MICROSTRUCTURE REFINEMENT AND MECHANICAL PROPERTY IMPROVEMENT OF AZ31 MAGNESIUM ALLOY RESISTANCE SPOT WELDS DUE TO INOCULANTS

by

Lin Xiao

A thesis
presented to the University of Waterloo
in fulfilment of the
thesis requirement for the degree of
Doctor of Philosophy
in
Mechanical Engineering

Waterloo, Ontario, Canada, 2012

I hereby declare that I am the sole author of this thesis. This is a true copy of the thesis, including any required final revisions, as accepted by my examiners. I understand that my thesis may be made electronically available to the public.

Abstract

Microstructure refinement was observed in the fusion zone of AZ31 magnesium (Mg) alloy resistance spot welds when an inoculant was added, either Ti, Al_8Mn_5, or Mn. The dependence of inoculant potency on the lattice disregistry between inoculants and matrix, and on the liquid cooling rate was studied. Microstructural characterization was performed via optical microscopy, scanning electron microscopy (SEM), and transmission electron microscopy (TEM). Thin foils containing the interface of the inoculant particles and Mg matrix were prepared using a focused ion beam (FIB) technique.

Columnar dendritic structures in the vicinity of the fusion boundary and equiaxed dendritic structures in the central area were observed in the fusion zone of welds in the SA and SB AZ31Mg alloys from different suppliers. However, the columnar dendritic zone (CDZ) was well restricted, and the width of the CDZ and the diameters of equiaxed dendrites were much smaller in the SA alloy than those in the SB alloy due to the earlier columnar-equiaxed-transition (CET) in the SA alloy. The refined microstructure in the fusion zone of the SA alloy welds is attributed to the pre-existence of the larger Al_8Mn_5 particles of 4-10μm in length in the SA alloy which act as an inoculant for α-Mg heterogeneous nucleation. Fatigue life and dislocation substructure were compared between the SA and SB welds. The SA welds with the refined microstructure displayed an enhanced fatigue resistance compared to the SB welds, when the interfacial failure took place across the fusion zone. The increased number and dispersion of slip systems in the fine-grained SA welds contributed to the improvement of fatigue life.

The well-developed columnar dendritic grains were successfully restricted and the coarse equiaxed dendritic grains were efficiently refined by intentionally adding Ti or Mn inoculant particles into the as-received SB alloy welds. The Ti and Mn particles of about 8μm diameter were observed to promote the nucleation of α-Mg grains during welding. TEM examinations showed the existence of local orientation relationships between the respective inoculants Ti, Mn, and Al_8Mn_5 with the Mg matrix. The further lattice matching was observed between the Al_8Mn_5 particles and Mg. The diameter of the added inoculant should be larger than 1.8 μm to make it a potent inoculant based on the thermodynamic calculation.

Microstructural examinations of samples with different inoculant additions and under different cooling rates showed that the inoculant potency was high for the Ti inoculant, medium for the Al_8Mn_5, but low for the Mn, when the cooling rate was low. This order in the decrease of grain refinement efficiency is inversely proportional with the order of crystallographic lattice disregistry between inoculants and matrix, which is calculated based on a crystallographic matching model. This implies that the lattice disregistry determines the potency of inoculants at the low cooling rates. In comparison, the lattice disregistry did not influence the heterogeneous nucleation, when the cooling rate was high. It could be inferred that an extremely high cooling rate produces a large supercooling, and provides a sufficient driving force for heterogeneous nucleation.

Keywords: Magnesium alloy; Resistance spot welding; Inoculant; Supercooling; Interface; Grain refinement; Crystallography; Heterogeneous nucleation.

Acknowledgements

I would like to sincerely thank my supervisors, Dr. Norman Zhou and Dr. Shahrzad Esmaeili. I appreciate the freedom they have given me to pursue my academic interests, as well as the guidance and insight that they provided when needed. I am very grateful for the opportunity to have worked with them during the period of this study.

I would like to acknowledge Dr. Scott Lawson for his ever punctual feedback and wise comments. I would also like to express my sincere appreciation to my friends who have supported me throughout the years. I have learned so much from you. Special thanks to: Dr. Lei Liu, Prof. S. Q. Zhou, Mr. Ali Nasiri, Mr. Alex Berlin, Dr. Xiaogang Li, and Dr. Yuquan Ding. You have made this an enjoyable journey.

This work is financially supported by the Natural Sciences and Engineering Research Council (NSERC) of Canada in the Framework of Strategic Magnesium Network Program (MagNET) and AUTO21 Network of Centres of Excellence of Canada. I would like to thank NSERC for the Postgraduate Scholarship and the University of Waterloo President's Graduate Scholarship.

I would like to thank Dr. Julia Huang and Mr. Fred Pearson from Canadian Center for Electron Microscopy, McMaster University, for help with preparing TEM films with FIB and TEM observation. We would also like to thank Mr. S.B. Behravesh for help with part of the fatigue testing.

For my family, who was there for me every step of the way.

TABLE OF CONTENTS

LIST OF TABLES

LIST OF FIGURES

1. Introduction

1.1. The Application of Magnesium Alloys in the Automobile Industry

Magnesium (Mg) alloys are attractive for lightweight structural applications in the transportation industry because of their low density, high specific strength and good stiffness. Significant weight savings can be made by substituting Mg alloys in place of steel or aluminum structural components of automobiles [1,2]. Therefore, Mg alloys are considered as advanced materials for coping with energy-conservation, carbon dioxide emission restriction, and environmental pollution regulations since higher fuel efficiency can be achieved through weight reduction of transportation vehicles [3,4].

The relatively rapid growth in consumption of Mg alloys in the automobile industry has been mainly attributed to the development of Mg–Al–Zn ternary system (*i.e.* AZ series alloys) introduced in the 1980s [5-7]. Major commercial grades of AZ alloys are AZ31, AZ61, and AZ91, which are produced either as cast products (*e.g.* die, sand, mold castings, and recently twin-roll strip casting) or wrought products (*e.g.* extrusions, forgings, sheets and plates). In general, as aluminum concentration increases, yield strength, ultimate tensile strength, corrosion resistance, and oxidation resistance of the alloys increase, whereas castability and weldability rapidly decrease [5-9]. Compared to Al, Zn is more effective in increasing strength and reducing ductility as a substitutional solid solution element. In addition to Al and Zn, other alloying elements, such as Ca, Sc, Y, and Zr, have been investigated for their potential impact on mechanical properties of Mg alloys [8]. Of the few AZ commercial Mg alloys, AZ91 is the most commonly used AZ alloy in the automotive industry; however, the AZ31 alloy represents a good compromise between mechanical strength, ductility, and cost [9].

Advantages of Mg alloys include high specific mechanical properties, high dimensional stability, high thermal conductivity, superior damping characteristics, good machinability, good electromagnetic shielding characteristics, and recyclability [5,10-12]. However, it has become clear that current wrought Mg alloys such as AZ31 are not best optimized to compete effectively with highly developed wrought aluminium alloys and current generation steels [6]. Processing of these Mg alloys, such as by casting, welding, and forming still faces many challenges so as to utilize their full potential.

1.2. Resistance Spot Welding of Magnesium Alloys

Welding is one of the manufacturing routes that can be used to optimize product design and minimize production costs. There has been a great amount of research activity on welding of AZ31 Mg alloys in recent years [13-22]. Various welding processes, including tungsten inert gas (TIG) welding [13,14], laser welding [13], electron-beam welding [16-18], resistance spot welding [19,20], and friction stir welding [21,22], have been employed in those investigations.

As one of the predominant joining techniques in sheet metal assembly, resistance spot welding (RSW) is a primary method for joining automotive structural components due to its advantages in terms of welding efficiency and automation [19,20]. Resistance spot welding involves the metallurgical bonding of two or more metallic parts by clamping them together between electrodes then applying current to generate local resistive heating causing melting followed by solidification of the metal in the proximity of the joint, as shown in Fig. 1-1. The generated heat can be expressed as:

$$Q=I^2Rt \tag{1-1}$$

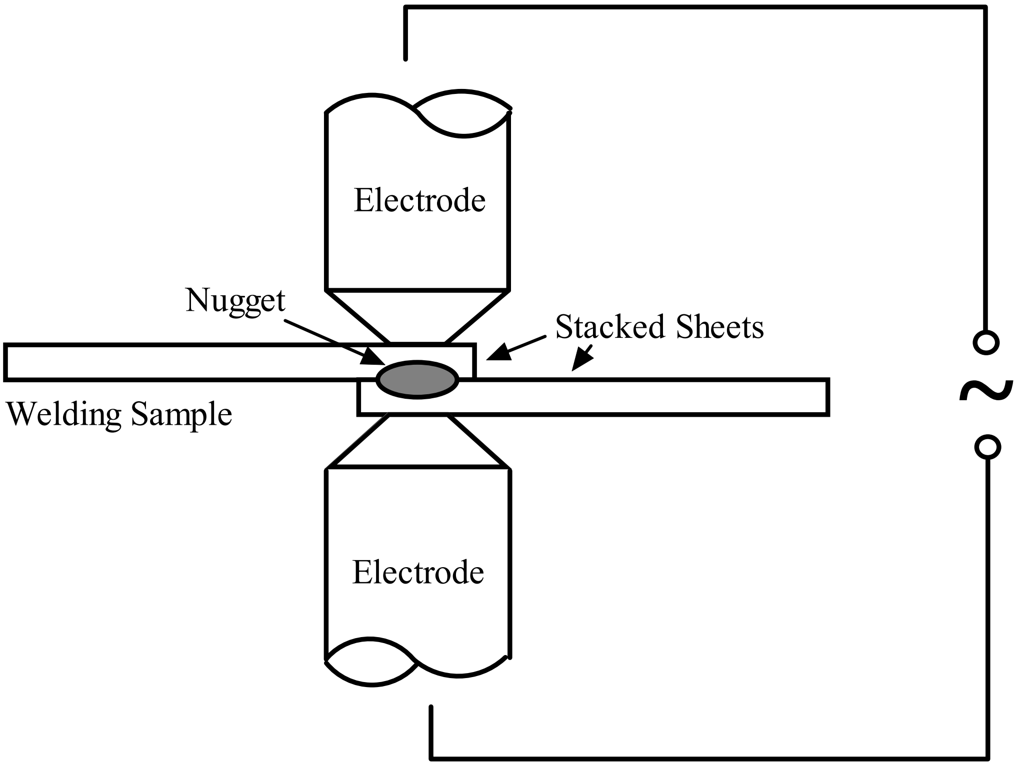

Fig. 1-1. Schematic illustration of resistance spot welding

where Q is heat, I is welding current, R is electrical resistance of the circuit, t is the time the current is allowed to flow in the circuit [23]. The electrical resistance, R, is comprised of the bulk resistance of materials and the interfacial resistance of contact surfaces. Furthermore, the interfacial resistance includes resistance at the interfaces of electrodes and workpieces, and the faying interfacial resistance between the two workpieces [24].

In strength or weldability tests on spot welded joints, lap shear samples or cross tension samples are often used [25]. A schematic representation of two primary failure modes, *i.e.,* interfacial and through thickness failure modes, are depicted by two dashed lines in Fig. 1-2. In a large weld, through thickness failure may occur, in which the weld nugget is completely pulled out from one of the metal sheets, leaving a circular hole in the sheet, as indicated by a straight dashed line on the left side of Fig. 1-2. In comparison, an interfacial fracture propagates through the weld nugget and is often found in smaller welds, as indicated by a curved dashed line on the upper half side of Fig. 1-2. Interfacial failure is associated with a lower load carrying capacity and considerably less energy absorption capability; therefore, industrial practice is to avoid this mode of failure [26].

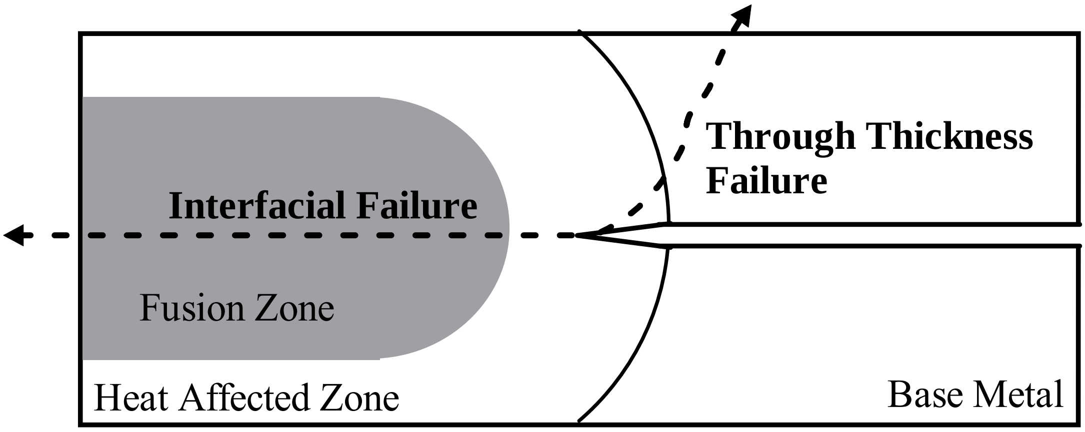

Fig. 1-2. Schematic representation of interfacial and through thickness failure modes. Interfacial failure: straight dashed line on the left side; through thickness failure: curved dash line on the upper half side.

The melting nugget area, as indicated by the shaded areas in Figs. 1-1 and 1-2, is usually defined as the fusion zone. The area immediately outside of the fusion zone is defined as the heat-affected zone (HAZ), as shown in Fig. 1-2. During welding, solidification of a liquid in the fusion zone is similar to that in a metal casting. Although many useful insights and data have been obtained on welding and microstructure of Mg alloys [13-22,27-29], there are still many issues to be addressed before Mg alloy welding can be fully used in real industrial applications. Further research and development efforts related to welding of AZ31 Mg alloys are required. This thesis focuses on studying microstructure evolution in the fusion zone of Mg alloy welds; the microstructure in the HAZ is outside the scope of this work.

1.3. Microstructure and Mechanical Property Improvement of Magnesium Alloy Welds

Columnar and equiaxed dendritic grains are two primary microstructures formed in resistance spot welds [19,20,29]. Growth of columnar grains initiating from the fusion boundary often terminates with the appearance of equiaxed grains or, a band of equiaxed grains as the columnar grains propagate towards the centre of the fusion zone. This process is known as the columnar-to-equiaxed transition (CET) [29,30-37]. Solidification of a resistance spot weld often results in a columnar grain structure in the fusion zone of welds. The alignment of grain boundaries often produces a relatively weak plane along the centreline of the solidified nugget which may be susceptible to brittle fracture or solidification cracking [29]. The presence of equiaxed grains in the fusion zone may enhance the mechanical properties and decrease the susceptibility to cracking. Therefore, it would be desirable to replace columnar grains with fine equiaxed ones to improve the weldments' mechanical properties.

The behaviour of Mg alloys during RSW is different from that of steel or Al alloys due to their lower melting point, greater fluidity, higher chemical activity, higher thermal and electrical conductivity, and larger coefficient of linear expansion [16-20,27,28]. The strength of Mg alloy weldments is generally much lower than that of the corresponding base material; the weldability of Mg alloys joined by conventional fusion welding is also usually inferior to that of steel, because the well-developed columnar grains in the vicinity of fusion boundary and coarse equiaxed dendritic grains formed in the centre of the fusion zone can seriously compromise the mechanical properties of joints in Mg alloys [1-6,27-29,38]. Therefore, there has been considerable experimental research on refining microstructure in the fusion zone of Mg alloy welds, and a number of approaches to refine grain size have been developed [13,19-

22,27,39]. Among them, inoculation using grain refining particles offers the greatest promise for practical application [40-46].

Inoculant particles can either promote or suppress grain refinement depending on their type, size, and fraction [29-31,33,35]. Although grain refinement of Mg alloy castings using inoculants has been investigated (previous work on this subject is reviewed in Chapter 2), less attention has been paid to the microstructural refinement of Mg alloy welds. Furthermore, most studies have concentrated on trial and error techniques rather than fundamental understanding of the solidification mechanisms of welds. On the other hand, there has been considerable experimental research on the columnar-to-equiaxed transition (CET) in welds and the CET has been successfully promoted in welds by adjusting welding processes or introducing foreign inoculants [30-37], but the detailed relationships between the thermal conditions in the fusion zones of welds, the type and size of inoculant particles, and the interfacial crystallographic characteristics of the added inoculants and matrix are obscure. Therefore, a systematic study is significant to refine microstructures and thus improve mechanical properties of AZ31 Mg alloy welds by introducing inoculant particles in the fusion zone.

1.4. Objectives and Scope

The objectives of this research are defined to provide in-depth understanding of the heterogeneous nucleation mechanism on inoculant particles by determining the dependence of inoculant potency on the crystallographic lattice disregistry between the inoculant particles and matrix, and the cooling rate of liquid phase in the fusion zone of the AZ 31 Mg alloy welds. This research provides a considerable contribution to the present knowledge on microstructural refinement mechanisms in the fusion zone of welds from perspectives of crystallography and thermodynamics, and provides a fundamental understanding for selecting type and size of inoculant particles.

The research consists of three major components:

1. Based on microstructural characterization of resistance spot welds (RSWs), the dependence of welding microstructure morphology and size on second-phase particles is studied in two AZ31 Mg alloys, AZ31-SA (from Supplier A) and AZ31-SB (from Supplier B) with the similar chemical composition under the same welding condition. We focus on studying the relationship between the microstructural refinement and columnar-to-equiaxed transition (CET) with the size of second-phase particles in the fusion zones of welds. Fatigue behaviour is compared between resistance spot welds made in these two AZ31 Mg alloys so as to evaluate the effect of grain refinement on mechanical properties of welds, and explore the dependence of cyclic plastic deformation mechanism on the solidification microstructure and its effect on the fatigue life of welds.

2. Mg alloy welds are inoculated with Ti, Mn, and Al_8Mn_5 particles which act as nucleants of α-Mg grains so as to refine microstructure and enhance weldment mechanical properties. The interfacial orientation relationships between three different inoculant particles and the Mg matrix are systematically analyzed by transmission electron microscopy (TEM). The grain refinement mechanism in AZ 31 Mg alloy resistance spot welds is analyzed from perspective of crystallography.

3. The relationship between the inoculant potency, lattice disregistry, and cooling rate is investigated. On the basis of assessment of the inoculant efficiency on refining microstructure of an AZ31 Mg alloy according to the crystallographic matching model, the work concentrates

on analyzing the interfacial characterization, and crystallographic orientation relationship with high resolution transmission electron microscopy (HRTEM), aiming to develop a criterion for choice of potent inoculants. Furthermore, a series of welding experiments is designed to ascertain the effect of cooling rate on microstructural refinement, and verify the relationship between the predicted potency of inoculants, supercooling level, interfacial energy in AZ31 alloy during welding.

2. Literature Review

2.1. Magnesium Alloy Systems

Magnesium alloys can be generally classified into two broad categories depending on whether they are alloyed with Al: Al-free and Al-bearing alloys. Al-free alloys mainly refer to those containing zirconium (Zr) due to the exceptional grain-refining ability of Zr when added to alloys that do not contain Al, such as ZE41, ZK60, WE43, AM-SC1, and ML10. In comparison, Al-bearing Mg alloys are the most common and economic commercial Mg alloys, which include AM50, AM60, AZ31, AZ61, and AZ91. Zr is not used in Al-containing alloys in spite of its exceptional grain-refining ability, since Al and Zr can form stable intermetallic phases [47-49].

AZ (Mg–Al–Zn) and AM (Mg–Al-Mn) series alloys with the Mn addition of 0.05 to 0.6 wt% are common commercial Mg alloys for practical use in automobile industry nowadays [47,48]. AZ31 Mg alloy has an excellent combination of good mechanical strength, ductility, and low cost. The phase components and microstructures of AZ31 Mg alloys have been studied both theoretically and experimentally [50-62]. To reduce the iron (Fe) content below a tolerable level less than 50 ppm, a small amount of manganese (Mn) is generally added to the molten AZ31 Mg alloy for removing Fe, since Fe existing as an impurity in the Mg alloys drastically degrades their corrosion resistance [47,48].

The equilibrium Mg–Al–Zn–Mn phase diagram is not known in great detail, but some features near the Mg corner have already been determined, as shown in Fig. 2-1, in which the contents of Al and Zn are fixed to 3.1 and 1.3 wt%, respectively [47,48,50]. It has been demonstrated that equilibrium phases at room temperature in Mg alloys with 2 to 9 pct Al and less than 1%

Mn are α–Mg solid solution, $Mg_{17}Al_{12}$, and Al_8Mn_5 [47,48]. The solid-solubility limit of Mn in a Mg–3 wt%Al alloy is only 0.1 to 0.2 wt% at 400°C. The amount and the size of the Al–Mn compounds increases with increasing Mn content. The Al-Mn binary phase diagram is shown in Fig. 2-2 [51]. The possible Al–Mn compounds formed during solidification can be considered to be Al_8Mn_5 and $Al_{11}Mn_4$ depending on the Mn concentration and cooling rate according to the Mg–rich part of the Mg–Al–Zn–Mn phase diagram (Fig. 2-1) [47,48] and Al-Mn phase diagram (Fig. 2-2). The melting points of Al_8Mn_5 and $Al_{11}Mn_4$ are 1160 and 989°C, respectively. The size and distribution of Al–Mn compounds are not affected by the homogenization treatment due of their high melting points leading to the high thermal stability.

Laser *et al.* [50] calculated the equilibrium phase diagram of Mg–3.1Al–1Zn alloy added with 0.28-0.8wt% of Mn using the database of Ohno and Schmid-Fetzer based on the Scheil model. The results showed that the AZ31 predominantly consists of α-Mg and $Al_{11}Mn_4$ phases in the equilibrium condition. However, it is primarily composed of β-Mn(Al), γ-$Mg_{17}Al_{12}$, and Al_8Mn_5 phases during rapid solidification according to non-equilibrium kinetic models [43]. Laser *et al.* [50,52] suggested that both β-Mn(Al) and Al_8Mn_5 may act as potential heterogeneous nucleants for Mg grains and thus as potential grain refiners in the Mg–Al system. Mirkovic *et al.* [53,54] extended the well-known Scheil method to ″Scheil-total″ thermodynamic calculation of segregation so as to reflect the solute profiles of the components dissolved not only in the matrix phase but also in all precipitating phases. They theoretically predicted that the components of precipitates in AZ31 Mg alloy consisted of Al_8Mn_5 and γ-$Mg_{17}Al_{12}$ double Phases. Furthermore, they experimentally identified the appearance of these double precipitate phases in Mg matrix via electron probe microanalysis (EPMA) [53,54].

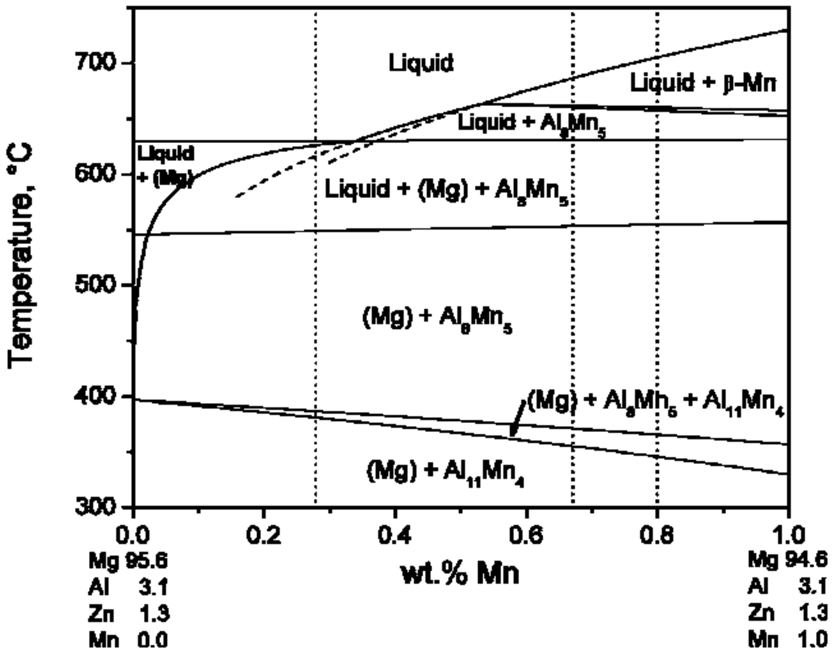

Fig. 2-1. Phase diagram of Mg-Al-Zn-Mn system (Taken from Laser *et al.*) [50]

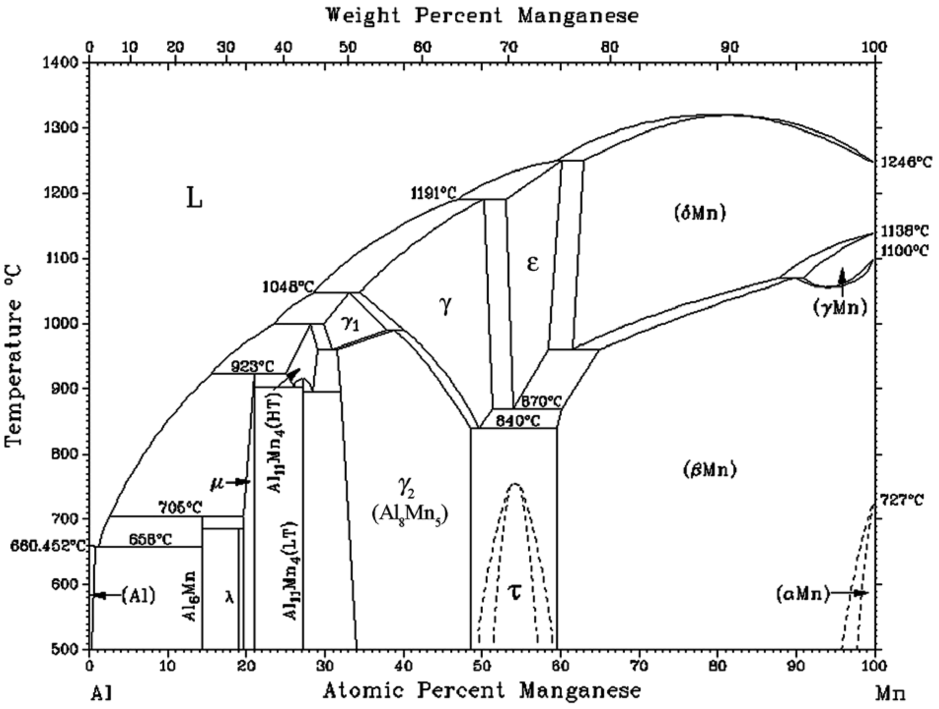

Fig. 2-2. Al-Mn binary phase diagram (Taken from Massalski) [51]

$Mg_{17}Al_{12}$ is an eutectic constituent and forms a complex cubic crystal structure, which is isostructural with α-Mn, with a lattice parameter a = 10.56 nm [48]. Al-Mn intermetallic particles in the AZ31 Mg alloy have been observed by several researchers [48,51,52,55-59]. Laser *et al.* [50,52] suggested that some Al-Mn particles in the form of Al_8Mn_5 could be present on the dendritic arms and in the matrix in as-cast AZ31 alloy. By means of extraction technology, Liu *et al.* [58] observed that Mn existed in the as-cast AZ31 Mg alloys in the form of Al_8Mn_5 phases of 15-100μm length or as dissociated Mn particles. It has been well-accepted that the equilibrium Al_8Mn_5 intermetallic compound has a rhombohedral structure with a = 0.906 nm and α = 89.3 deg, which is described by a = 1.265 nm and c = 1.586 nm in trigonal coordinates [48,60]. This phase has a significant homogeneity range of ~31 to 50 at. % Mn [51].

2.2. Microstructure Refinement and the Columnar-to-Equiaxed Transition (CET) in the Fusion Zone of Welds

2.2.1. Microstructure Refinement in the Fusion Zone of Welds

The differences of thermal, structural, electric properties among the metallic materials inevitably lead to differences in solidification microstructure of resistance spot welds. The nugget microstructures of most metals and alloys such as steel, Mo, Ni, Ti, and Cu alloys demonstrate entirely columnar dendritic structures [30-32,63]. Others including Al and Mg alloys consist of columnar grains around the periphery and equiaxed grains in the centre [19,29,30-32,39,63]. Fig. 2-3 shows the typical microstructures of resistance spot welds in different materials [19,63]. During RSW, weld pool solidification always starts from the parent metal partially molten zone with a minimum degree of supercooling since the solidified phase

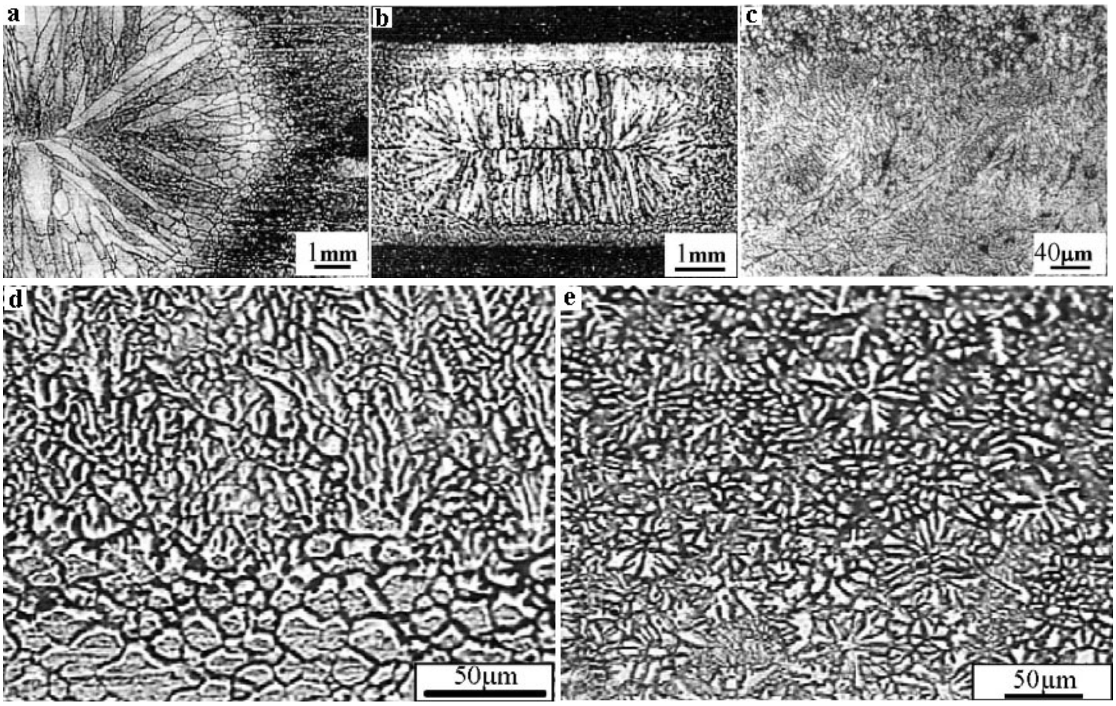

Fig. 2-3. Typical microstructures of resistance spot welds: (*a*) Cr17 stainless steel [63], (*b*) TA7 Ti alloy (Taken from Wang *et al.*) [63], (*c)* LY12CZ Al alloy (Taken from Wang *et al.*) [63], (*d*) and (*e*) AZ31 Mg alloy (Taken from Sun *et al.*) [19].

has the same crystalline structure as the base metal (BM). This leads to the well-known epitaxial growth without requiring any nucleation event. Columnar grain growth proceeds in the direction of steepest thermal gradient in the liquid, G_L, at a local growth rate, *R*. Coarse columnar grains are often the predominant macrostructure [29,30-32,39]. In as solidified structures, growth of columnar grains often terminates with the appearance of an equiaxed zone or, possibly, a band of equiaxed grains, resulting in the CET.

The microstructure of welds primarily depends on the welding conditions and the size and distribution of any inoculant particles in the fusion zone. Owing to the good heat conductivity of Mg alloys, the liquid temperature at the edge of a RSW nugget drops so quickly that the liquid is in a highly supercooled state during solidification, which promotes epitaxial growth of cellular-dendritic crystals. As solidification progresses, the solute concentrations of Al and Zn atoms in front of the solid/liquid interface increase and the temperature gradient tends to decrease in the liquid near the centre of the nugget due to the relatively poor heat extraction and the released latent heat. Under such conditions, constitutional supercooling is sufficient to result in the formation of equiaxed dendritic crystals by radial dendritic growth of the nuclei [30-32].

The CET may be promoted by providing both (i) thermal conditions which favour the nucleation and growth of embryos into equiaxed grains [33-37]. The equiaxed grains could be formed in alloys even in the absence of deliberately added nucleants, if the thermal supercooling condition can satisfy the nucleation condition; and (ii) inoculants of equiaxed grain nucleating substances [64]. In welds, the nuclei for equiaxed grains have two general sources: (1) nuclei composed of the base metal, created by dendrite fragmentation, grain detachment, or surface nucleation; these grain fragments do not have supercooling, $\Delta T_N \approx 0$, and will nucleate equiaxed grains if they survive in the melt and the correct thermal conditions are present, and (2) heterogeneous nuclei composed of second-phase particles or added inoculant particles in the melt which will nucleate equiaxed grains if the correct thermal conditions are available [64].

Various grain refinement techniques have been applied in controlling the weld bead microstructures of Mg alloys [2,41,42,49,53,54,61,65]. They mainly include: (1) superheating; (2) carbon inoculation [61]; (3) the Elfinal Process [2]; (4) native grain refinement by control of impurity level; (5) grain refinement by means of other additives, such as Zr, Sr, RE, Th, Si, Ca, B, AlN, MgO, TiB_2, and TiC [41,42,49]; (6) alloying to promote constitutional supercooling/dendrite fragmentation; (7) electromagnetic stirring; (8) current pulsing; (9) torch vibration; (10) arc oscillation [13,19,30,43]. Among them, inoculation using grain refining particles offers the greatest promise for practical application [40-46]. However, none of the approaches has been satisfactory in the commercial application so far, and a suitable grain refiner for Mg-Al alloys is still elusive.

2.2.2. Mechanisms of the Columnar-to-Equiaxed Transition

Various mechanisms have been proposed to try to explain the local interaction of columnar grain growth and equiaxed grain formation that gives rise to the CET. These consider, to some extent, the solute and temperature fields, fluid flow and the growth of equiaxed grain nuclei. There have been a few reviews that consider the detailed relationship between solidification parameters and weld structures and the CET in castings and welds [30,31,64,66-68]. There is a consensus that the CET occurs when the moving front of columnar grains is blocked by equiaxed grains growing in the supercooled liquid ahead of this front. Regardless of the origin of the dendrites, it is clear that the condition of the bulk liquid determines whether a columnar grain or an equiaxed grain prevails [64,66-68].

Tiller *et al.* [69] have introduced the initial quantitative derivation of the conditions necessary for the breakdown of a planar interface and the formation of the CET as follows:

$$G / R < -mC_0(1-k)/kD \qquad (2\text{-}1)$$

where G is the temperature gradient in the liquid, R the interface velocity, m the liquidus slope, C_0 the initial alloy composition, k the equilibrium distribution coefficient, and D the solute diffusion coefficient in the liquid.

The relationship between the growth rate and the temperature gradient in forming the CET can be described in the well-known CET diagram of Hunt [70]. Quested and Greer [71] append the

Hunt diagram with contours of equal grain size in the equiaxed region of the diagram, as shown in Fig. 2-4. They predicted the variation of grain size with refiner addition level, solute content in the melt and cooling rate. The grain size is predicted to be independent of solidification velocity or thermal gradient at a given cooling rate. Gaumann *et al.* [72] developed a CET diagram based on a more sophisticated dendrite growth law. Martorano *et al.* [73] have considered the effects of solutal interactions between dendrites and given a modified CET diagram with solutal blocking effects.

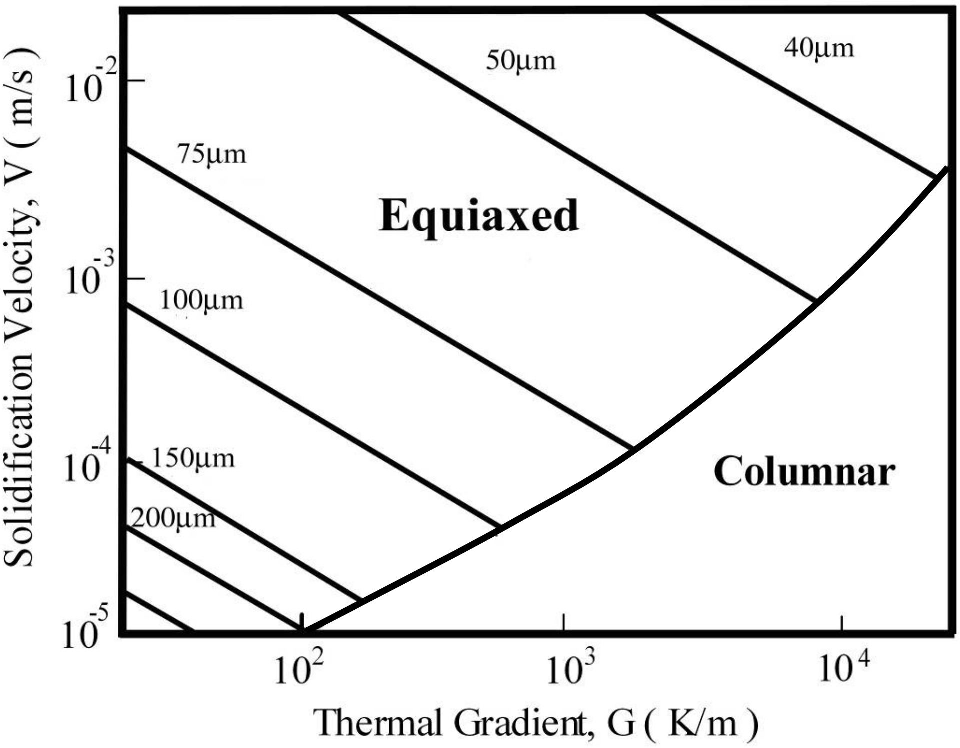

Fig. 2-4. The modified CET diagram of Hunt by Quested and Greer [71].

Numerous mechanisms for the CET have been proposed based on experimental evidence. Hallum and Baeslack [74] inoculated titanium alloy gas tungsten arc welds with Ti-6Al-4V powder. The inoculant additions were observed to reduce the melt temperature and lower the thermal gradients near the tail of the weld pool, thus favouring equiaxed grain growth by heterogeneous nucleation on partially melted inoculant particles. Kato *et al.* [75] showed that increasing the alloy composition favours a CET, since alloying agents, *i.e.* inoculants, may provide nucleants for equiaxed grains and potentially increase the growth supercooling.

Reinhart *et al.* [76], Mangelick-Noel *et al.* [77] and Nguyen *at al.* [78] used a synchrotron X-radiography approach to make in-situ and real-time observations of the solidifying interface, in particular at the CET in the refined and non-refined Al–3.5wt.% Ni alloys in a Bridgman furnace, as shown in Fig. 2-5 (a) to (d). Solidification was started with a low pulling velocity of 1.5 μm/s to produce a columnar dendritic structure (Fig. 2-5 (a)). In order to provoke the CET, a sharp jump of the pulling rate V_P to a higher value (6, 10 and 15 μm/s) was applied at t_0. In all cases, a short time after the velocity jump, a band of small equiaxed grains appeared in the supercooled liquid adjacent to the columnar dendritic front (Fig. 2-5(b)). When enough grains had nucleated and could grow, they blocked the columnar growth leading to the CET (Fig. 2-5(c) and (d)).

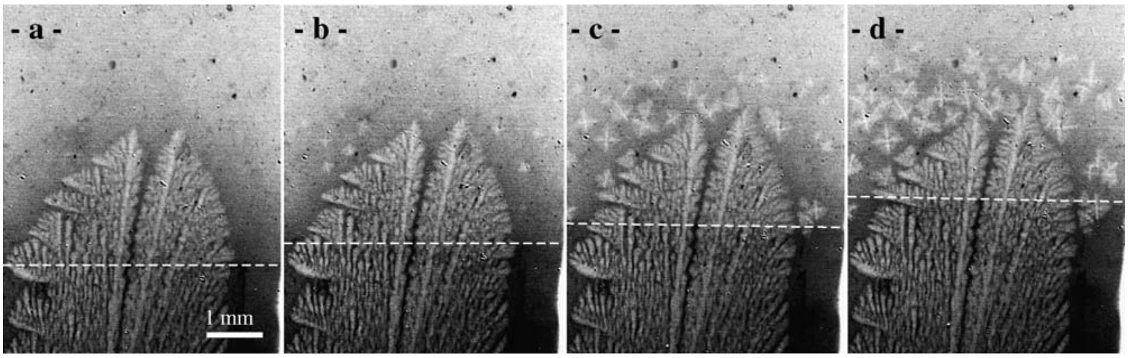

Fig. 2-5. Sequence of four images of refined Al–3.5 wt.%Ni solidification, recorded during the CET induced by a sharp pulling rate jump from 1.5 to 15 μm/s by synchrotron X-ray radiography, G= 20 K/cm: (*a*) $t = t_0$ +42 s, (*b*) +63 s, (*c*) + 87 s, and (*d*) + 111 s. The solid mainly constituted of aluminum appears in grey while the Ni enriched liquid is dark. The dashed line underlines the eutectic front position (Taken from Reinhart *et al.*) [76, 78].

Sturz *et al.* [79] studied the directional solidification behaviour of Al–7 wt.%Si alloy both with and without the deliberate addition of inoculant particles, using the same in-situ observation technique. The temperature gradient decreased and the solidification rate increased simultaneously to initiate the CET in a transient experiment. A linear decrease in columnar grain length with increasing cooling rate was found for non-refined alloys. The critical experimental values of G and V at the CET were compared with the models of Hunt [70] and Martorano *et al.* [73] calculated for Al–7 wt.%Si, for three different values of the critical supercooling: 0, 3, and 5 K. The critical experimental values were found to be in good agreement with the model of Martorano *et al.* [73] for a critical supercooling of about 5 K.

Heterogeneous nucleation always plays an essential role in solutions containing second-phase particles. According to Hunt's model [70], the presence of heterogeneous nucleants ahead of the solidification front is not sufficient for the CET, it also requires necessary low thermal gradients and high interface growth rates. Heterogeneous nucleation can be promoted by introducing foreign inoculants or adding grain refiner during the casting of the base metal [64,66,80]. Different mechanisms of equiaxed grain formation may operate in the different studies, even in the absence of deliberately added inoculant particles. Under steady controlled freezing conditions and in the absence of thermosolutal convection, heterogeneous nucleation in the bulk liquid ahead of the advancing front may be a plausible mechanism [70-73]. In the presence of thermosolutal convection, dendrite remelting/fragmentation may be the mechanism as evidenced in the study by Pollock and Murphy [80]. Under nonsteady freezing conditions, loss of heat from the upper liquid surface may result in the formation of a surface dendritic layer. Fragmentation of this layer could lead to showering of dendrite fragments which grow as equiaxed crystals [64]. Quested and Greer [71] suggested that equiaxed microstructures are favoured by high interface growth velocities, low temperature gradients, high solute levels, and a large number of equiaxed nucleation events.

The other mechanisms of equiaxed grain formation involve surface nucleation [35,81], dendrite fragmentation [30,35,43], grain detachment [30,34], showering of dendrite particles [82], separation of equiaxed crystals from mould wall [83], and heterogeneous nucleation [40,44-46,73,83,84]. Surface nucleation often occurs when supercooling at the weld pool surface causes solid nuclei to form which then sink into the weld pool due to their higher density [35,81]. Dendrite fragmentation is produced by weld pool convection in the presence of branched dendrites. Sufficient convection dislocates dendrite fragments from the mushy zone and sweeps them into the pool where they grow into equiaxed grains when the thermal gradients permit [30,35,43]. Grain detachment is a mechanism by which small grains in the partially molten region of the heat affected zone detach and become entrained in the weld pool [34,40]. The showering mechanism was proposed by Ruddle [85] who found that a combination of high welding speeds and low power densities provide the thermal conditions required for the nucleation and growth of equiaxed grains in the weld pool in Al-Cu-Mg-Mn aluminium alloy, providing heterogeneous nucleation sites are available. The most likely origin of the nucleants is from a combination of dendrite fragments and TiB_2 particles that survive in the weld pool under supercooled liquid ahead of the moving solid-liquid interface [85]. In brief, a variety of mechanisms of heterogeneous nucleation and the CET could be activated depending on the materials parameters and the solidification conditions.

2.2.3. Modeling of the Columnar-to-Equiaxed Transition

The significant renewed interest in the CET since the 1980s has resulted from the emergence of new modelling approaches to investigate the CET which, as a consequence, have prompted further experimental studies [64,86]. The CET models can be classified as stochastic or deterministic. Stochastic models aim to follow the nucleation and growth of each individual grain [87-94]. The shape evolution of each grain is calculated as a function of the local thermal conditions. The CET may then be determined based on whether the average final grain shape in a portion of a casting appears more columnar or equiaxed. The main limitation of stochastic models is related to the large amount of computer resources needed to resolve the large number of grains potentially present in a casting. Deterministic models of the CET, on the other hand, do not attempt to resolve the nucleation and growth of each grain in a casting. Instead, they rely on averaged quantities and equations that are solved on a macroscopic scale [91,95-97]. By tracking the movement of the columnar front and calculating the growth of equiaxed grains in the supercooled liquid in front of it, the CET is predicted. Hunt [70] proposed the first deterministic model to predict conditions for the CET. The final equation derived by Hunt [70] states that the CET occurs or will have occurred when the following condition holds:

$$G < 0.617 n^{1/3} \Delta T_t \left(1 - \left(\frac{\Delta T_N}{\Delta T_t} \right)^3 \right) \tag{2-2}$$

where ΔT_t is the supercooling at the columnar dendrite tips, is calculated from an empirical relation as a function of the isotherm velocity. ΔT_N is a supercooling of a certain number of equiaxed grains per unit volume (n), assumed to nucleate instantaneously ahead of the columnar front.

The simulation of CET has had limited success owing to the complex interplay of macroscopic phenomena, such as heat transfer and fluid flow, and microscopic phenomena, such as nucleation and dendritic growth. All previous CET models neglect or oversimplify the treatment of melt convection and movement of free equiaxed grains. Usually, equiaxed grains are assumed to nucleate and grow in the constitutionally supercooled liquid ahead of the advancing columnar front, as originally proposed by Winegard and Chalmers [98]. The CET occurs when the advance of the columnar front is blocked by the equiaxed grains. Therefore, systematic research on the mechanisms of heterogeneous nucleation and the CET is essential to provide a physical foundation for simulation.

2.2.4. Grain Refinement of AZ31 Mg Alloy Welds due to Inoculants

The promotion of heterogeneous nucleation by the intentional addition of inoculant particles during casting has been studied in a number of pure metals and eutectic mixtures [33,70,99,100]. Considerable theoretical modelling and experimental examinations have been made to understand heterogeneous nucleation on inoculants of different potency and geometries and the characteristics of dendritic interface growth since the 1980s [33,70,99,100-107]. Unfortunately, no satisfactory model or equation is able to incorporate the interfacial energy and the solidification condition. Therefore, an understanding of the dependence of the inoculant potency on the interfacial properties of the inoculants and the cooling rate is of considerable significance.

Heterogeneous nucleation into a specific crystallographic phase is characterized by an activation energy barrier (ΔG^*) to form a nucleus of critical size, r^*, in the supercooled melt [29,30,31,108,109]. According to the classical nucleation theory [100,108,109-112], ΔG^* is given by:

$$\Delta G* = \frac{16\pi\sigma_{sl}^3}{3\Delta G_V^2} \cdot f(\theta) \qquad (2\text{-}3)$$

where σ_{sl} is the interfacial energy between the crystal nucleus and the supercooled melt, ΔG_V is the Gibb's free energy change per unit volume for liquid to solid phase transformation, $f(\theta)$ is inoculant potency factor in the case of heterogeneous nucleation. ΔG_V is negative below the melting temperature and, consequently, drives the phase transformation, σ_{sl} is always positive, which leads to the activation energy barrier for the formation of a critical nucleus, *i.e.* ΔG^*.

Nucleation of equiaxed dendrites in the liquid region ahead of a liquid-solid interface is assumed to take place instantaneously at a thermodynamic total supercooling ΔT, [30]. The total supercooling equation can be expressed as [102,113]:

$$\Delta T = \Delta T_t + \Delta T_c + \Delta T_r + \Delta T_k \tag{2-4}$$

The components, in order, are the thermal supercooling, ΔT_t, the constitutional (solutal) supercooling, ΔT_c, the the curvature supercooling, ΔT_r, and the kinetic supercooling ΔT_k. Furthermore, this equation can be expressed as [102,113]:

$$\Delta T = \frac{L}{C_p} Iv(P_t) + m_L C_0 \{1 - \frac{m_L^{'} / m_L}{1-(1-k_0) Iv(P_c)}\} + \frac{2\Gamma}{r} + \frac{V}{\mu} \tag{2-5}$$

where, L is the latent heat of fusion, C_p is the specific heat, P_t is the thermal Peclet number, $P_t = V \cdot R$. $Iv(P_t)$ is the thermal Ivantsov function, $Iv(P_t) = P\exp(P)E_1(P)$, m_L is the liquidus slope, k_0 is the partition coefficient, C_o is the composition, the solute Peclet number, $P_c = VR/2D$, D is the solute diffusion coefficient in liquid, and Γ is the Gibbs–Thompson parameter, defined as the ratio of the specific liquid-solid interface energy to the melting entropy, V is the interface velocity, R is the tip radius of a dendrite.

It has been generally accepted that dramatically increasing the cooling rate (dT/dt) could increase the thermal supercooling degree (ΔT_t) of the liquid [86,114-126]. A semi-empirical equation that predicts a linear increase between $\ln\Delta T_t$ and $\ln(\mathrm{d}T/\mathrm{d}t)$ was established based on a great number of experimental data of crystallization [120-124]. Liu *et al.* [114] calculated and measured the cooling rate and the total supercooling in DD3 superalloy during rapid solidification. The results showed the total spercooling could reach 158 K, when the cooling rate was 2.8×10^5, and 53 K at 5×10^4 K sec^{-1}. The total supercooling was 0 when the cooling rate was $\leq 1.4\times10^4$ K sec^{-1}. Kim *et al.* [125,126] experimentally measured cooling rate and grain size in melt-spun Ni-A1 alloys and 316L stainless steel. The results indicate that the total nucleation supercooling, ΔT, is proportional to the cooling rate, $\mathrm{d}T/\mathrm{d}t$:

$$\Delta T \propto \mathrm{d}T/\mathrm{d}t \qquad (2\text{-}6)$$

Nucleating particles have been widely used to refine grains of Mg alloy castings [43, 42-60, 64, 65, 99, 100]. Earlier work by Tiner [127] showed that Mg–Al alloys containing 0.19% Mn or more (up to 0.98% Mn) demonstrated grain refinement. Recently, Byun *et al.* [128] studied the slurry formation process of AZ91 containing different Mn levels ranging from 0.23% to 0.45%. $Al_8(Mn,Fe)_5$ particles were observed in the resulting primary Mg crystals. They thus suggested that $Al_8(Mn,Fe)_5$ particles could act as nucleation sites for primary Mg grains in Mg–Al alloys. Laser *et al.* [50] reported grain refinement by Al_8Mn_5 particles in AZ31 alloys. Some researchers tend to believe that one or more Al–Mn or Al–Mn–Fe intermetallic compounds may form at high temperature and act as effective grain refiners during subsequent cooling of Mg-Al alloy [50,128,129]. Qiu *et al.* [46] compared the grain refining efficiency of various (Al, Mn)-containing phases including the equilibrium β-Mn, γ-AlMn, ε-AlMn phase, and meta-stable τ-AlMn phase in Mg–Al alloys, and suggested that a metastable τ-AlMn phase could serve as an effective heterogeneous nucleation site. However, the metastable τ-AlMn phase can only be generated from the high temperature ε-AlMn phase through a massive transformation. Overheating the melt is necessary to produce the high temperature ε-AlMn phase. Therefore, further convincing experimental evidence is needed to prove that the high temperature ε-AlMn phase can be retained in the Mg alloys at low solidification temperatures.

2.3. Critical Size of Heterogeneous Nucleation in Mg Alloy Welds

Heterogeneous nucleation would occur ahead of the columnar front once the supercooling suffices to induce heterogeneous nucleation, depending upon the inoculant sizes. If the size of second-phase particles in front of the interface is not big enough, then any growing equiaxed grains will be trapped by the progressing columnar grains and the grown macrostructure will retain a columnar dendritic morphology [64]. However, new grains will nucleate and grow if the second-phase particles are big enough to become nuclei in the areas near the fusion boundary [64].

Besides the well-known classical flat substrate model [130,131], various heterogeneous nucleation models have been proposed. Fletcher's spherical substrate model is a classic model to understand the heterogeneous nucleation of supercooled or supersaturated solutions by foreign particles [108,132], as shown in Fig. 2-6. The parent phase is denoted by subscript 1, the embryo by 2, and the nucleus by 3, V is the volume, and S is the surface area. The free energy of formation of an embryo of radius r on a nucleus of radius R can be expressed:

$$\Delta G=\Delta Gv V_2+\sigma_{12}S_{12}+(\sigma_{23}-\sigma_{13})S_{23} \tag{2-7}$$

where ΔGv is the free energy difference per unit volume of phase 2 between matter in state 1 and matter in state 2, and σ_{ij} is the surface free energy of the interface between phases i and j.

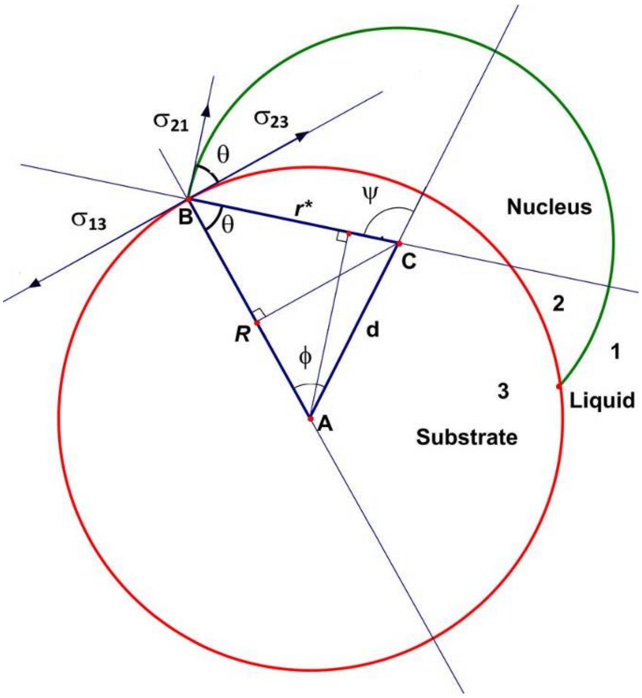

Fig. 2-6. A schematic illustration of a spherical-cap embryo formed on a convex spherical substrate surface with $\theta < 90°$ (Taken from Fletcher) [108].

Independently of the shape or even presence of the nucleus, the critical radius r^* must satisfy the usual nucleation equation

$$r^* = -2\sigma_{12}/\Delta G_v \tag{2-8}$$

The free energy of formation of a critical embryo is

$$\Delta G^* = \frac{8\pi\sigma_{12}^{\ 3}}{3(\Delta G_v)^2} f(m,x) \tag{2-9}$$

and

$$f(m,x) = 1 + \left(\frac{1-mx}{g}\right)^3 + x^3\left[2 - 3\left(\frac{x-m}{g}\right) + \left(\frac{x-m}{g}\right)^3\right] + 3mx^2\left(\frac{x-m}{g} - 1\right) \tag{2-10}$$

where

$$x = R/r^* \qquad (2\text{-}11)$$

and

$$g = (1 + x^2 - 2mx)^{\frac{1}{2}} \qquad (2\text{-}12)$$

When nucleant particles are present in a molten pool, thermal and constitutional supercooling driven heterogeneous nucleation is believed to play an important role in promoting the CET. According to the Fletcher's model [108], it has been well accepted that the size effect of a nucleant particle is related to the critical embryo radius, r^*, which is a function of the supercooling. It was recently demonstrated that the bigger the nucleant particle is, the more efficient it is, when the radius of the nucleant particle, R, is smaller than $5r^*$ [132]. However, the additional influence of the nucleant particle size on heterogeneous nucleation is limited, when $R > 5r^*$. [132]

According to the free-growth model for nucleation on potent inoculant particles, Greer [111,134] suggested that grain initiation is limited by the barrier for the free-growth of nucleated α-Al from the nucleant surface, rather than by nucleation itself in Al added with the commercial inoculant, Al-5Ti-1B. The supercooling necessary to initiate the free-growth is inversely proportional to the diameter of the particle surface, and the particle size distribution determines refiner performance. Any initial nucleus can readily grow across the face of the nucleant particle to form a thin coating, but can then grow further only by reducing the radius of curvature of its interface with the melt. This radius can not go below the critical value r^* for nucleation at the instantaneous temperature. If the diameter d of the particle is such that $d < 2r^*$, then free growth of the crystal from the particle is not possible, as shown in Fig. 2-7. It becomes possible when the supercooling is increased, thus reducing r^*. The critical condition

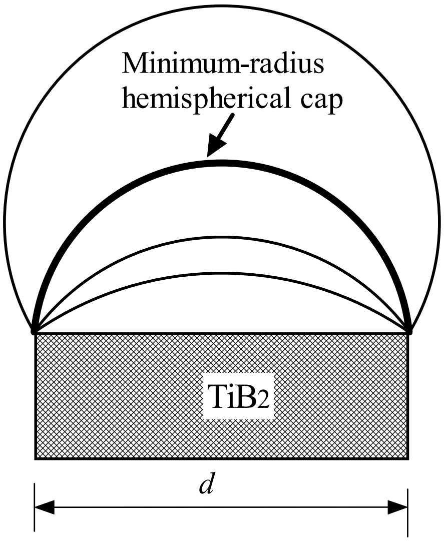

Fig. 2-7. Greer's free-growth model [109,133].

for free growth of the crystal through the minimum-radius hemispherical shape is when $d = 2r^*$. The supercooling for free growth ΔT_{fg} and the nucleant particle diameter d are simply related by

$$\Delta T_{fg} = \frac{4\sigma}{\Delta S_V d} = \frac{2\sigma}{\Delta S_V r^*} \tag{2-13}$$

where σ is the solid-liquid interfacial energy and ΔS_v is the entropy of fusion per unit volume. The supercooling ΔT_{fg} constitutes a barrier for the effective initiation of a new grain.

In an attempt to understand the grain refinement observed in Al–Ti and Al–Zr alloys, Maxwell and Hellawell [134] proposed a model that combines the spherical-cap model with efficient wetting for grain formation on faceted Al_3Ti or Al_3Zr particles. They assumed that a particle will be immediately enveloped as soon as a spherical-cap nucleus forms on a facet of its surface. The subsequent growth of the spherical envelope is a function of the melt supercooling using a spherical growth model. For a given cooling rate, the efficiency of a grain refiner depends on its potential as an inoculant particle and the alloy constitution.

Inspired by the particle-core structures observed in Mg alloys after inoculation with nearly spherical Zr particles, Qian [135] proposed a model for heterogeneous nucleation and grain formation on potent spherical inoculants during solidification on the basis of an adsorption and surface diffusion mechanism, where nucleation is assumed to occur through the formation of an adsorbed layer of atoms. The critical supercooling required for such a nucleation event is proportional to the reciprocal of the inoculant size and is defined approximately by [135]:

$$\Delta T_{crit} = \frac{4\gamma_{SL} T_m}{L_V d_P} \tag{2-14}$$

Effective inoculation with potent spherical particles depends on both the inoculant particle size and the supercooling that the liquid metal experiences during solidification. For a given size of potent spherical inoculant particle, a critical supercooling is still required for nucleation even if the contact angle is zero. Barrierless nucleation appears to be possible only when the particle size approaches infinity under complete wetting conditions.

2.4. Grain Refinement of Mg Alloy Welds by Adding Alloying Elements

When solute elements are added to a metal, the free energy required for nucleation is a function of the solute content and the nucleus size. The solute, which is required to cause a CET, provides the constitutional supercooling necessary for the nucleation and growth of equiaxed grains. The effect of principal phase diagram parameters including m, k, D and C_0 on the constitutional supercooling and then on the CET is now qualitatively well understood [49,64]. Tarshis *et al.* [136] in a classic paper, examined the variation of grain size in binary Ni alloys and Al alloys. The grain sizes of a series of poured binary alloy castings were compared at a fixed level of solute addition. It was demonstrated that a fine grain size can occur in slightly supercooled melts even in the absence of active heterogeneous inoculants. Therefore, it was supposed that solute elements could promote grain formation in certain castings at supercoolings insufficient to cause heterogeneous nucleation. To study the effect of solute elements on the structure of solidifying materials, castings of pure Ni and Al were compared with binary alloys of these base materials. It was found that the relative grain size decreased as the parameter P increased, where P is given by [136,137]

$$P=-mC_0(1-k)/k \qquad (2\text{-}15)$$

At low P values, the structures were columnar, and they changed to columnar-equiaxed and finally equiaxed structures as P increased.

In recent years, when examining the influence of phase diagram parameters, it has become more common to relate grain sizes to the 'growth-restriction parameter', Q [71,133], rather than P, where Q is given by

$$Q= m_l c_0(k-1) \qquad (2\text{-}16)$$

When nucleant particles are added into the molten pool, the grain size of the alloy primarily depends on $1/Q$ [134]. Since c_0 is an approximate constant, the growth restriction factor, Q, is proportional to the $m_l(k-1)$. Table 2-1 presents the data for calculating Q for a variety of elements which could be alloyed to Mg. It can be seen that Fe, Zr, and Ca could be efficient grain refiners of AZ31 Mg alloy since they generate very high values of Q when small amounts of solute are present in the Mg matrix. Therefore, the choice of effective inoculant particles predominantly depends on the alloy being refined, and the resultant grain size (RGS) varies depending the type and amount of added inoculants or alloying elements [49]. The RGS can be calculated using the following equation [49]

Table 2-1. Slope of the Liquidus Line, *m*, Equilibrium Distribution Coefficient, *k*, and Growth Restriction Factor, *m*(*k*-1), of Various Alloying Elements in Magnesium [42,49]

Elements	*m*	*k*	*m(k - 1)*	System
Fe	-55.56	0.054	52.56	eutectic
Zr	-6.90	6.55	38.29	peritectic
Ca	-12.67	0.06	11.94	eutectic
Si	-9.25	≈0.00	9.25	eutectic
Ni	-6.13	≈0.00	6.13	eutectic
Zn	-6.04	0.12	5.31	eutectic
Cu	-5.37	0.02	5.28	eutectic
Ge	-4.41	≈0.00	4.41	eutectic
Al	-6.87	0.37	4.32	eutectic
Sr	-3.53	0.006	3.51	eutectic
Ce	-2.86	0.04	2.74	eutectic
Sc	4.02	1.65	2.61	peritectic
Yb	-3.07	0.17	2.53	eutectic
Y	-3.40	0.50	1.70	eutectic
Sn	-2.41	0.39	1.47	eutectic
Pb	-2.75	0.62	1.03	eutectic
Sb	-0.53	≈0.00	0.53	eutectic
Mn	1.49	1.10	0.15	peritectic

$$\mathrm{RGS} = f_{s,n} = 1 - \left(\frac{m_l c_0}{m_l c_0 - \Delta T_n} \right)^{\frac{1}{1-k}} \tag{2-17}$$

where $f_{s,n}$ is the amount of growth required to develop the supercooling, ΔT_n, necessary for nucleation to occur, m_l is the slope of the liquidus line, c_0 is the composition of the alloy, and k is the partition coefficient. The potency of the nucleant particles and the segregating power of the solute play an important role in determining the final grain size of alloys [42,49,133,138].

2.5. Crystallographic Analysis of Grain Refinement in Mg-Al Alloys

Turnbull and Vonnegut [139] first proposed that the effectiveness of an inoculant particle in promoting heterogeneous nucleation depends on the crystallographic disregistry between the inoculant and the nucleated solid. The disregistry is defined as

$$\delta=(\Delta a/a) \tag{2-18}$$

where a is the lattice parameter of the nucleated phase, and Δa is the difference in lattice parameters between the crystal and the inoculant in a low index plane. When the chemical parameters of the inoculant and the nucleated crystal are similar, the energy barrier to heterogeneous nucleation is minimum for a coherent interface [139].

Reynolds and Teottle [140] investigated heterogeneous nucleation in Zn, Al, Mg, Sn, Pb, Cu, and Sb castings by applying various metal inoculant particles to the surface of sand and metallic molds. They found that the metal inoculant particles that had a crystal structure similar to that of the melt material were effective in promoting nucleation when the lattice spacing difference between the inoculant particle and the melt material was less than 10 pct. If the lattice misfit was greater than 10 pct, the effectiveness of inoculants could be ignored.

After systematic studies of heterogeneous nucleation behaviour of supercooled liquid Fe on various carbides and nitrides, Bramfitt [141] modified the linear disregistry by introducing the following planar disregistry to include crystallographic combinations of two phases with planes of differing atomic arrangements:

$$\delta_{(hkl)_n}^{(hkl)_s}=\sum_{i=1}^{3}\frac{1}{3}\left(\frac{\left|(d_{[uvw]_s^i}\cos\gamma)-d_{[uvw]_n^i}\right|}{d_{[uvw]_n^i}}\right)\times 100\% \tag{2-19}$$

where subscripts *s* and *n* represent the inoculant and the nucleated crystal, respectively; (*hkl*) is a low index plane, [*uvw*] is one of three low index directions in (*hkl*), θ is the angle. Bramfitt [141] suggested that when the planar disregistry is less than about 12 pct, the nucleating inoculant is potent; when the disregistry is above 12 pct, the potency is poor.

In recent years, an edge-to-edge matching model has been developed by Zhang and Kelly [142-144] to predict the orientation relationships (ORs) and actual atom matching across an interface between any two phases, as shown in Fig. 2-8. This model is based on the assumptions that the crystallographic relationships between any two phases are governed by minimization of the strain energy of the interface and that the necessary and sufficient conditions for minimization of the strain energy are the maximum matching of rows of atoms across the interface between the two adjacent phases [143]. In addition to the great success in the prediction and understanding of crystallographic features of phase transformations in solids, this model has recently also been used to elucidate the grain refinement mechanism and efficiency of the refiners and approaches for both Al and Mg casting alloys [144–148]. The

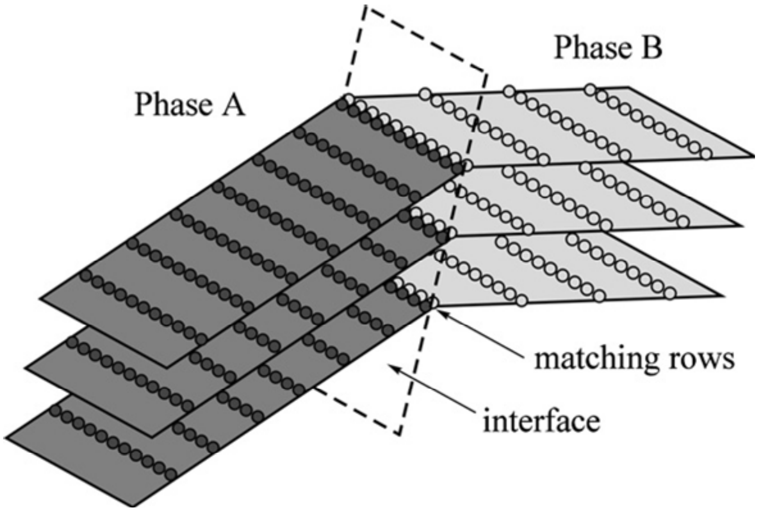

Fig. 2-8. Schematic diagram showing the interface and the essential features of the edge-to-edge matching model (taken from Zhang and Kelly) [142-144].

edge-to-edge matching model is based on the matching of actual atoms, rather than just lattice points in complex crystals where there may be more than one atom associated with each lattice point [144].

Zhang *et al.* [145] examined the actual atomic row matching across the interface between the $Al_8(Mn,Fe)_5$ compound and the Mg matrix and concluded that the crystallographic matching at the interface is so poor that the $Al_8(Mn,Fe)_5$ phase could not provide an effective nucleation site for the Mg grains. This conclusion is supported by recent work of Cao *et al.* [149]. They found that when an Al–60 wt.%Mn master alloy (containing mainly Al_8Mn_5 and a small amount of high temperature ε-AlMn phase) was added to the AZ31 molten alloy, the grain size of as-cast ingots decreased for a short holding time, but increased for a long holding time. Since Al_8Mn_5 is the dominant equilibrium phase at the pouring temperature, the grain coarsening may result from the transformation of the metastable ε-AlMn phase to the Al_8Mn_5 phase during the long period of isothermal holding. Therefore, it was suggested that the high temperature ε-AlMn phase, rather than Al_8Mn_5, is the effective grain refiner [49,149]. Nevertheless, there are still doubts about whether grain refinement can be credited to the ε-AlMn phase. First, the authors of Ref. [49] incorrectly applied the crystallographic data of the ε-AlMn phase to estimate its crystallographic potency; and second there is no convincing evidence to prove that the high temperature ε-AlMn phase can be retained at the low pouring temperature. From a crystallographic point of view, the hcp ε-AlMn phase (a = 0.2697 nm) is more likely to be a nucleant for magnesium grains than the rhombohedric γ_2-Al_8Mn_5 (a = 1.2630 nm) [61,141], as ε has a smaller lattice mismatch (~4% misfit) against Mg (hcp, a = 0.3200 nm) compared to γ_2-Al_8Mn_5 (~20% misfit) [139,141].

2.6. Summary

In the metal casting and welding industries, it is a common practice to introduce inoculant particles into a liquid metal to promote the heterogeneous nucleation and the formation of fine, uniform, and equiaxed grains. Considerable theoretical modelling and experimental examinations have been made to understand heterogeneous nucleation on inoculants of different potency and geometries and the characteristics of dendritic interface growth. Various mechanisms have been proposed to explain the local interaction of columnar grain growth and equiaxed grain formation that gives rise to a CET. However, these vast amounts of detailed results are confusing and sometimes conflicting. There is not a universal criterion to choose the inoculants and not a satisfactory model or equation to be able to incorporate the inoculant properties and the solidification condition. The precise relationship, governing the CET, between inoculant potency, solidification condition, and interfacial properties of inoculant particles in the fusion zones of welds is still far from clear. Therefore, a fundamental understanding of the microstructure refinement mechanism and the dependence of the inoculant potency on the interfacial properties of the inoculants and the solidification condition is of considerable significance.

3. General Methodology

3.1. Materials and Microstructural Examination

The materials used in this study were two commercial grade hot-rolled sheets of AZ31 (SA from Supplier A and SB from Supplier B) Mg alloy, supplied by two different companies, where they were produced through independent processes. The as-receive materials were in H24 temper with thicknesses of 2.0 mm (SA) and 1.5 mm (SB), respectively. The chemical compositions of these alloys were analyzed using an inductively coupled plasma-atom emission spectrometer and mass spectrometer. As Table 3-1 shows, they had similar chemical compositions.

Table 3-1. Chemical Composition of Two AZ31 Alloys (Weight Percent)

Alloys	Al	Zn	Mn	Si	Zr	Ca	RE	Mg
SA	2.92	1.09	0.3	0.01	<0.01	<0.01	<0.01	Bal.
SB	3.02	0.80	0.3	0.01	<0.01	<0.01	<0.01	Bal.

All specimens for metallographic and SEM examinations were cut, cold-mounted, ground, mechanically polished, and then chemically polished for 5 seconds in 10% nital followed by etching for 5 seconds with a solution of 4.2 g picric acid, 10 ml acetic acid, 70 ml ethanol, 10 ml water. The microstructures of the as-received and welded specimens were examined by optical microscope, a JEOL JSM-6460 scanning electron microscope (SEM) equipped with an Oxford ultra-thin window detector energy-dispersive spectrometer (EDS). X-ray diffraction was performed in a Rigaku AFC-8 diffractometer with Cu target, 50 kV acceleration voltage, and 40 mA current.

For transmission electron microscopy (TEM), samples were cut on the base material and the cross-sections of welds using an electrical-discharge machine. Mechanical thinning of discs was continued to a thickness of 100μm by grinding on abrasive papers. The TEM foils were electropolished in a Tenupol 5 (Struers, Ballerup, Denmark) double jet polishing unit in a LiCl + Mg perchlorate + methanol + buthyloxyethanol solution at –45°C. In the final step of sample preparation the foils were subjected to short ion milling on a Fischione 1010 Low Angle Milling and Polishing System in order to remove the surface oxide layer. The TEM investigations were performed with a PHILIPS CM 200 electron microscope equipped with an Oxford ultra-thin window detector EDS operated at 120 kV. The fatigue dislocation substructures were observed with a JEOL JEM-3010 transmission electron microscope operated at 300 kV.

3.2. Resistance Spot Welding and Mechanical Property Measurement

The configuration and dimensions of the welding specimens used throughout the present work are shown in Fig. 3-1. The specimens were cut parallel to the rolling direction of the sheets. The surfaces of the plates were chemically cleaned using 2.5% (w/v) chromic acid before welding to eliminate surface oxidation and contamination, as suggested by previous work [150]. Welding was performed by the conventional RSW technique in a S-400 Robotron 600V single phase A.C. spot welding machine. Crown electrode caps (FF25) with a sphere radius of 50.8 mm and face diameter 16 mm, manufactured from class Cu–Cr–Zr alloy, were used.

The welding conditions are listed in Table 3-2. Six welding samples were welded under each welding condition: three for the tensile-shear test and three for the examination of microstructure. Nugget diameters were measured using metallographic specimens.

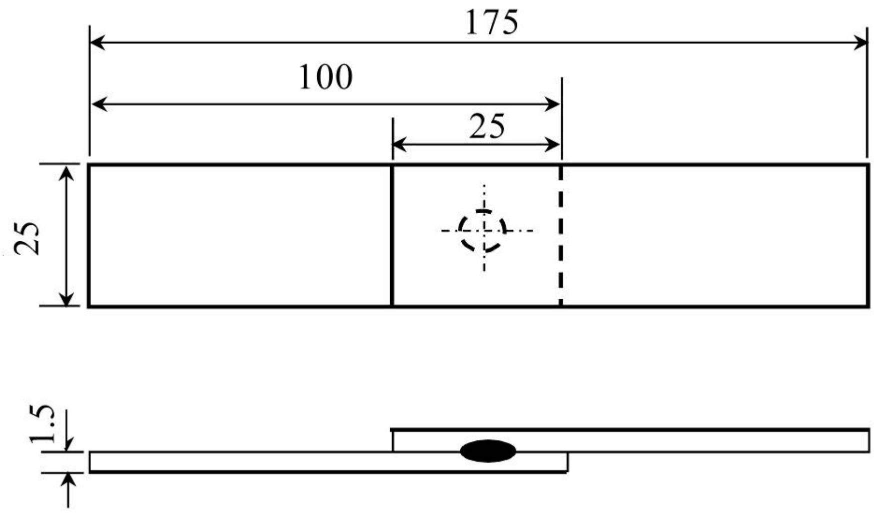

Fig. 3-1. Geometries of resistance spot welding specimens (mm).

Table 3-2. Welding Parameters Selected in this Work

Welding Current (kA)	Electrode Force (kN)	Welding Time (cycles)	Squeezing Time (cycles)	Cooling Time (cycles)
26	4	8	30	30

Furthermore, a variety of welding currents, hold times, and electrode forces were examined. The effect of welding current and hold time on mechanical properties and microstructures of AZ31 Mg alloy welds has been described elsewhere [151].

Mechanical properties of the as-received sheets with a gage of 100 mm × 25 mm × 1.5 mm were measured on an Instron 4206 universal test machine at a constant cross-head speed of 10^{-2} mm/s. The tensile-shear properties of welds were measured using a conventional tensile testing method. The standard tensile loading procedure applied along the longitudinal axis of welding samples produces tensile-shear stress in the welds.

Special care was taken to minimize the effect of misalignment between the axis of the nugget and the bonding axis. The thickness of both end sections of the welded specimens was kept to be the same as the thickness of the welded region by inserting the same thickness of sheets into the grips as shims to prevent bending moments. After failure, fracture surfaces were examined using a SEM.

4. Dependence of Fusion Zone Microstructures and Fatigue Behaviour on Second-phase Particles in Resistance Spot Welds of AZ31 Magnesium Alloys

It is important to characterize the microstructures of resistance spot welds (RSW) in Mg alloys [19,152,153] so as to understand their dependence on inoculant particles in the welds and ascertain an effective method of refining microstructure and improving mechanical properties of Mg alloy welds. The structural application of welded Mg alloy joints requires a detailed understanding of the cyclic deformation resistance so as to predict fatigue life of welded structures, and to ensure the integrity and safety of welded structures in the automotive industry. The effects of welding parameters on tensile-shear mechanical properties have been studied in reference [151]. However, it was unknown how and to what extent the refined microstructure affects fatigue properties of AZ 31 Mg alloy welds.

Both slip and twinning play an important role in maintaining homogeneous plastic deformation in hexagonal-close-packed (hcp) alloys [154,155]. It has been shown that (0002) basal slip is usually the dominant plastic deformation mode in cold deformed Mg alloys [156-161]. A recent study involving a fine-grained AZ31B Mg alloy has indicated that besides (0002) basal slip, nonbasal glide could be activated to maintain the continuity of strain due to stress concentrations at the boundaries [156]. On the other hand, $\{10\bar{1}2\}$ twinning was observed to be easily activated in a coarse-grained cast AZ91 Mg alloy under cyclic loading [157-159]. Twinning was more difficult with a smaller amount of twinning in a fine-grained material than in a coarse-grained one [155,157,160,161]. The further objective of this work is to study the fatigue behaviour of AZ31 Mg alloy resistance spot welds as well as the influence of microstructural refinement on slip and twinning modes during cyclic plastic deformation.

4.1. Experimental Procedures

The materials were two commercial grade hot rolled sheets of AZ31 Mg alloys SA of 2mm and SB of 1.5mm in thickness. In order to eliminate the effect of sample thickness on weldability, and thus permitting direct comparison of weldments and their fatigue lives between the SB and SA alloys, some of the as-received 2.0 mm-thickness alloy SA sheets were mechanically ground from 2mm to 1.5mm in thickness, which is the thickness of the SB alloy. Then, both alloys′ samples were mechanically ground using 600 mesh abrasive papers so as to minimize the effect of surface roughness of samples on welding behaviour. Samples for microstructural characterization and fatigue testing (Fig.3-1) were welded at 26kA. Load-controlled pull-pull low cycle fatigue (LCF) tests were performed on an Instron 8874 servo-hydraulic fatigue testing system at room temperature. A triangular loading waveform was selected. Different cyclic tensile load ranges from 0.3 kN to 3.6 kN were applied at a load ratio of 0.2. The test frequency was 1 Hz, when the load range was larger than 1.6 kN. It was increased to 10 Hz so as to save time, when the load range was less than 1.6 kN.

4.2. Results

4.2.1. Microstructural Characterization across Weld Zones

The base metal′s optical microstructure was found to be comprised of equiaxed grains in the as-received AZ31 Mg alloys, as shown in Fig. 4-1(a) and (b). The average grain size obtained by the linear intercept method was 8.4μm for SA alloy and 7.5μm for SB according to standard ASTM E 112-96 (2004). Ten randomly selected and widely separated fields were used to count the number of times which a test line cuts through individual grains on the plane of polish. Some strips of fine grain, distributed along the hot-rolled direction, were observed in both alloys. No obvious differences in microstructure were observed via optical microscope between SA and SB alloys in the as-received condition.

Macrostructures of nuggets of two AZ31 alloy welds in the cross section are shown in Fig. 4-2(a) and (b). The average nugget size was 7.30 mm × 1.84 mm (±0.05) for the SA alloy, similar to 7.36 mm × 1.94 mm (±0.05)) for the SB alloy. Metallographic examinations were performed to identify microstructural features across the resistance spot welds in each alloy. A variety of structures were observed across the welds, as shown in Figs. 4-3(a) and (b). Each weldment could be roughly divided into four zones with different microstructural features, *i.e.* base metal (BM), heat affected zone (HAZ), columnar dendritic zone (CDZ), where the fraction of columnar dendrite is larger than 50 percent, and equiaxed dendritic zone (EDZ), where the fraction of equiaxed dendrite is larger than 50 percent, in the fusion zone. The main difference in solidification microstructures between welds in the two alloys was in the size of the CDZ in the vicinity of the fusion boundary, as shown in Fig. 4-4(a) and (b), respectively. In the SA alloy, columnar structure was restricted to a narrow strip region of 400μm±10 in

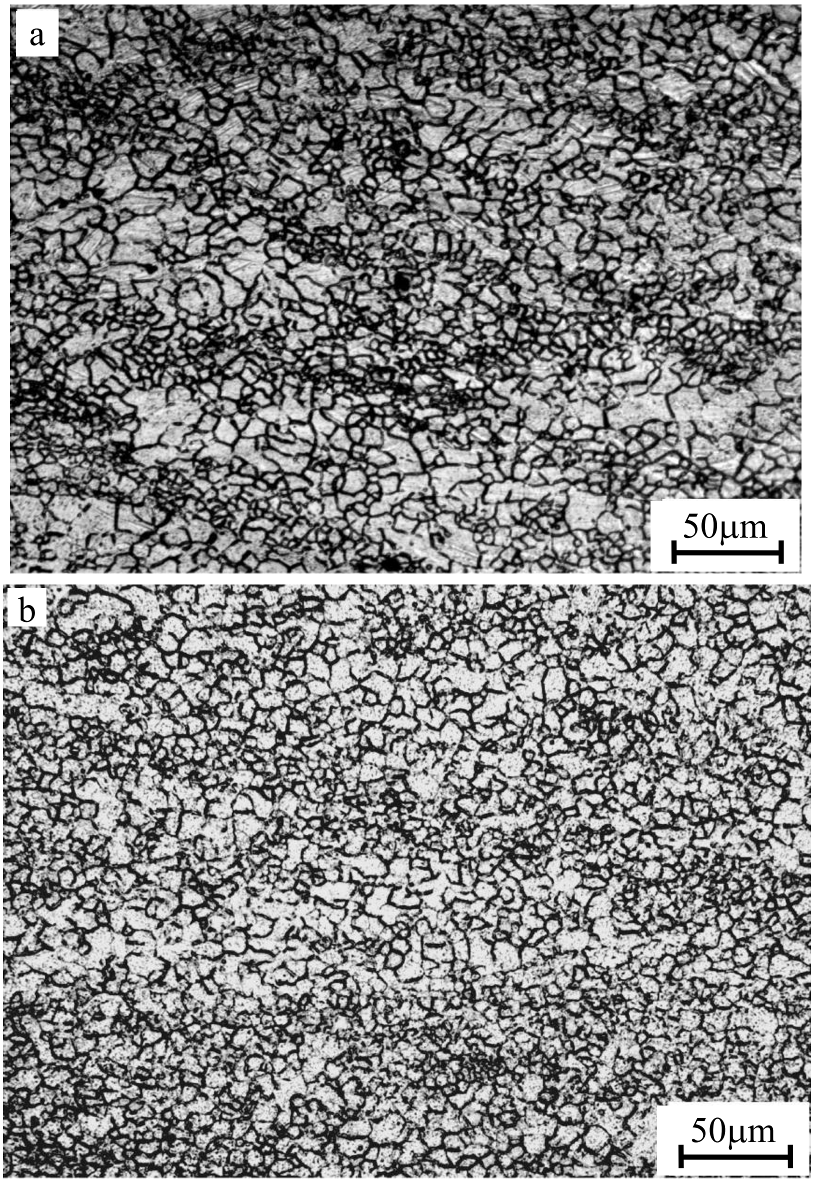

Fig. 4-1. Optical microstructure of two as-received AZ31 alloys in cross section: (*a*) SA alloy and (*b*) SB alloy.

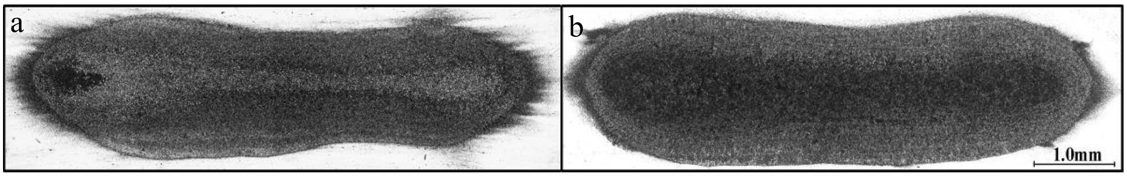

Fig. 4-2. Macrostructures of nuggets of two AZ31 alloy welds in cross section: (*a*) SA alloy and (*b*) SB alloy.

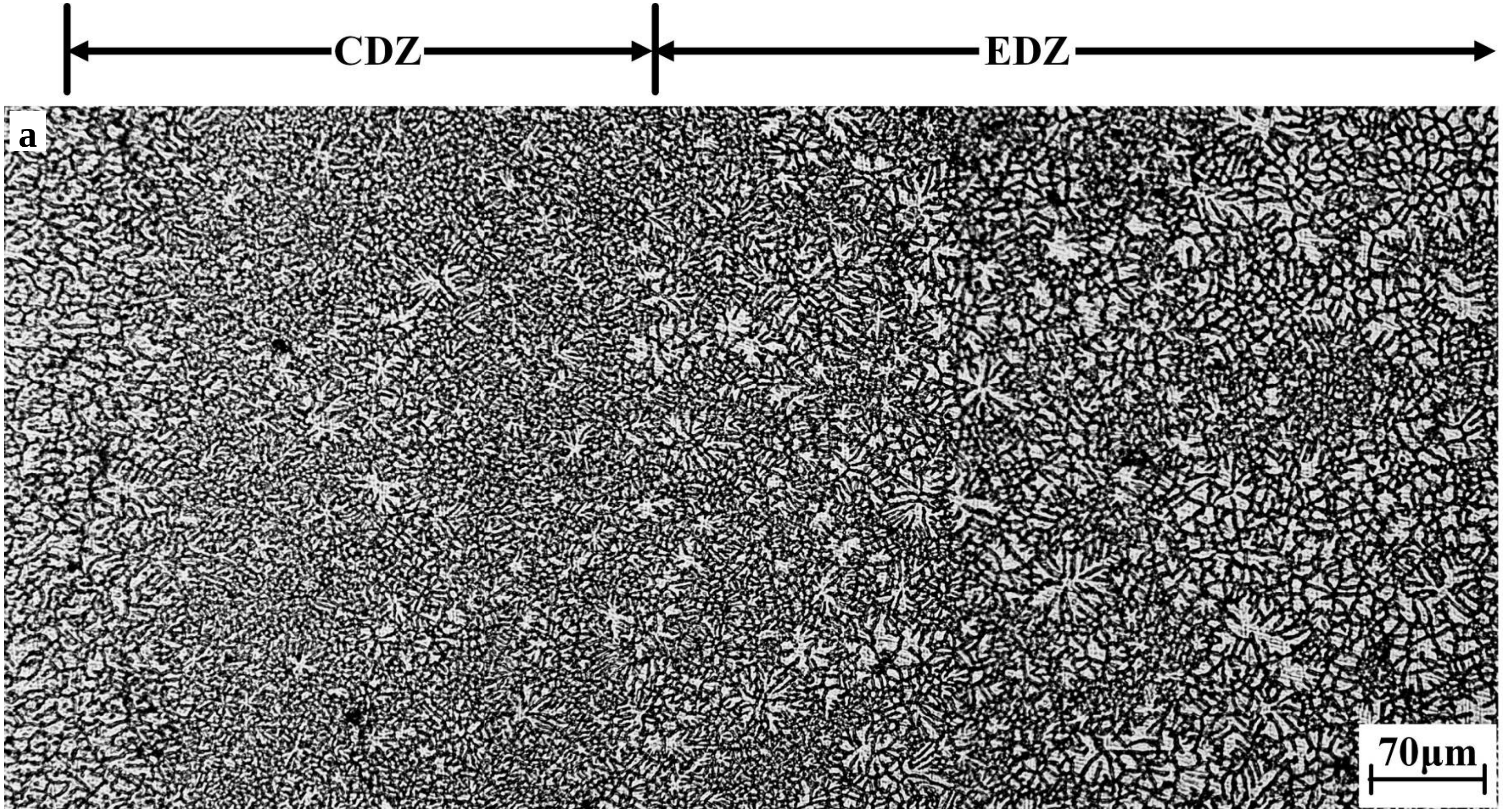
CDZ
EDZ
a
70μm

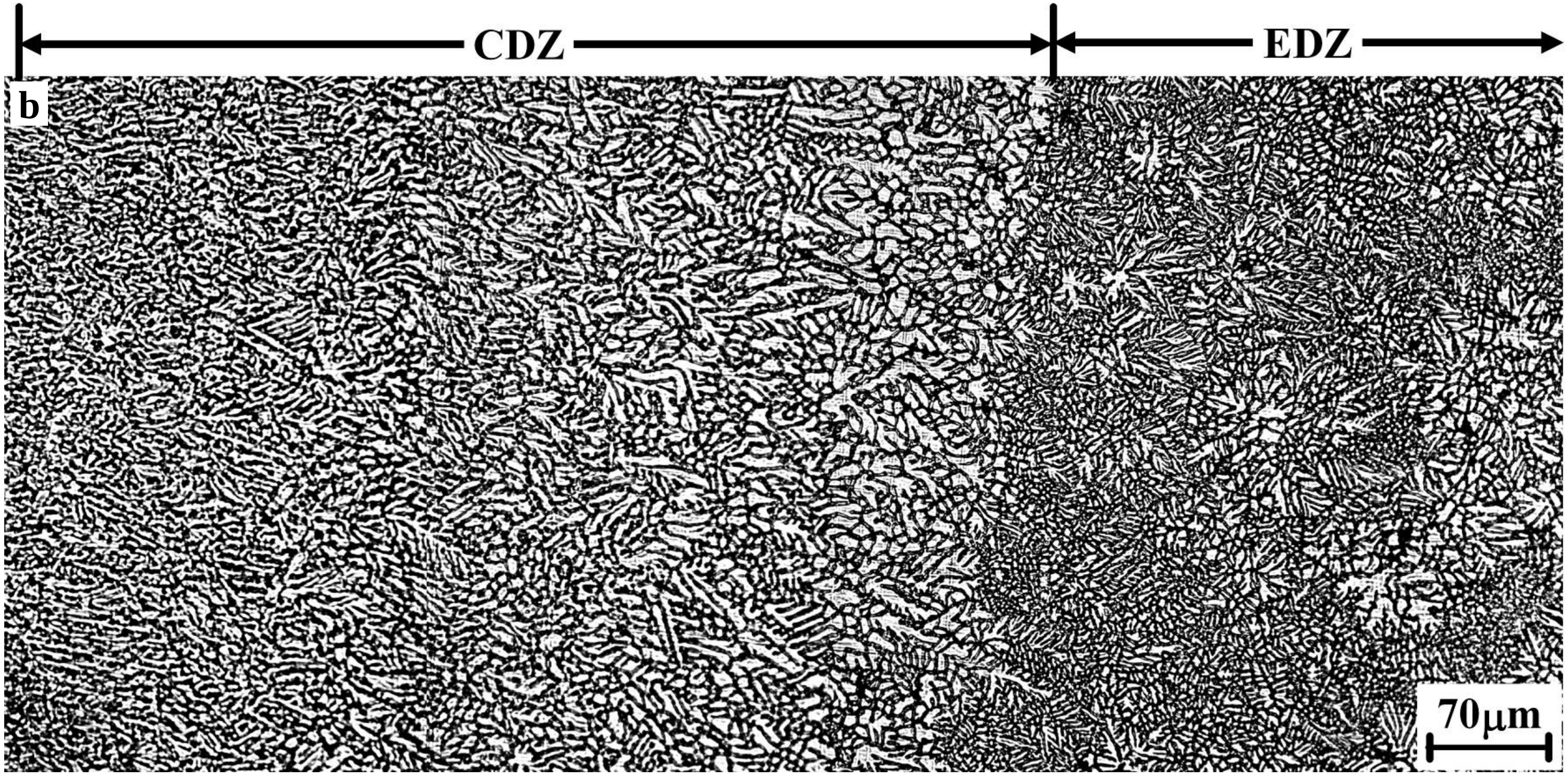

Fig. 4-3. Microstructure variation across RSW AZ31 alloy welds: (*a*) SA alloy and (*b*) SB alloy

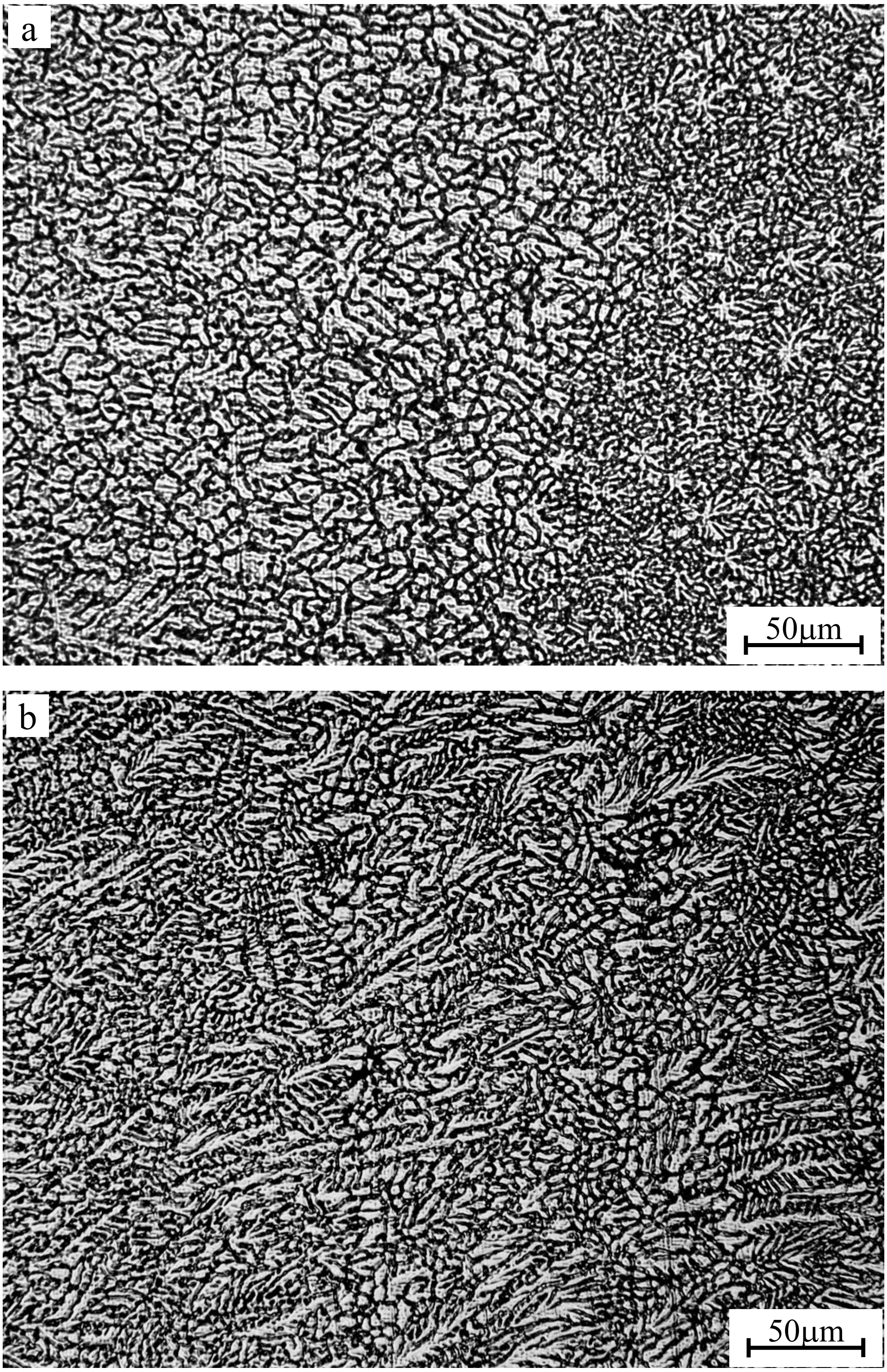

Fig. 4-4. Columnar dendritic zone (CDZ) formed in two AZ31 alloys: (*a*) undeveloped columnar structure in the SA alloy and (*b*) well-developed columnar structure in the SB alloy.

width, and the ratio of length over width of columnar dendritic grains was small (Fig. 4-4(a)). In contrast, well-developed columnar dendritic grains perpendicular to the fusion boundary within a band of 600μm±10 were produced in the SB alloy (Fig. 4-4(b) and Table 4-1). This indicates a much earlier CET in the SA alloy. As the solidification progressed towards the centre of the nugget, equiaxed dendritic structure occurred in both SA and SB alloys, as shown in Figs. 4-5(a) and (b). On a close examination, the diameter of the flower-like dendritic structure, which is equal to the double length of first-order arm of dendrites, in the SA alloy (Fig. 4-5(a)) was found to be smaller than that in the SB alloy (Fig. 4-5(b)). The average diameter of the flower-like dendrites was about 55μm±5 in alloy SA, and 85μm±5 in the SB alloy after counting ten randomly selected and widely separated fields by the linear intercept method according to standard ASTM E 112-96 (2004), as listed in Table 4-1.

Table 4-1. A Comparison of Welding Microstructure between SA and SB

Alloys	Length of CDZ, μm	Diameter of Dendrite in EDZ, μm
SA	400	55
SB	600	85

4.2.2. Microscopic Analysis of Second-phase Particles

4.2.2.1. As –received AZ31 alloys

SEM examination showed that the microstructure in the as-received SA and SB alloys was relatively homogeneous and consisted of an α-Mg matrix together with a large number of submicron white particles, as shown in Fig. 4-6(a) and (b). These white particles were determined later by TEM to be β-$Mg_{17}Al_{12}$. Also, some rectangular and triangular second-phase particles of 4~10 μm in length were observed in the SA alloy, as indicated by an arrow in Fig. 4-6(a). The volume fraction of these large particles in the SA alloy was estimated using a polished planar cross section specimen by the manual point count procedure according to ASTM E562-05 standard. It was about 0.15%. In contrast, second-phase particles of such size were not observed in the as-received SB alloy. Analysis of the large second-phase particles in SA alloy using EDS gave a result of 56.5 at.% Al and 43.5 at.% Mn, as shown in Fig. 4-6(c). Some tiny peaks originating from Au were ignored. Considering the binary phase diagram of Al–Mn [47], a Mn content between 20 and 27 at.% corresponds to $Al_{11}Mn_4$, a Mn content between 37 and 50 at.% corresponds to Al_8Mn_5, and a Mn content above 68 at.% corresponds to β-Mn. Those results suggest that the large particles in Fig. 4-6(a) were primarily Al_8Mn_5. Further examination revealed that the AZ31 microstructure of SA alloy in the as-received condition was composed of hcp α-Mg and sub-micron sized bcc β-phase $Mg_{17}(Al, Zn)_{12}$ precipitates, which was identified by a set of TEM selected area electron diffraction (SAED) patterns, as shown in Fig. 4-7. The shape of the $Mg_{17}(Al, Zn)_{12}$ precipitates was ellipsoidal. When the incident electron beam was parallel to the $[01\bar{1}0]$ zone axis of the Mg matrix, the long axes of the ellipsoidal $Mg_{17}(Al, Zn)_{12}$ precipitates were parallel to the $[2\bar{1}\bar{1}0]$, [0002], and $[2\bar{1}\bar{1}2]$, respectively (Fig. 4-7). The aspect ratio of long and short axes determined using TEM was up to about 5:1, and their maximum length was around 0.12 μm.

A large number of submicron Mn-Al second-phase particles were also observed in both as-received SA and SB alloys. Figs. 4-8(a) through (d) show typical bright-field (BF) and dark field (DF) TEM images of the Al-Mn particles, and the selected area diffraction pattern (SADP) of a thin foil with $[01\bar{1}0]$ zone axis of the Mg matrix in the as-received SA alloy. Some of the second-phase particles gathered as a group, as shown in Fig. 4-8(a). The secondary diffraction

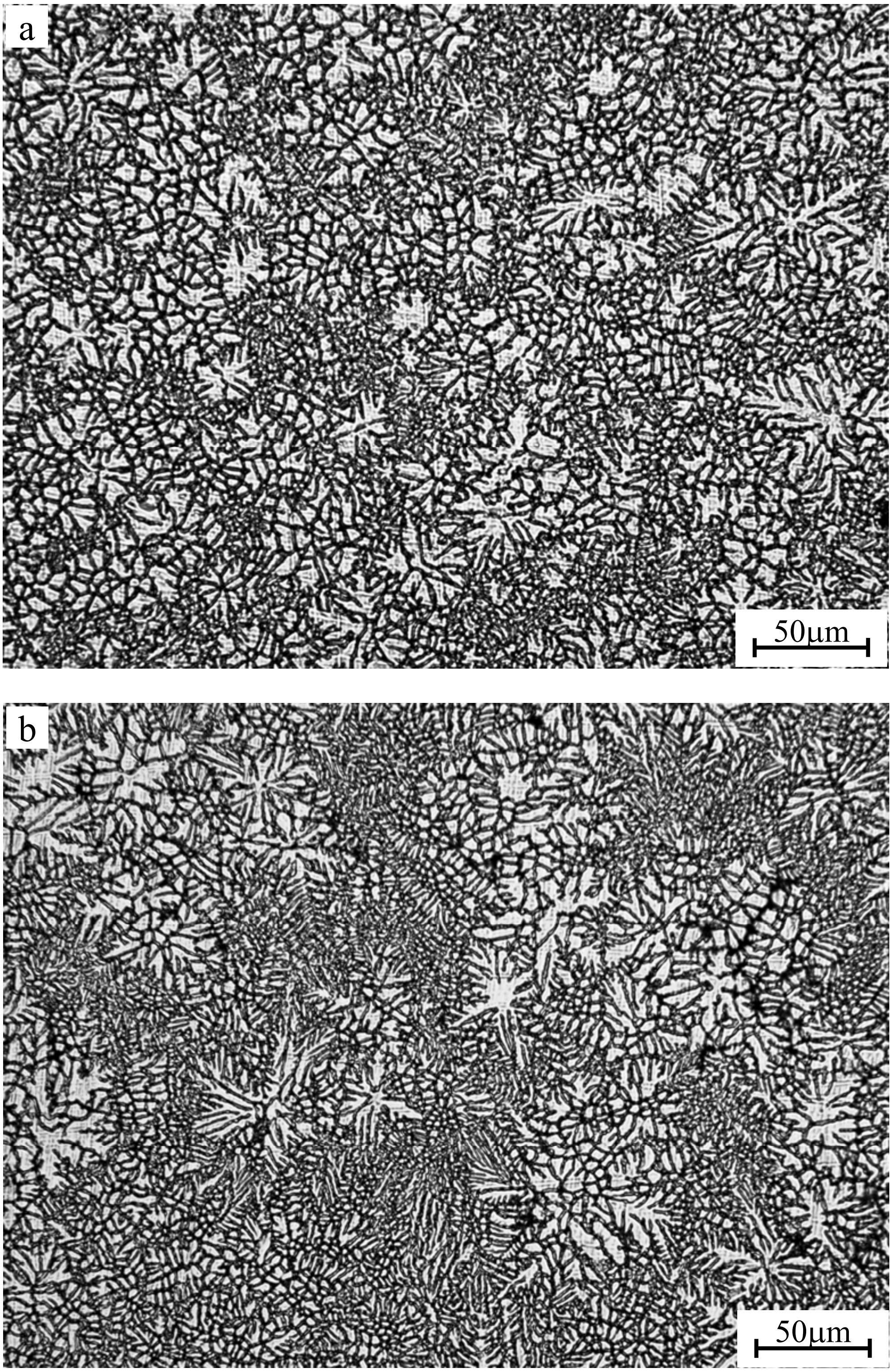

Fig. 4-5. Equiaxed dendrite zone (EDZ) formed in AZ31 alloys: (*a*) SA alloy and (*b*) SB alloy.

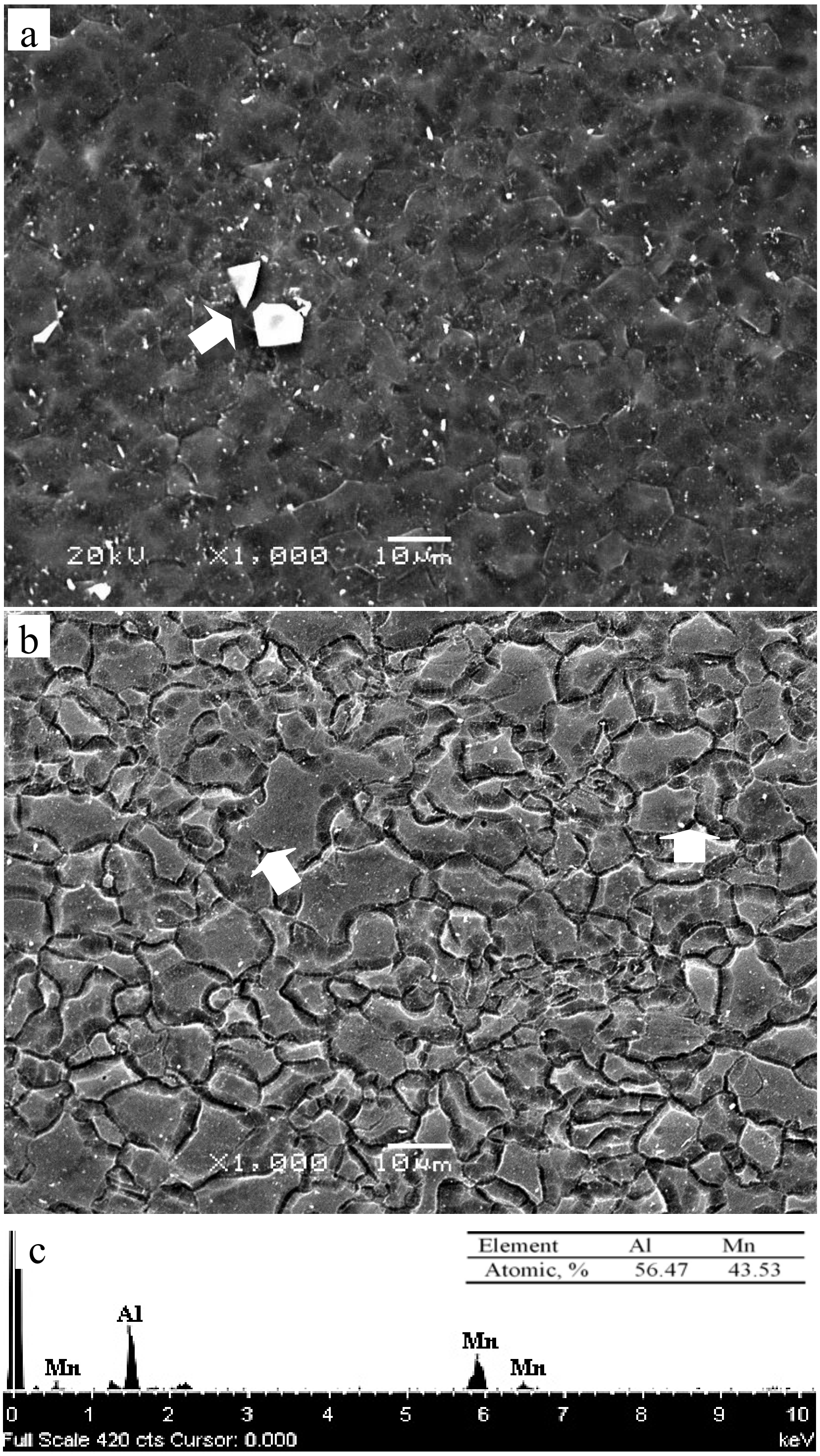

Fig. 4-6. SEM images of the as-received AZ31 SA and SB alloys and EDS analysis of the Al-Mn particles: (*a*) coarse Al-Mn particles as indicated by an arrow in the SA alloy, (*b*) only tiny eutectic β-$Mg_{17}Al_{12}$ particles as indicated by arrows in the SB alloy, and (*c*) EDS analysis of Al-Mn particles in the SA alloy.

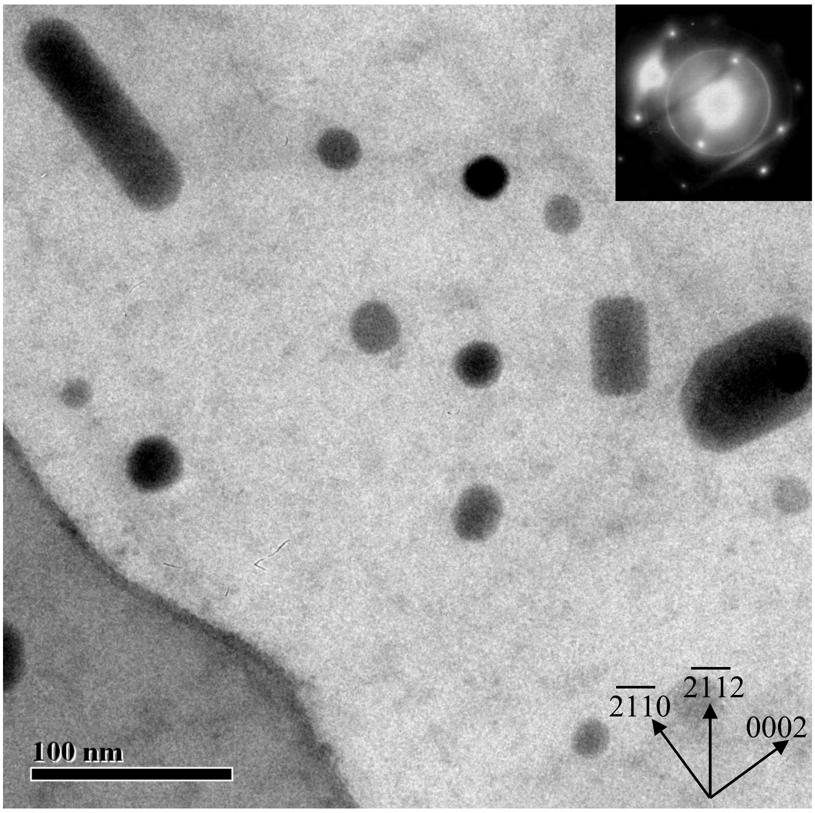

Fig. 4-7. TEM image of $Mg_{17}Al_{12}$ precipitates in the as-received SA alloy, incident beam // $[01\bar{1}0]$.

spots in the SADP in Fig. 4-8(c) and (d) were found to be due to the presence of Al-Mn particles. The TEM dark-field image in Fig. 4-8(b), which was obtained from the $(\bar{1}10)$ reflection presented in Fig. 4-8(c) and (d), shows the sub-micron Al-Mn particle, also indicated by an arrow in Fig. 4-8(a). The analysis of SADP showed that these sub-micron particles were Al_8Mn_5 with a size of 0.130μm single particle and 0.4μm in a group of particles when the zone axis of the Mg matrix is parallel to the $[01\bar{1}0]$. Furthermore, analysis of the second-phase particles using EDS indicated that primary constituent elements were Al and Mn, which is consistent with the results obtained with SEM, as shown in Fig. 4-8(e). This spectrum was obtained in TEM mode with a nominal probe size of 0.15±0.01 μm in diameter, which is

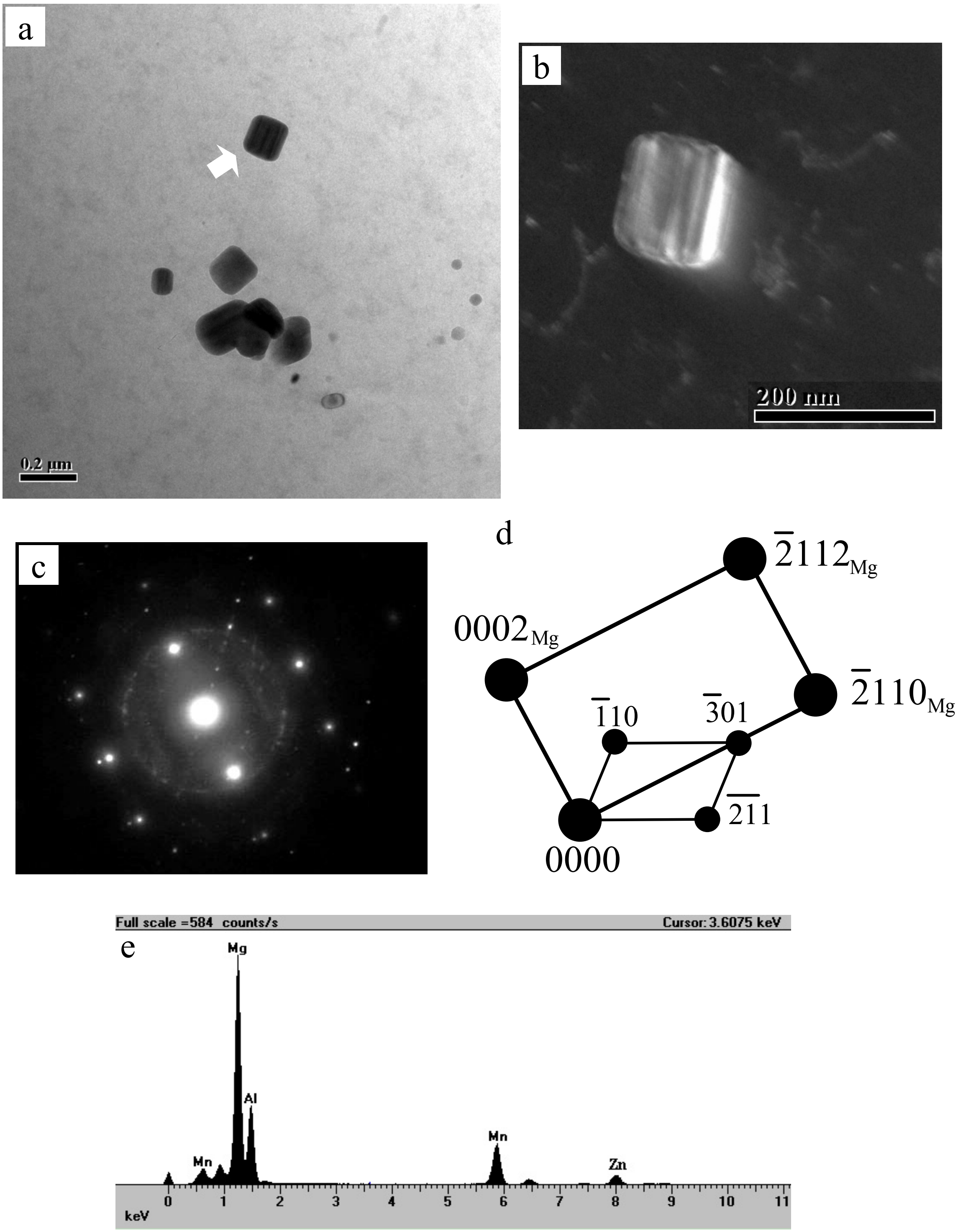

Fig. 4-8. TEM image, selected area diffraction (SAD) and EDS analysis of submicron Al-Mn particles formed in the as-received SA alloy: (*a*) bright field, (*b*) dark field, (*c*) SADP, (*d*) its schematic representation in $[01\bar{1}0]_{Mg}$ zone axis, and (*e*) EDS.

bigger than the diameter of the second-phase particles. Therefore, the peak of Mg together with some peaks of Ni and Zn in the spectrum in Fig. 4-8(e) could be attributed to the contribution from α-Mg matrix. Some tiny Au peaks were ignored. Therefore, these TEM results demonstrated that the second phase particles produced in the as-received SA alloy are Al_8Mn_5.

The same examination was performed on SB alloy in the as-received condition. The typical sub-micron Al_8Mn_5 particles are displayed in Fig. 4-9. The diameter of these particles was around 0.09μm in the form of single particle, and 0.2μm in groups, which is slightly smaller than those formed in the SA alloy.

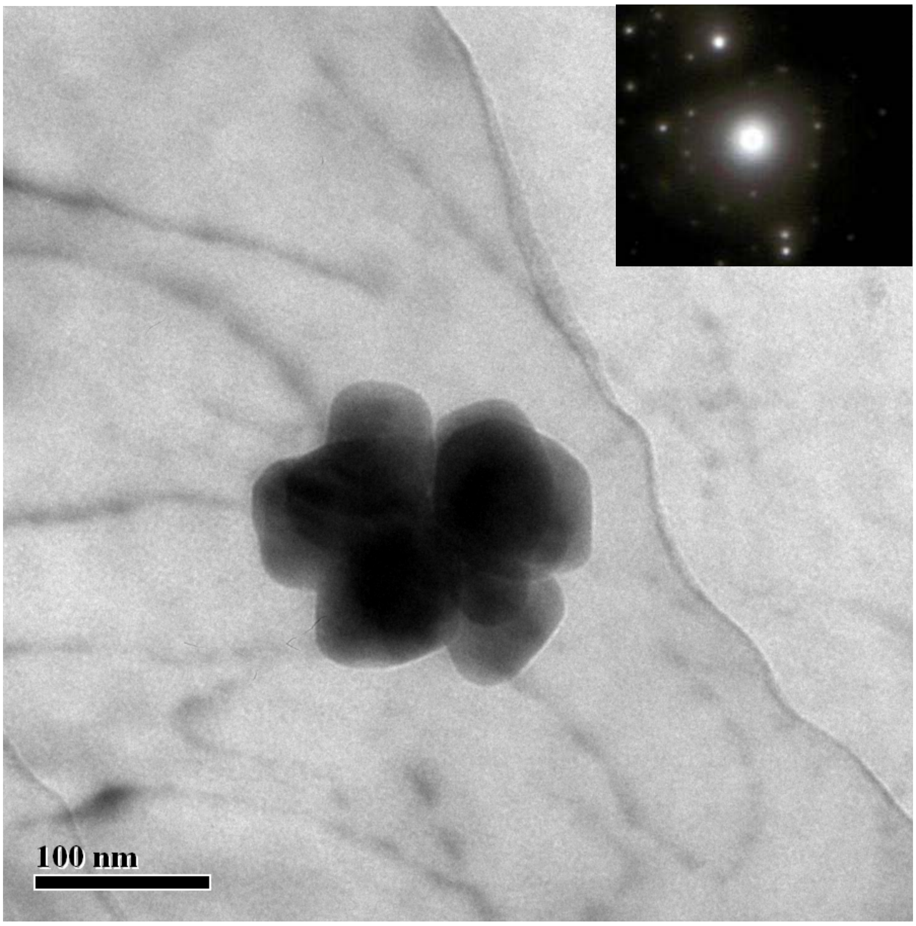

Fig. 4-9. TEM image of submicron Al-Mn particles formed in the as-received SB alloy.

In summary, sub-micron Al_8Mn_5 second-phase particles of 0.09-0.4μm in length were observed to form in both SA and SB alloys in the as-received condition. However, coarse Al_8Mn_5 particles of 4-10μm in length were produced only in the as-received SA alloy.

4.2.2.2. Fusion zone

Figs. 4-10(a) to (c) show the SEM microstructures of second phase particles in the welded SA alloy in HAZ, CDZ, and EDZ regions, respectively. The EDS analysis results are listed in Table 4-2. Coarse second phase particles of 4-10μm in length were detected in each zone, as shown in Figs. 4-10(a) to (c). A comparison of energy dispersive X-ray spectra recorded from the HAZ, CDZ and EDZ in the welded SA alloy in Table 4-1 indicated that the composition of particles was between 35 to 48 at.% for Mn and 45 to 55 at.% for Al, which is similar to those obtained in the as-received SA alloy, in all three zones. This implies that there was not a big effect of welding process on the existence of Al_8Mn_5 intermetallic compounds in the SA alloy. The same SEM examination was carried on the SB alloy welds and no such coarse (*i.e.* 4-10μm) Al-Mn particles were observed in the welded SB specimens.

Figs. 4-11(a) to (d) show TEM images and SADP analysis of small particles observed in alloy SA welds. Bright field (Fig. 4-11(a)), dark field (Fig. 4-11(b)) images and the corresponding SADP (Fig. 4-11(c) and (d)) showed that these particles were Al_8Mn_5 intermetallic compound with a size of about 0.3μm. Similar sized second-phase particles were observed in the welded SB alloy, as shown in Fig. 4-12(a) and (b). From EDS analysis ~35 at.% Mn and ~65 at.% Al were determined in the particles, indicating that they were also Al_8Mn_5.

In brief, two scales of particles were observed in the two AZ31 Mg alloys in the as-received and welded conditions. Micron-sized Al_8Mn_5 particles of 4-10μm in length were only observed

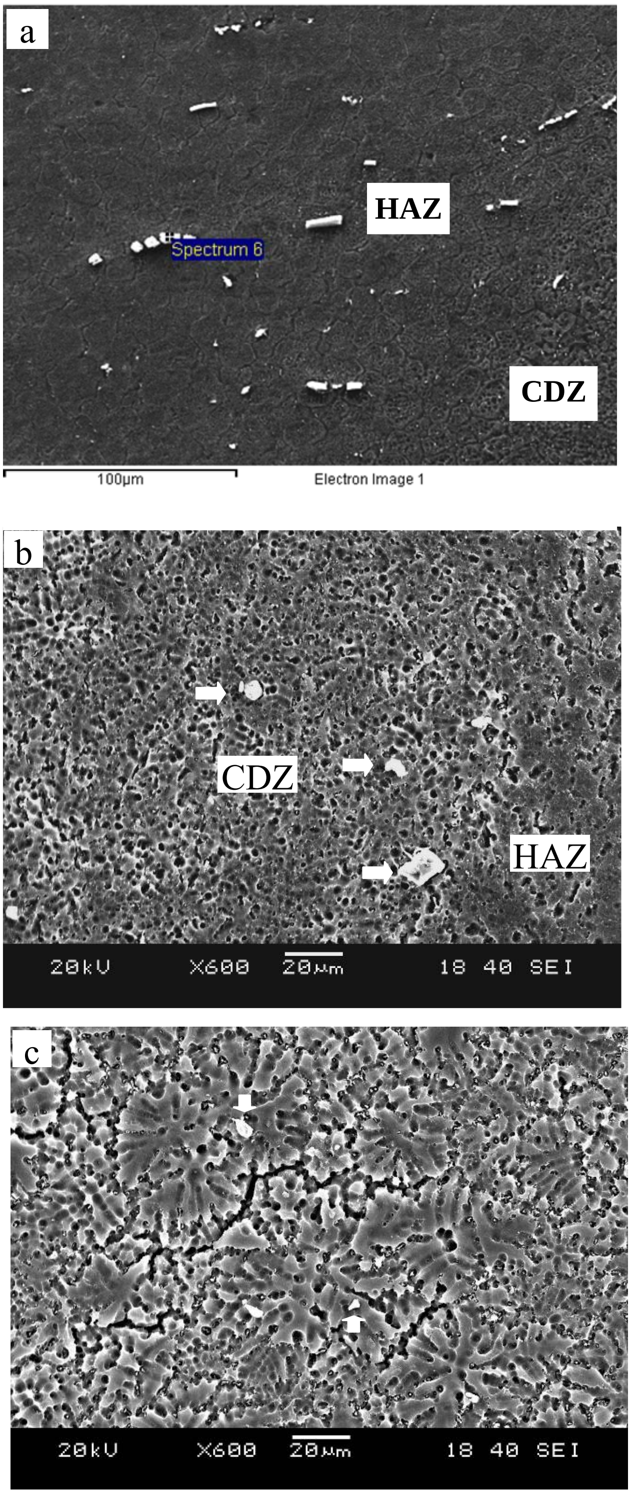

Fig. 4-10. SEM image of Al-Mn particles formed in the RSW welded SA alloy at different zones: (*a*) HAZ, (*b*) CDZ, and (*c*) EDZ.

Table 4-2. EDS Analysis Results of Al-Mn Particles Formed in RS W Welds in A Alloy at Different Zones

Element	Atomic%		
	HAZ	CDZ	EDZ
Mg, K_α	19.65	/	6.81
Al, K_α	45.07	52.87	48.80
Mn, K_α	35.28	47.13	44.38

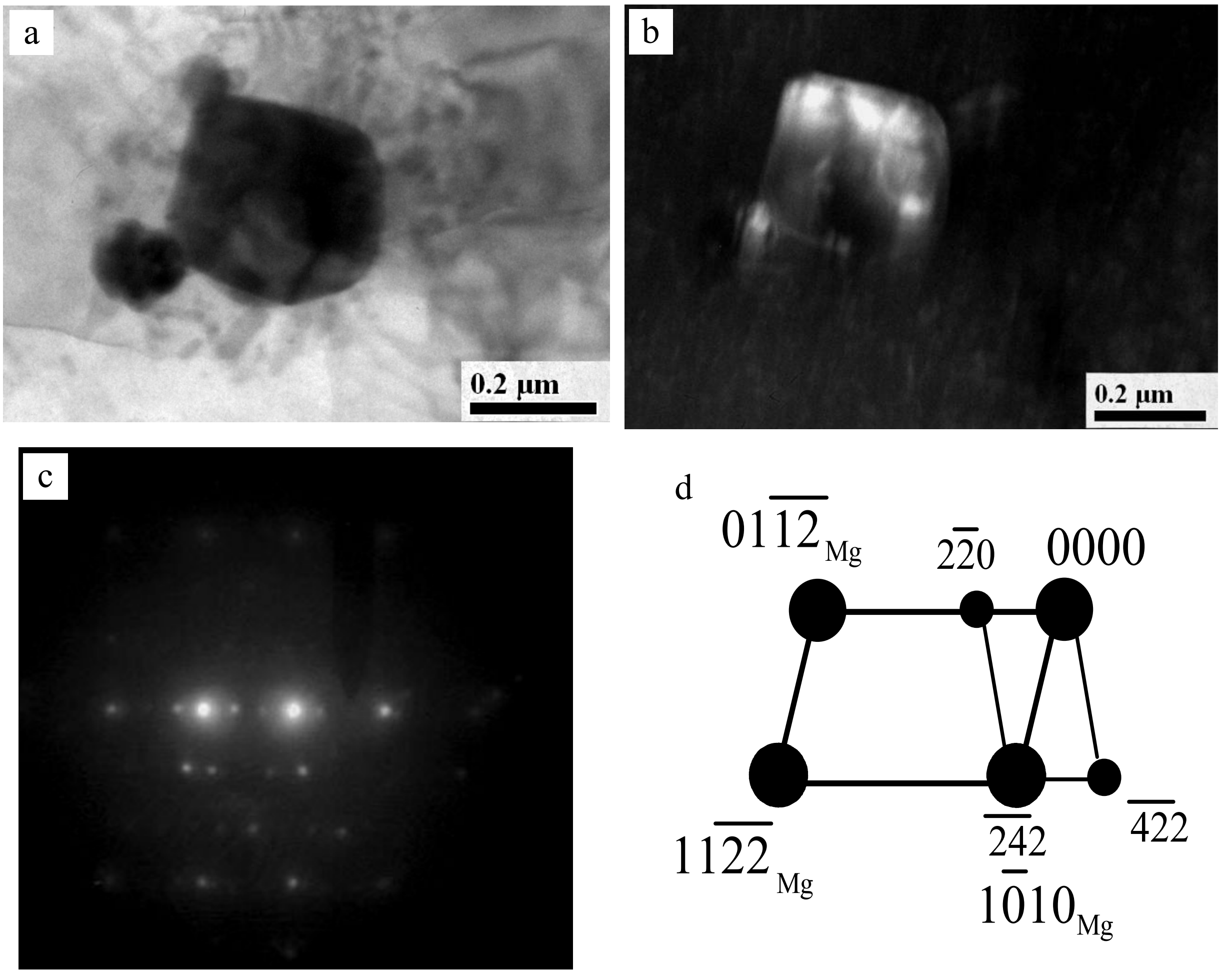

Fig. 4-11. TEM image, SADP and EDS analysis of the Al-Mn-Zn particles in the SA alloy: (*a*) bright field, (*b*) dark field, (*c*) SADP, and (*d*) its schematic representation in $[2\bar{4}2\bar{3}]_{Mg}$ zone axis.

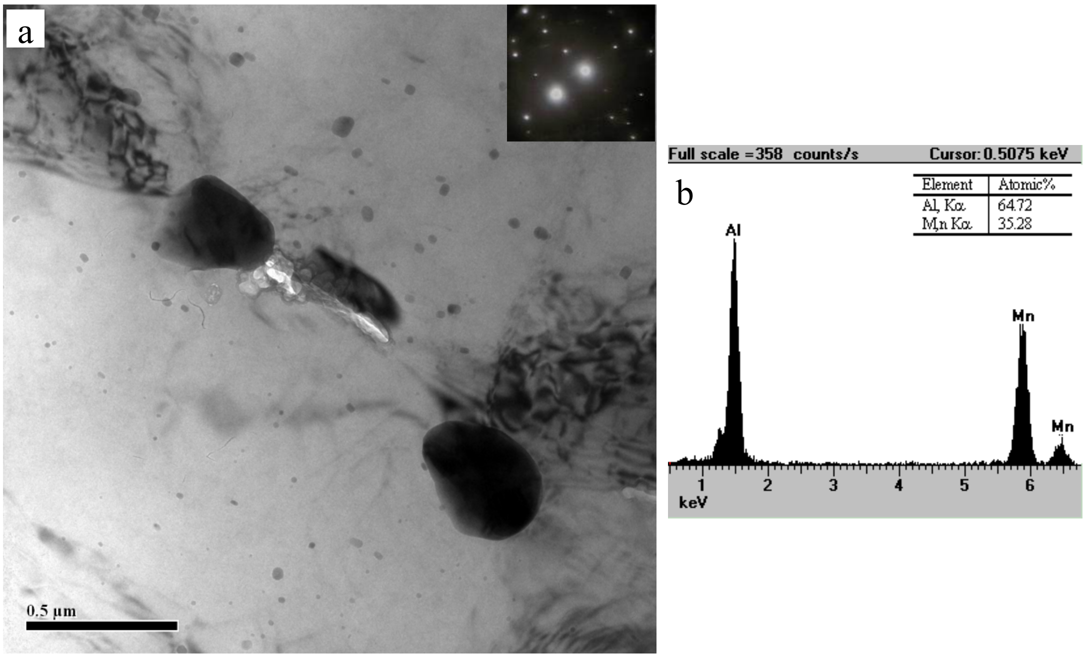

Fig. 4-12. TEM image and EDS analysis of the Al-Mn particles in the SB alloy: (*a*) TEM image and (*b*) EDS.

in the as-received and welded SA alloy. Submicron Al_8Mn_5 second-phase particles of 0.09-0.4µm in length were detected in both SA and SB alloys in the as-received and welded conditions. The welding process did not have a great effect on the existence and size of Al_8Mn_5 second-phase particles in both SA and SB alloys.

4.2.3. XRD Examination of Two AZ31 Alloys in the As-received and Welded Conditions

Phases formed in the as-received AZ31 SA and SB alloys were identified by X-ray diffraction analysis, as shown in Fig. 4-13(a). Peaks of α-Mg, β-$Al_{12}Mg_{17}$ and Al_8Mn_5 were formed in the as-received SA and SB specimens. Further analysis demonstrated that the α-Mg produced the most intense peaks. Well-defined Al_8Mn_5 reflections were displayed, as well. Fig. 4-13(b) shows the XRD spectra of the two welded AZ31 alloys in the fusion zones. The results of XRD analysis showed that besides Mg solid solution, β-$Mg_{17}Al_{12}$ and Al_8Mn_5 intermetallic compounds appeared in the fusion zone. These results have also confirmed the existence of Al_8Mn_5 intermetallic compound in the welded SA and SB alloy specimens. In comparison with the as-received AZ31 alloys, the reflection peaks of the Al_8Mn_5 declined in the fusion zones in both alloys. In addition, some $Mg_{17}Al_{12}$ peaks were also identified by XRD in the fusion zones, as shown in Fig. 4-13(b).

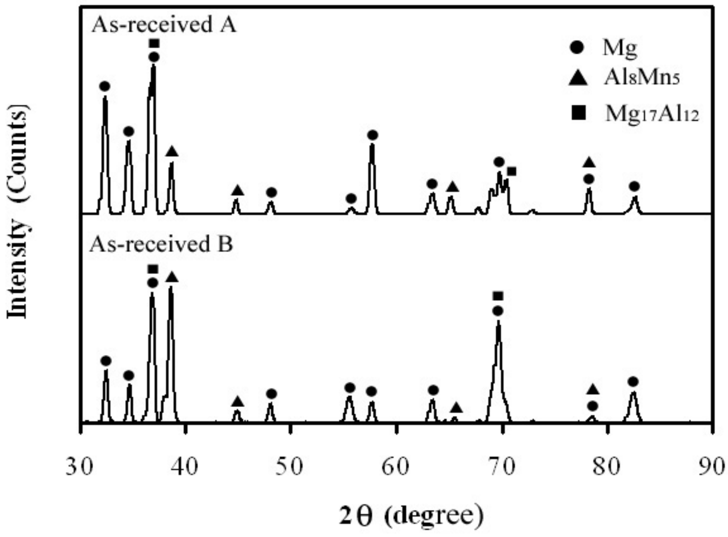

(*a*)

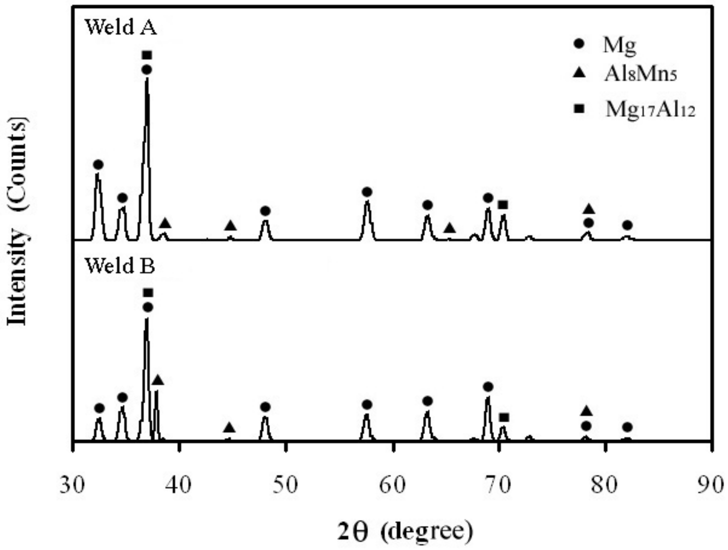

(*b*)

Fig. 4-13. XRD test results of the AZ31 alloys: (*a*) as-received condition and (*b*) welds.

4.2.4. A Comparison of Fatigue Behaviour and Dislocation Substructures

The coarse Al_8Mn_5 particles were observed to promote microstructure refinement of AZ31 Mg alloys. The pre-existing micro-sized Al_8Mn_5 intermetallic particles were observed to act as nucleation sites for α-Mg grain formation resulting in an early columnar-equiaxed-transition (CET) and refinement of microstructure in the fusion zone during solidification of the AZ31 Mg alloy welds [153]. The fatigue life was compared and the cyclic plastic deformation mode was analysed in SA and SB welds so as to evaluate the effect of grain refinement on mechanical behaviour of AZ 31 Mg alloy welds.

4.2.4.1. Fatigue life

Macroscopic examination revealed that failure modes of AZ31 Mg alloy welds during fatigue could be divided into interfacial failures and through thickness failures, as shown in Fig. 4-14. Fatigue cracks were observed to initiate and propagate parallel to the loading axis across the heat-affected and fusion zones, causing interfacial failure through nuggets, when the cyclic load range was higher than about 2.3 kN, as shown in Fig. 4-14(a). In contrast, fatigue cracks initiated in the heat-affected zone and propagated across circumferential base metal perpendicular to the loading axis, leading to through thickness failure, when the cyclic load range was below about 1.7 kN, as shown in Fig. 4-14(b).

Fig. 4-15(a) shows the low cycle fatigue (LCF) lives of the two types of AZ31 Mg alloy welds as a function of cyclic load range (ΔP). The LCF lives of SA welds were basically longer than those of SB at the same cyclic load range, when the cyclic load range was larger than 0.5 kN. However, the fatigue lives between SA and SB welds were similar when the cyclic load range decreased to lower than 0.5 kN. On a close examination, when the interfacial failure took

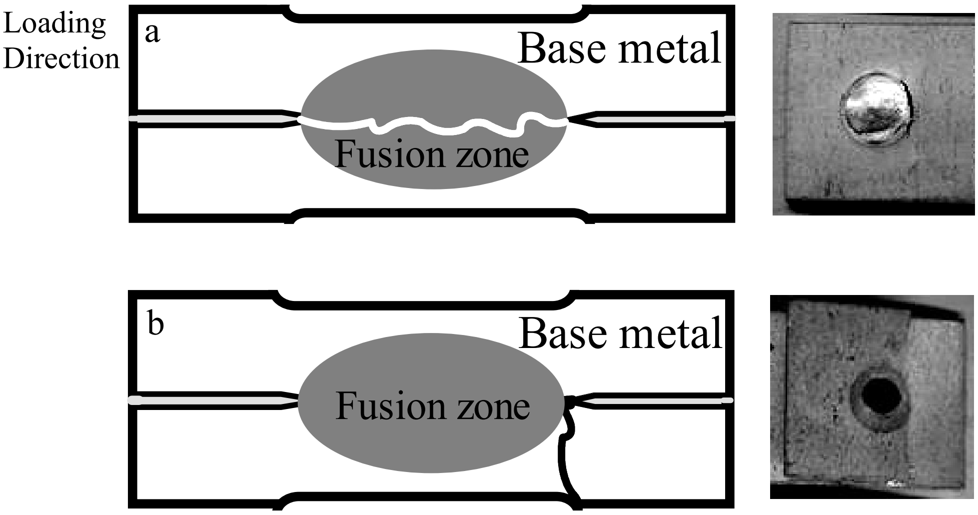

Fig. 4-14. Schematic illustration of fatigue failure mode: (*a*) interfacial failure at a higher cyclic load range and (*b*) through thickness failure at a lower level of cyclic load range.

place, *i.e.*, when the cyclic load range was higher than about 2.3 kN, the SA welds had a higher LCF life than SB welds, as indicated by solid circles and triangles in the upper-left side of Fig. 4-15(a)). However, when the through thickness failure occurred, *i.e.*, the cyclic load range was less than about 1.7 kN, the difference in fatigue lives between two AZ31 Mg alloy welds was small, as indicated by empty circles and triangles in the low-right side of Fig. 4-15(a).

To evaluate the effect of refined microstructure on the fatigue life of Mg alloy welds, it was necessary to eliminate the effect of the thickness of as-received sheets. Zhang [162,163] has successfully used cyclic stress intensity factor range (ΔK) to compare the fatigue lives of resistance spot welds joining two overlapping sheets with different thicknesses, when interfacial failure occurred. The ΔK was defined as follows:

$$\Delta K = 0.694\frac{\Delta F_t}{d\sqrt{t}} \tag{4-1}$$

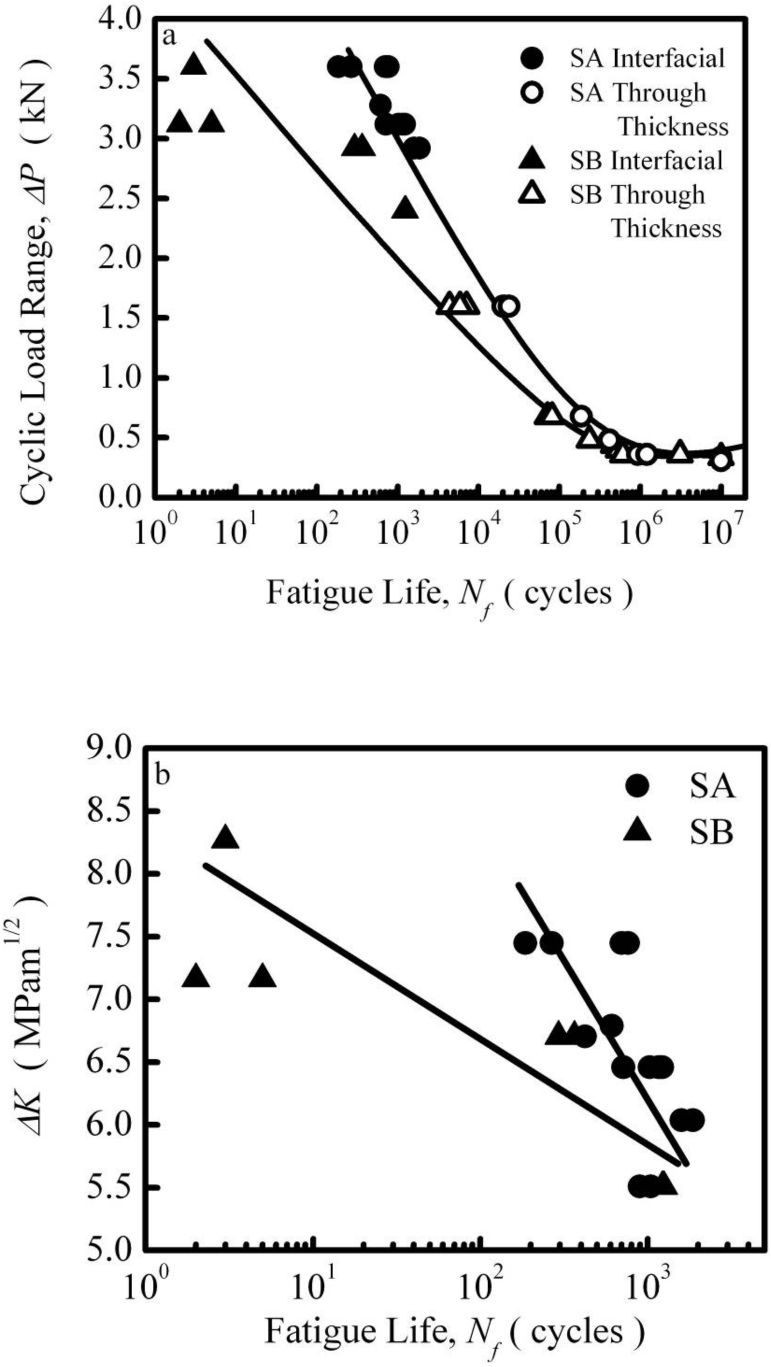

Fig. 4-15. Fatigue life curves of AZ31 Mg alloy welds: (*a*) ΔP vs. N_f and (*b*) ΔK vs. N_f.

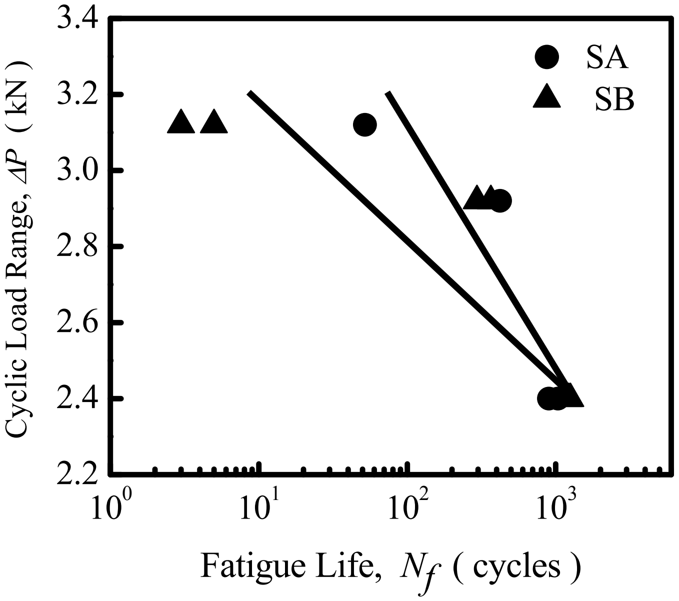

Fig. 4-16. A comparison of fatigue life curves between SA and SB Mg alloy welds made with an identical thickness of 1.5 mm.

where ΔF_t is the load range at failure, d is the nugget diameter and t is the sheet thickness. In order to compare the fatigue lives of two groups of AZ 31 Mg alloy welds with different thicknesses, the fatigue life curves were re-plotted as a function of cyclic stress intensity factor range in the cyclic loading range larger than 2.3 kN, *i.e.* the range of interfacial failure, or corresponding to the cyclic stress intensity factor range larger than 5.3 $\mathrm{MPam}^{1/2}$, as shown in Fig. 4-15(b). SA welds still had the longer fatigue lives than SB welds. Both alloys had a similar fatigue life at the lower level of cyclic stress intensity factor ranges.

Some of the alloy SA sheets were further mechanically ground from 2 mm to the thickness of the SB alloy (1.5 mm) in order to eliminate the effect of sheet thickness. Both alloy samples were mechanically ground up to 600 mesh abrasive paper to minimize the effect of surface roughness of samples on welding behaviour. Both SA and SB were welded using the same welding conditions. Fig. 4-16 illustrates a comparison of fatigue lives between SA and SB welds with the same thickness of 1.5 mm; all welds in this comparison fractured with interfacial failure due to the high cyclic loading range. Once again, SA welds exhibited longer fatigue lives than those of SB welds at the same high cyclic load range. The difference of fatigue lives dramatically decreased as the cyclic loading range decreased.

Typical fractographs of interfacial failure cases are shown in Fig. 4-17. Fatigue crack propagation was characterized by typical fatigue striations, which were taken as evidence of transgranular mode, as shown in Fig. 4-17(a) and (b). Many plastic tear traces were observed, as indicated by arrows in Fig. 4-17(a) and (b). Further examination showed that the spacing of fatigue striations on the SA weld fracture surfaces (Fig. 4-17(a)) was smaller than that of SB welds (Fig. 4-17(b)) tested at the same cyclic load range of 3.12 kN, corresponding to a slower crack propagation rate and longer fatigue life of SA welds in Figs. 4-15 and 4-16. The smaller fatigue striation spacing in the SA welds could be attributed to the finer dendritic structure in the fusion zone of SA welds compared to the SB welds, as shown in Fig. 4-17 and also explained in [156].

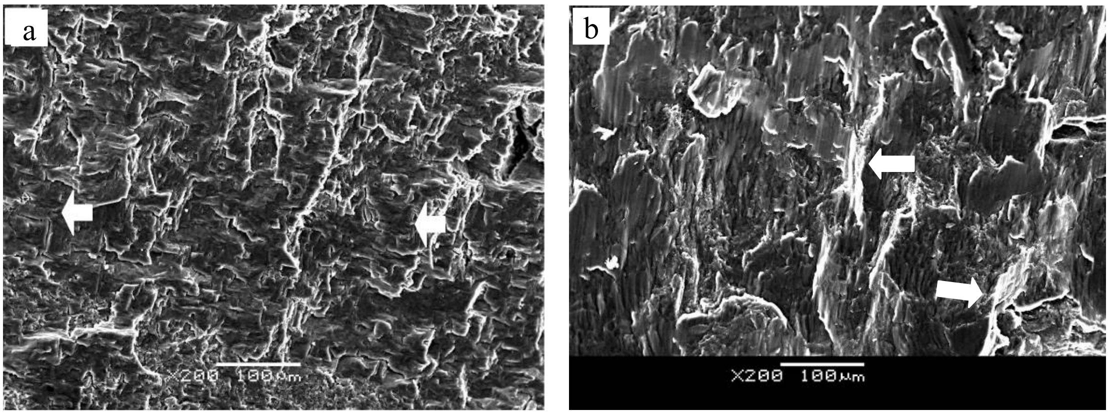

Fig. 4-17. A comparison of fatigue crack propagation zones in the AZ31 SA and SB welds at higher cyclic load ranges: (*a*) SA and (*b*) SB.

The fact that the SA welds had a longer fatigue life than SB when the interfacial failure occurred in the fusion zone at a higher cyclic load range implied that the fatigue resistance of fusion zones in SA welds was better than that in SB welds. Therefore, the subsequent detailed microstructure and dislocation substructure characterization has focused on the fusion zones of these welds.

4.2.4.2. Cyclic deformation substructure

The deformation substructures in the SB welds fatigue tested at different cyclic load ranges is shown in Fig. 4-18(a) and (b). Typical dislocation configuration comprised parallel dislocation lines, which were shown to be mostly arranged along (0002) slip planes, when the incident electron beam was parallel to the $[01\bar{1}0]$ zone axis, as shown in Fig. 4-18(a). Under this observation condition, the basal planes vertically intercepts with the TEM foil surface. Therefore, straight dislocation segments lying parallel to the basal plane traces represent slip in the basal system. It is seen from Fig. 4-18(a) that the majority of dislocation segments were parallel to the basal slip plane trace. Further examination showed that some basal dislocation segments extended out of the basal plane trace, as indicated by arrows in Fig. 4-18(a). The formation of these curved dislocation lines could be attributed to the cross-slip of dislocations from the basal plane to non-basal planes, as the slipping dislocations were accumulated and blocked at obstacles on their basal planes. When the cyclic load range increased to 3.65 kN, substantial cross-slip to non-basal planes occurred leading to a rapid increase of dislocation density on the non-basal planes. As a result, the fatigue dislocation configuration evolved from parallel dislocation lines to parallelogram dislocation cells, as shown in Fig. 4-18(b). Further examination showed that elongated dislocation lines were observed to pass the fine second-phase particles of about 0.1 μm in diameter, as indicated by an arrow in Fig. 4-19. In short, parallel dislocation lines were the typical dislocation pattern and planar basal slip was a predominant plastic deformation mode in the fatigued SB welds. Similar dislocation configurations and plastic deformation features have been observed in cyclically-deformed hcp Mg, Ti, and Zr samples by other researchers [156, 164-166].

Typical deformation substructure was composed of elongated dislocation cells in SA welds fatigue tested at different cyclic load ranges, when the incident electron beam was parallel to the [$01\bar{1}1$] zone axis, as shown in Fig. 4-20(a) and (b). Dense dislocation lines interacted with each other and developed into elongated dislocation cells when the cyclic load range was 2.92 kN (Fig. 4-20(a)). Obvious dislocation-free zones were observed around the Al_8Mn_5 particles of about 1 μm in diameter, as indicated by arrows in Fig. 4-20(a). This implies that the resistance to dislocation slip in the SA welds with larger Al_8Mn_5 particles was larger than that in the SB welds with finer Al_8Mn_5 particles during cyclic deformation (Fig. 4-19). Dislocation density increased as the cyclic load range increased to 3.65 kN; however, the cell dislocation configuration still remained, as shown in Fig. 4-20(b). Dense dislocation lines were visible, when the operation vector, $\boldsymbol{g}$, was equal to [0002] (Fig. 4-20(b)). This implies that $\langle \boldsymbol{c}+\boldsymbol{a} \rangle$, or more precisely, $1/3\langle 11\bar{2}3 \rangle$ pyramidal slip was activated in the fatigue tested SA welds, according to the $\boldsymbol{g}\cdot\boldsymbol{b}$ invisible criterion. Dislocations having a Burgers vector of $\langle \boldsymbol{a} \rangle$ were out of contrast when $\boldsymbol{g}$ was equal to [0002]. Basal slip together with $\langle \boldsymbol{c}+\boldsymbol{a} \rangle$ pyramidal multiple slips were the primary plastic deformation features in the fatigued SA welds.

Twinning was observed to occur and acted as another plastic deformation mode in both the fatigued SB and SA welds, as shown in Fig. 4-21(a) and (b). This was related to the fact that the dendrite cell size in both SB and SA welds was sufficiently large (i.e., ~55 μm in SA welds,

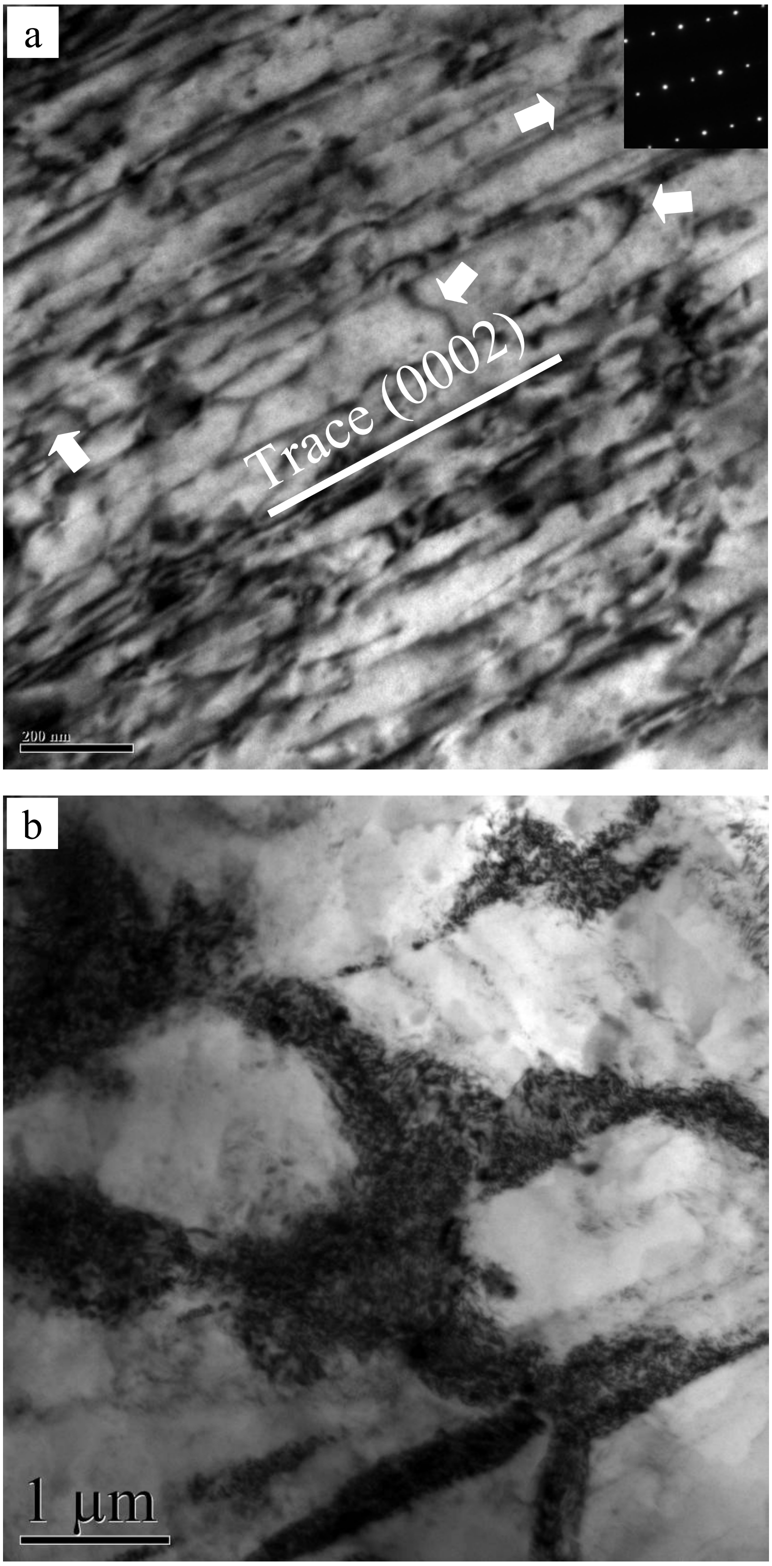

Fig. 4-18. Fatigue deformation structures in the SB welds at different cyclic load ranges: (*a*) ΔP=2.92 kN, N_f=125 cycles, incident beam $/\!/ [01\bar{1}0]$ and (*b*) ΔP=3.65 kN, N_f=294 cycles.

and ~85 μm in the SB welds). However, it appeared that the twins were wider and longer in the SB welds (Fig. 4-21(a)) with coarser dendrite cells (Fig.4-5(b)) compared to the SA welds (Fig. 4-21(b)), which had finer dendrite cells (Fig.4-5(a)). These observations suggest that twinning in the fine-grained welds would be more difficult. This is also in agreement with the observations reported in [157,159-161].

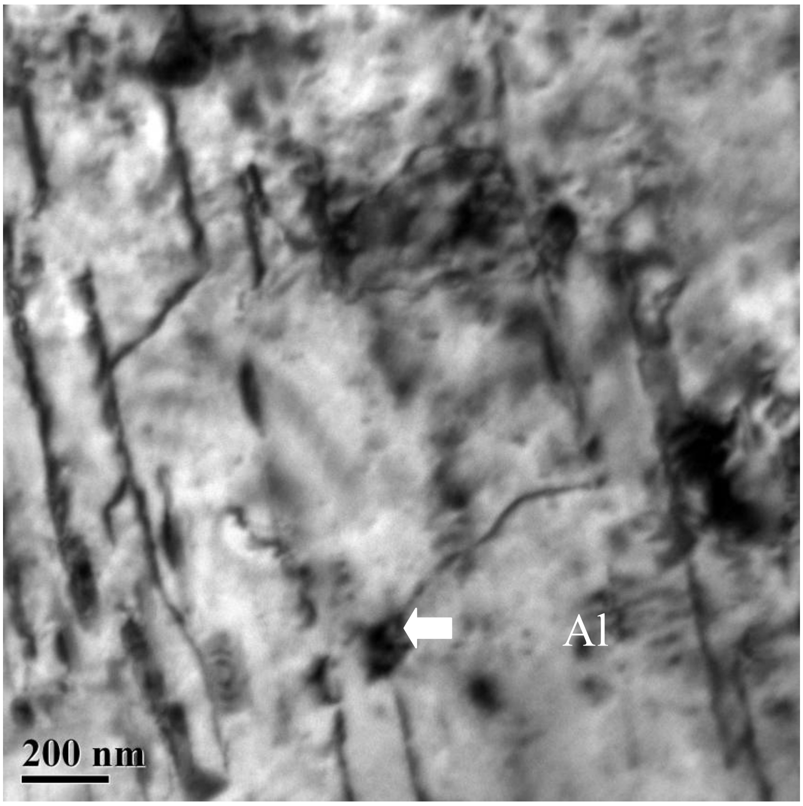

Fig. 4-19. Fatigue deformation structure in the SB welds.

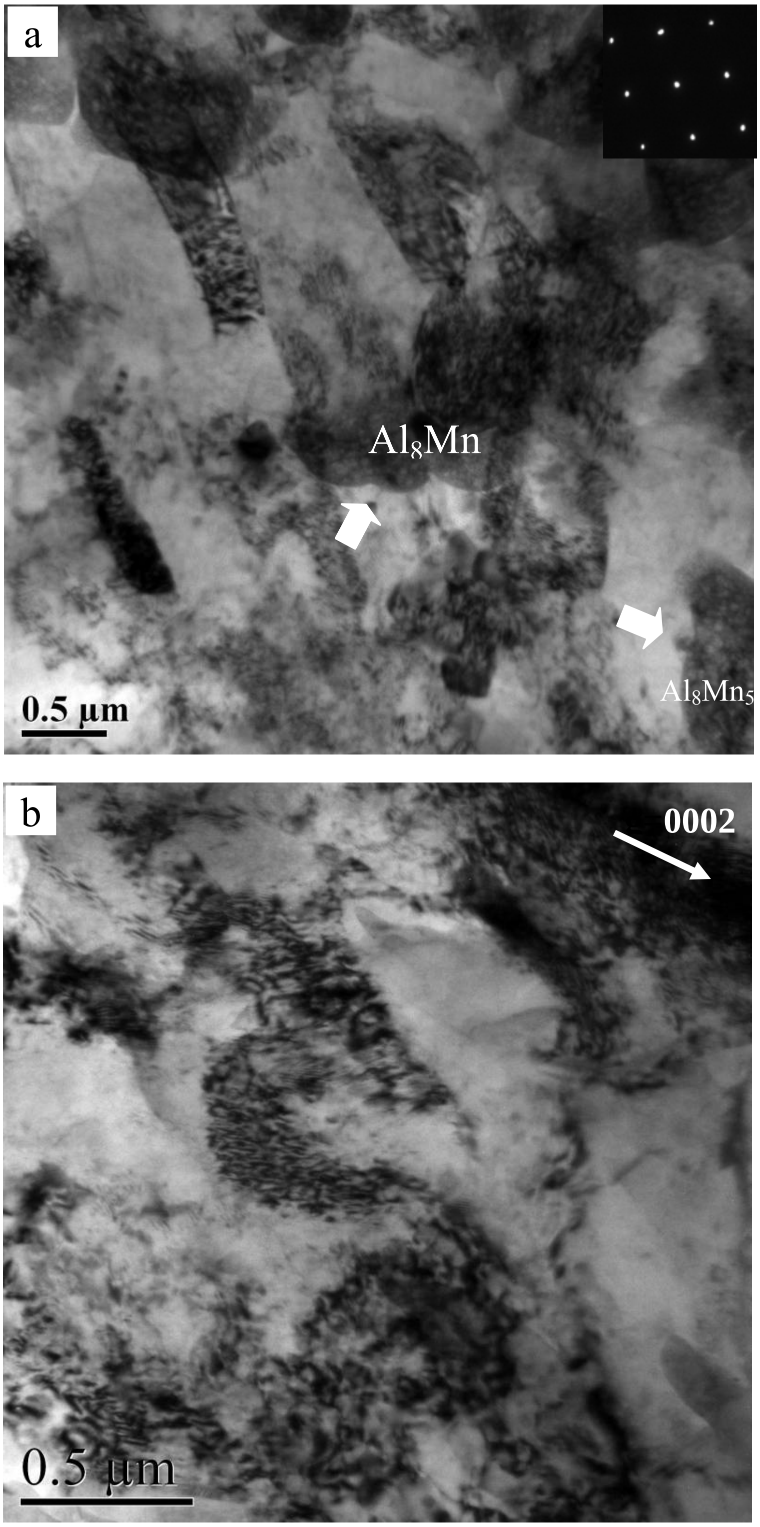

Fig. 4-20. Fatigue deformation structures in the SA welds at different load ranges: (*a*) ΔP=2.92 kN, N_f=1864 cycles, incident beam // $[01\bar{1}1]$ and (*b*) ΔP=3.65 kN, N_f=422 cycles, incident beam // $[01\bar{1}0]$.

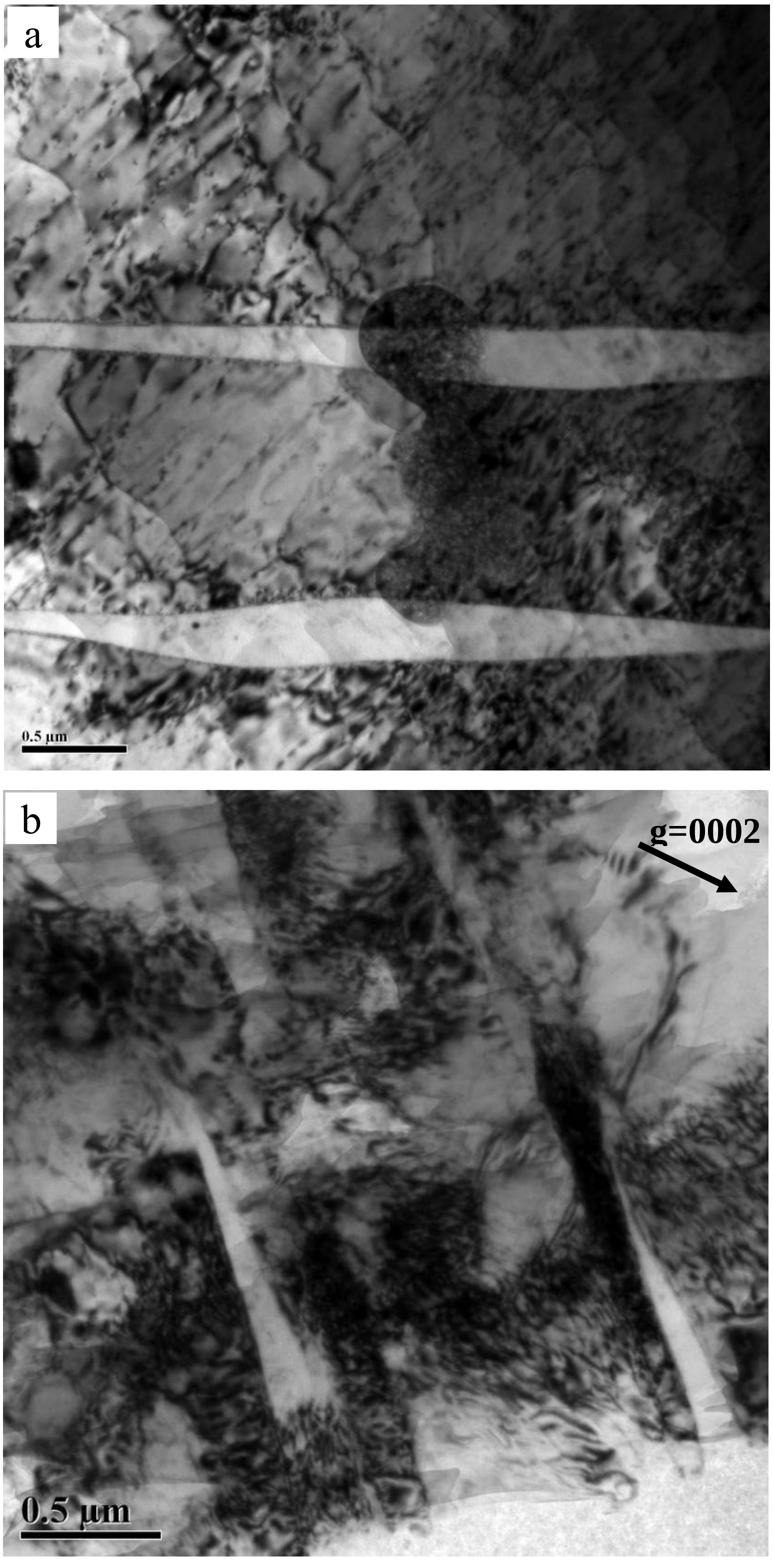

Fig. 4-21. Twinning in the fatigued SB and SA samples, incident beam // $[01\bar{1}0]$: (*a*) SB and (*b*) SA.

4.3. Discussion

4.3.1. Mn-Al Particles in AZ31 Alloys

Based on the theoretical calculations and experimental examinations, Laser *et al.* [50,52] suggested that some Al-Mn particles in the form of Al_8Mn_5 could be present on the dendritic boundaries and in the matrix in as-cast AZ31 alloy.

Al_8Mn_5 particles were observed to be present in AZ31 alloys in the as-received and welded conditions via SEM and TEM in this work. The welding process did not have a big effect on existence of Al_8Mn_5 particles. This implies that these particles were formed in the period of the AZ31 sheet making process. In other words, the details of the Mg alloy manufacturing process play a primary role in determining the size and distribution of residual Al_8Mn_5 products. The microstructure of AZ31 alloy welds, therefore, will be influenced by the sheet metal manufacturing process.

According to the heat input during RSW of AZ31, the temperature of the welding zone can reach 650°C to 770°C [28]. This implies that spontaneous melting of second-phase Al_8Mn_5 particles is precluded since this intermetallic has a melting temperature of 1048 ~1191°C [47], which is much higher than the highest predicted temperature of the fusion zones. Therefore, these preexisting Al_8Mn_5 particles in AZ31 alloys sheets will remain solid and can act as inoculants to promote the nucleation of new grains in the fusion zone.

4.3.2. Effect of Second-phase Particles on Columnar-to-Equiaxed Transition

Different microstructures were observed across the RSW welds of AZ31 SA and SB alloys, which have a similar chemical composition but different sizes of second-phase particles. It is usually believed that solification morphology in any welds of given alloys is related to the ratio of *G*/*R* [30,33,35,37]. During RSW, weld pool solidification always starts from the parent metal partially molten zone with a minimum degree of undercooling since the solidification phase has the same crystalline structure with the BM. This leads to the well-known epitaxial growth without requiring any nucleation event. The columnar dendritic grains which have their easy growth direction lining up favorably with the direction of maximum temperature gradient tend to grow faster and crowd out other columnar grains. A columnar dendritic structure is produced as shown in the SB alloy (Figs. 4-3(b) and 4-4(b)).

If the size of second-phase particles in front of the interface is significantly less than the critical embryo radius, r^*, few new grains will nucleate in the molten pool under typical welding conditions. If the size is above the r^*, the nucleation of new grains is possible. But, when the size is not big enough, then any growing equiaxed grains will be trapped by the progressing columnar grains and the grown macrostructure will retain a columnar dendritic morphology (Fig. 4-4(b)). However, new grains will nucleate and grow if the second-phase particles are big enough to become nuclei in the areas near the fusion boundary. These coarse second-phase particles block off the epitaxial columnar grains. Consequently, the main growth competition can switch from being among epitaxial columnar grains themselves to between epitaxial columnar grains and new grains formed in the fusion zone. Columnar dendritic grain growth will be restricted and equiaxed grains will partially replace the columnar ones, as displayed in the AZ31 SA alloy welds (Figs. 4-3(a) and 4-4(a)). Meanwhile, the grains could be refined in the central areas of AZ31-SA weld as the nucleation efficiency of the coarse nuclei increased (Fig. 4-5(a)).

When nucleant particles are present in the molten pool, thermal and constitutional undercooling driven heterogeneous nucleation is believed to play an important role in promoting columnar-to-equiaxed transition. The heterogeneous nucleation would occur ahead of the columnar front once the undercooling suffices to induce heterogeneous nucleation, depending upon the inoculant sizes. The dependence of nucleation efficiency on the size and surface properties of the foreign nucleating particles was investigated by Fletcher [108]. It has been well accepted that the size effect of a nucleant particle is related to the critical embryo radius, r^*, which is a function of the undercooling. It was recently demonstrated that the bigger the nucleant particle, the more effective they are, when the radius of the nucleant particle, R, is smaller than $5r^*$. However, little further influence of the nucleant particle size on heterogeneous nucleation will be displayed, when $R > 5r^*$ [73].

According to Ref. [132], the r^* for nucleation of Mg could be estimated with the following equation:

$$r^* = -\frac{2\gamma_{SL} T_m}{L_V \Delta T} \tag{4-2}$$

where melting point of magnesium, T_m=923 K, the solid/liquid interfacial free energy γ_{SL}=0.115 Jm^{-2}, and the latent heat of fusion per unit volume of solid Mg, L_V=5.989×10^{8} Jm^{-3}. ΔT is the undercooling required to overcome the free-growth barrier for the effective initiation of a grain on particles. Therefore, the critical embryo radius in α-Mg can be estimated by the following equation [167]:

$$r^* = 0.354/\Delta T \tag{4-3}$$

The critical embryo radius r^* is typically of the order of magnitude of 10^{-1} μm in many cases [167]. This means that the size effect will be observed by using substrate particles of less than

1 μm in diameter ($2R<10r^*$). To enhance heterogeneous nucleation, the substrate radius needs to be at least five times that critical embryo radius. In other words, the coarser the Al_8Mn_5 particles, the more efficient the nucleation is and the more grain refining of the weld, when the diameter of nucleant is up to 1 μm. No extra promotion of nucleation would be observed when the diameter of nucleant is larger than 1 μm. Therefore, the Al_8Mn_5 particles with 4 to 10 μm in the SA alloy welds can be expected to have higher efficiency of nucleation than those with 0.09 to 0.2 μm in the SB alloy welds.

4.3.3. Columnar-to-Equiaxed Transition Induced by Adding Mn Particles into the SB Alloy

In order to confirm the effects of second-phase particles on the microstructure formed in AZ31 Mg alloy, coarse Mn particles, ~10μm in length, were intentionally added into the fusion zone of some AZ31 SB welds, which did not contain coarse Al_8Mn_5 particles in the as-received condition. Welds were doped with Mn by placing powders on the surface of the sheets in the welding areas before welding. All welding parameters were kept the same as the previous tests on the as-received SA and SB alloys sheets. Typical optical microstructure across the weld of the SB alloy specimen with added Mn particles is shown in Fig. 4-22. This microstructure is similar to that formed in the SA alloy, which contains the coarse Al_8Mn_5 particles. This result clearly demonstrated that the introduced Mn particles dramatically restricted the growth of columnar dendritic structure within an area of 420μm in width and promoted the columnar-to-equiaxed transition in the AZ31 SB alloy welds. Furthermore, these microstructures formed in the SB alloy welds with added Mn particles were analysed via SEM and EDS. Some equiaxed dendritic grains were observed to nucleate on the surface of the added Mn particles, as shown

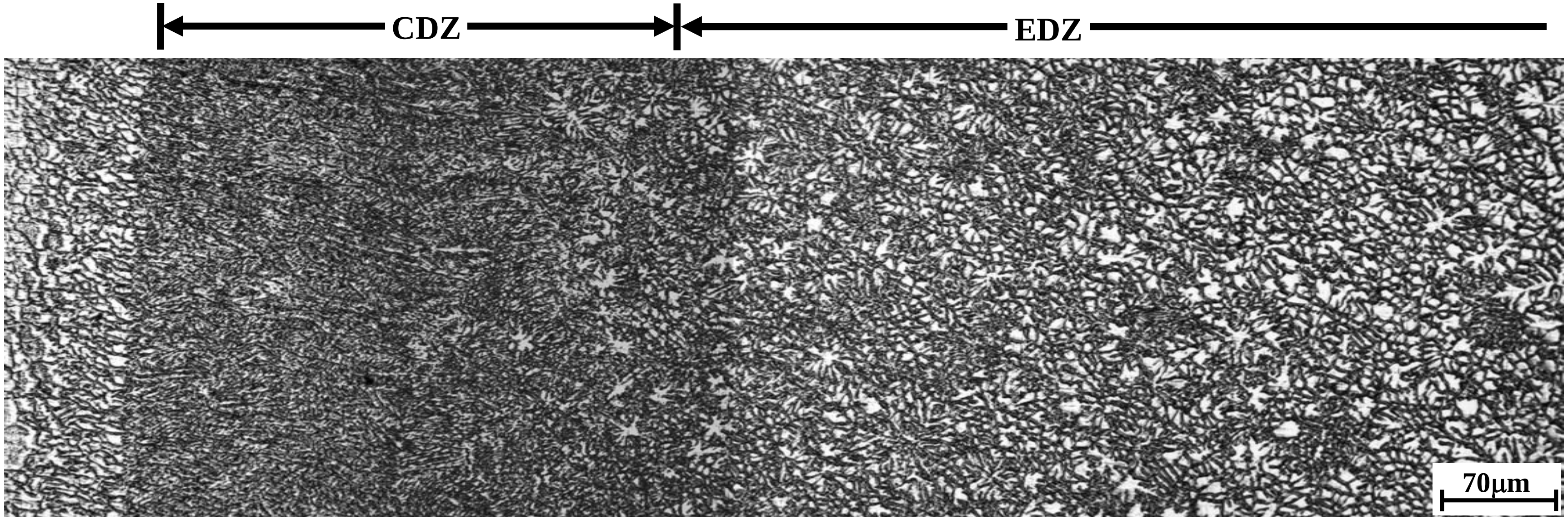

Fig. 4-22. Microstructure variation across RSW AZ31 SB alloy welds with addition of Mn particles.

in Fig. 4-23(a). This inoculant was determined by EDS to be Mn particles, as shown in Fig. 4-23(b). This result confirms that the reduction of the columnar dendritic structure in the AZ31 alloy SA weld can be attributed to the pre-existence of coarse Al-Mn intermetallic second-phase particles in the AZ31 Mg alloy.

4.3.4. Other Factors Affecting Columnar-to-Equiaxed Transition

The columnar-to-equiaxed transition in AZ31 Mg alloy welds can be affected by several other factors such as welding heat input, cooling rate, and chemical compositions of base metals, besides the second phase particles of relatively high melting temperature. It is well known that the higher the cooling rate, the shorter the solidification time of welds, the finer the dendritic structure becomes [29]. As the welding heat input increases, the temperature gradient (G) of the melt pool is reduced. This effect results in limiting constitutional supercooling and promoting equiaxed grains, which in turn block off the growth of columnar grains [37]. In this work and the examined welding conditions, the nugget size of two AZ31 Mg alloys is almost the same (Figs. 4-2(a) and (b)). Therefore, it is believed that the welding heat input and cooling rate should be similar for the SA and SB alloy welds. However, different from the case of casting, the cooling rate is much faster during resistance spot welding. That leads to a high thermal undercooling of welds. Since the melting temperature of AZ31 Mg alloys is approximately 640°C to 670°C during welding in the present welding condition and the melting temperature of the ternary eutectic Mg-Al-Zn is about 430°C [47], the thermal supercooling temperature of AZ31 Mg alloy welds could be as high as ΔT = 210~240°C.

Thermal supercooling is believed to play a significant role in promoting the columnar-to-equiaxed transition in AZ31 Mg alloy resistance spot welds. However, this thermal

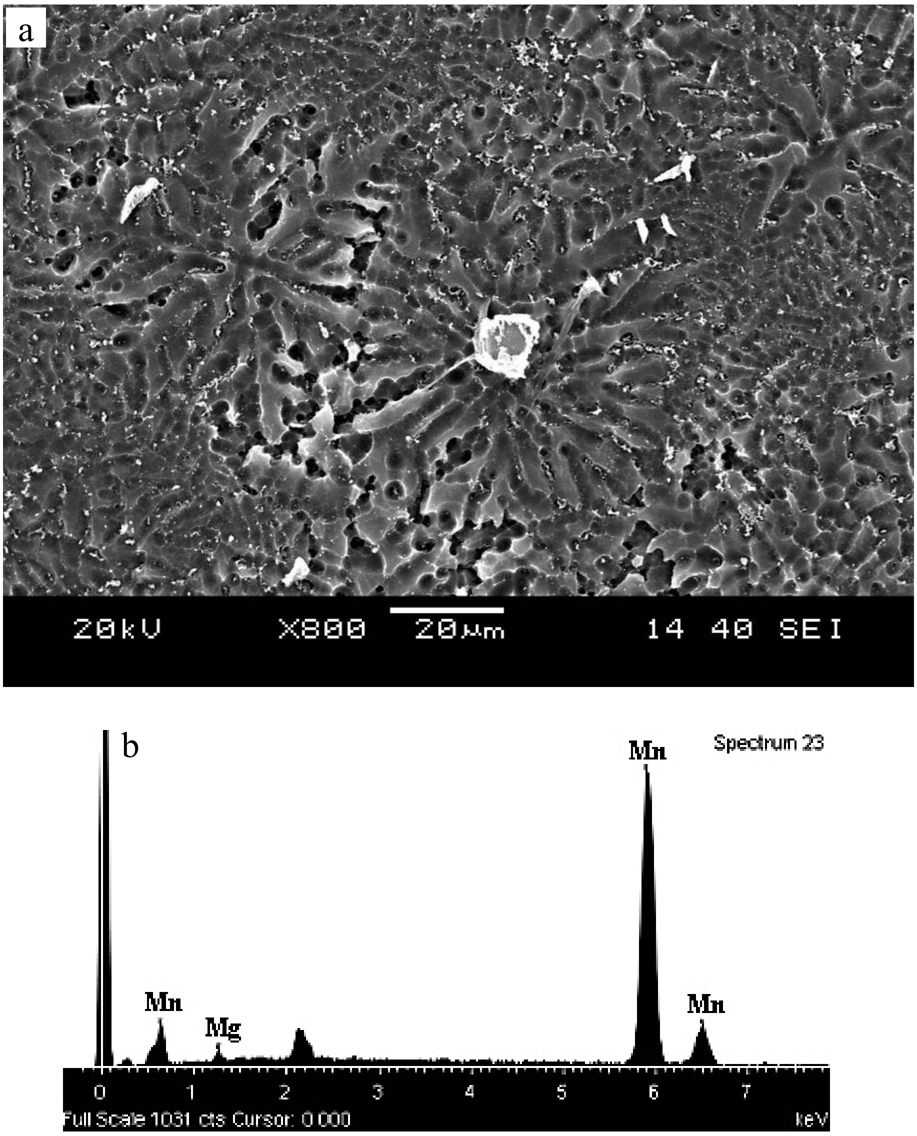

Fig. 4-23. Illustration of an added Mn particle as a nucleus of equiaxed dendritic grain: (*a*) SEM image and (*b*) EDS.

supercooling should not lead to an obvious difference of microstructure between the SA and SB alloys, since they have the similar heat input at the same welding condition. Therefore, it is believed that constitutional supercooling and second-phase particles play a predominant role in restricting the growth of columnar dendritic structure in the SA alloy, and lead to a different microstructure between the SA and SB alloy welds. The details of effects of thermal supercooling on microstructure of AZ31 Mg alloy welds under different welding conditions were reported in the paper [151].

For the effect of chemical compositions of base metals, solute atom zinc (Zn) may have an influence on the width of columnar dendritic zone by promoting the formation of nuclei for equiaxed dendritic structure [75], since Zn concentration in the SA alloy (1.09%) is higher than that in the SB alloy (0.8%). The equilibrium solid solubility of Zn in Mg substantially decreases with temperature. Zn is next to aluminium in effectiveness as an alloying ingredient to strengthen AZ 31 Mg alloy. The primary effect of the added Zn is believed to be promotion of the age hardening effect of Mg-Al precipitates and improvement of the creep properties of AZ31 alloys [163,168]. On the other hand, Zn was observed to form fine precipitates of $MgZn_2$ compound of around 0.04 μm during double aging in ZM61 and ZMA611 Mg alloys [59,61]. Therefore, the higher concentration of Zn in the SA alloy could form $MgZn_2$ with a size of 0.04 μm, which is similar in size to the sub-micron Al_8Mn_5 existing in the both SA and SB alloys. Therefore, the difference of Zn concentration should not have a big contribution to the microstructure refinement of AZ31 Mg alloy welds, compared to that of the much larger Al_8Mn_5 particles present only in the SA alloy.

4.3.5. Effect of Grain Refinement on Fatigue Behaviour

In a spot-welded joint, a natural notch forms at the junction of nugget between two welded sheets [162,163]. The high shear and normal stress concentrations are produced at the edge of the weld spot under tension-shear loading. Finite element simulation showed that the normal tensile stress concentration could reach as high as more than five times the average stress under tensile–shear loading [169]. This high normal tensile stress concentration could lead to initiation of fatigue cracks on the fusion boundary at the edge of weld spots, and to propagation through the nugget, when the cyclic loading range is high (Fig. 4-14(a)). As a result, the interfacial fracture is exhibited at high cyclic loading ranges. The strength of nugget is high enough to resist fatigue crack propagation through the nugget at the low cyclic loading ranges. Consequently, failure through thickness is displayed (Fig. 4-14(b)). A similar fracture mode was observed in the fatigued spot-welded DP600 steel [170].

The fatigue life of AZ31 Mg alloy welds in SB with a coarser dendrite structure was lower than that of SA with a finer dendrite structure, when interfacial failure took place across the fusion zone. The corresponding fatigue dislocation configurations changed from parallel dislocation lines and parallelogram dislocation cells in SB to elongated dislocation cells in SA. The activated slip systems changed from {0002} single basal slip alone in the SB welds to basal slip together with pyramidal multiple slips in the SA welds. The fatigue life improvement could be rationalized in terms of the transition of plastic deformation mode in these AZ31 Mg alloy welds.

According to the reported data, the critical resolved shear stress (CRSS) of a basal slip system is approximately 1/100 those of non-basal slip systems on prismatic and pyramidal planes in single crystal Mg at room temperature [171,172]. Therefore, plastic deformation in polycrystalline Mg alloys has been thought to occur almost entirely on the (0002) basal plane. However, the (0002) basal slip provides only two independent slip systems, far fewer than the necessary five independent slip systems required to fulfill the von Mises criterion for homogeneous deformation of polycrystalline materials [154,173]. Consequently, plastic heterogeneity is very strong in hcp Mg alloys and may give rise to large plastic compatibility stresses between adjacent dendrite boundaries [156]. The strong slip incompatibilities in and near interdendritic regions of the Mg alloys would lead to a rapid increase of local stress concentration to a sufficiently high level to activate twinning or other possible slip systems depending on the orientation of the surrounding grains and the level of localized stress concentration.

Dislocation slip in coarse-grained SB welds was expected to be restricted to basal slip, since the welds have a well-developed columnar dendritic structure, as well as coarse equiaxed dendrites of about 85 μm diameter in which could provide a long mean free path for the mobile dislocations. Therefore, parallel dislocation lines were formed in the fatigued SB welds (Fig. 4-18(a)). As the applied cyclic load range increased, the slipping dislocations piled up and accumulated at obstacles on the basal planes, local stress concentrations would be produced to activate cross-slip to non-basal planes. As a result, cross-slipping of ***a*** dislocation to non-basal planes was significantly activated resulting in the formation of parallelogram dislocation cells at high cyclic load ranges (Fig. 4-18(b)).

Localized stress concentration is proportional to the grain size at a given applied stress [173]. It is much higher in coarse-grained samples than that in fine-grained samples, since the former would have a longer mean free path of the mobile dislocations than the latter, leading to pile-up of more dislocations against obstacles as sessile dislocations. This would result in a magnified internal stress at the head of the pile-up which would cause sources in certain secondary systems to operate [173]. On the other hand, deformation twinning becomes more active in coarse grains during plastic deformation, because the critical shear stress for twinning in fine-grained specimens was calculated to be higher than that in coarse-grained ones [174]. Therefore, the localized stress concentrations in coarse grains could easily reach the critical shear stress for twinning at a given applied stress. Consequently, deformation twinning was more easily activated in the coarse-grained SB welds due to sufficient stress concentration and the lower critical shear stress of twinning. In comparison, the level of local stress concentration would decrease and the critical shear stress for twinning increase, leading to less extensive twinning in the SA welds with refined grains. However, the number of grains oriented for favorable non-basal slip is expected to increase in the fine-grained SA welds. Under such a circumstance the pyramidal multiple slips and twinning could be simultaneously activated in the SA welds. Similar results have been reported in [156,160]. The activation of basal and pyramidal slips together with twinning can provide five independent slip systems to satisfy the von Mises criterion for sustained plastic deformation of polycrystals [154]. As a result, dislocation cells became a predominant dislocation configuration in the fatigue tested fine-grained SA welds (Fig. 4-20).

Micron-sized Al_8Mn_5 particles (4-10 μm in diameter) were only observed in the SA welds. Submicron-sized Al_8Mn_5 second-phase particles (0.09-0.4 μm in diameter) and nano $Mg_{17}(Al, Zn)_{12}$ precipitates (0.1 μm in diameter) were detected in both SA and SB welds. The intermetallic compounds are harder than the matrix of Mg. The presence of harder second-phase particles in the fusion zone played an important role of dispersion strengthening by the Orowan dislocation bypass strengthening mechanism in the SA welds with the large-size of particles [166]. The interaction between dislocations and second-phase particles leads to an increase of the resistance to dislocation slip [173]. A transition from planar single slip to multiple slips could be induced, and the fatigue lifetime of the alloy could be enhanced. However, further work is needed to understand in detail the effect of second-phase particles on plastic deformation behaviour and their relative contributions to fatigue life improvement of Mg alloy welds.

Better fatigue properties have generally been related to a higher degree of dispersion of slip systems for hcp metals [154,173,175]. Therefore, longer fatigue life can be expected in the SA welds than that in the SB welds due to the increase in the number and dispersibility of slip systems in the fusion zone during cyclic deformation under conditions where interfacial fracture occurs at a higher level of cyclic load range (i.e., in the LCF range of about $N_f<3\times10^3$ cycles), as shown in Fig. 4-15.

The currently observed effect of the size of microstructural features on fatigue life can also be corroborated from a perspective of fatigue crack growth resistance in cast Mg alloys as reported in [176]. *In-situ* observations of low-cycle fatigue damage by Gall *et al.* [176] showed that fatigue cracks nucleated and grew along persistent slip bands (PSBs) in the cast AM60B Mg alloy. The strong slip incompatibilities between adjacent dendrite cells created high mismatch stresses in and near interdendritic regions and facilitated rapid PSB and crack formation. PSB formation and subsequent cracking were often favoured in larger dendrite cells because of the relatively larger dislocation pile-up length and, thus, higher local stresses. Cracks that formed at PSBs nearly instantaneously spanned the entire length of the slip band, rather than slowly propagating along the slip band. Consequently, the cast AM60 Mg alloy with the finer dendrite size displayed the higher resistance to fatigue crack growth and an improved fatigue life [176]. AM30 Mg alloy with smaller grains was also observed to exhibit a greater fatigue resistance compared to specimens with larger grains [177]. Therefore, the SA welds containing finer dendrite cells could be expected to have a stronger resistance to fatigue crack propagation and a longer fatigue life than the SB welds with coarser dendrite cells.

4.4. Summary

1. Typical weld microstructure of AZ31 Mg alloys consists of four distinct regions, i.e. base metal (BM), heat-affected zone (HAZ), columnar dendritic zone (CDZ), and equiaxed dendritic zone (EDZ) in the fusion zone. The primary microstructural difference between AZ31 SA and SB alloy welds was found to be the size of the columnar dendritic zone. Columnar dendritic grains were well-developed in the SB alloy welds, while they were restricted within a narrow region near the fusion boundary by an earlier transition from columnar to equiaxed structure in the SA alloy welds.
2. Even though the two AZ31 Mg alloys have similar chemical compositions, different manufacturing processes led to the formation of different sizes of second-phase particles in the SA and SB alloys in the as-received condition. Coarse Al_8Mn_5 particles of 4-10 μm in length were only formed in the SA alloys. Submicron Al_8Mn_5 second-phase particles of 0.09-0.4 μm in length were observed to be present in both SA and SB alloys. All of these Al-Mn intermetallic particles were pre-existing from the sheet manufacturing process and were not apparently changed significantly by the transient melting during weld nugget formation.
3. The pre-existing Al_8Mn_5 intermetallic compounds particles could act as nuclei of α-Mg equiaxed dendritic grains during the solidification of the AZ31 Mg alloys in RSW. The refined microstructure in the vicinity of the fusion boundary in the SA alloy could be attributed to the preexisting coarse second phase particles of Al_8Mn_5 which play the role of inoculants causing heterogeneous nucleation on their surface during weld nugget solidification. The coarser the particles, the more efficient the nucleation of α-Mg was found to be.

4. Columnar dendritic grains can be restrained and equiaxed grains can be promoted by adding some coarse Mn particles of ~10μm in length into the fusion zone of AZ31 SB alloy welds, which do not contain any coarse Al-Mn particles in the as-received condition.
5. AZ31 SA resistance spot welds with a refined fusion zone microstructure had a longer fatigue life than that of AZ31 SB welds with a coarse fusion zone microstructure, when interfacial failure across fusion zone occurred at a higher level of cyclic load range larger than 2.3kN.
6. Typical dislocation configurations in the fusion zone of the SA welds consisted of elongated dislocation cells. In comparison, elongated parallel dislocation lines and parallelogram dislocation cells were observed in the SB welds.
7. Deformation mode in the AZ31 welds evolved from {0002} single basal slip in the SB alloy welds to $1/3\langle 11\bar{2}3\rangle$ pyramidal combined with {0002} basal slips in the SA alloy welds.
8. Twinning was observed to serve as another important deformation mode in both SA and SB welds. However, more twins appeared to be present in the coarser-grained SB welds. This may be due to the strong slip incompatibilities causing a rapid increase of local stress concentration to a sufficiently high level to activate twinning in neighbouring dendrite cells which had the higher stress concentration and the lower critical shear stress for twinning.
9. Pyramidal multiple slips and twinning were simultaneously activated in the finer-grained SA welds probably due to the lower stress concentrations and the high critical shear stress for twinning. This led to an increase of the amount and dispersibility of slip systems in the SA welds, thus a longer fatigue life than that of the SB welds.

5. Microstructure Refinement Due to the Addition of Titanium Particles in AZ31 Magnesium Alloy Resistance Spot Welds

Resistance spot welding (RSW), which is a widely-used joining technique in the automotive industry, frequently results in the formation of well-developed columnar grains in the vicinity of fusion boundaries and coarse equiaxed dendritic grains in the central region of AZ31 Mg alloy welds [29,31,151,153]. Columnar and coarse dendritic structures in fusion zones can seriously compromise the mechanical properties of welds [28,31,178]. Fine grains are generally desirable to improve mechanical properties of welds. Therefore, it would be desirable to replace columnar grains with fine equiaxed ones to improve the weldments' mechanical properties.

In aluminum gas-tungsten arc (GTA) welds, Kerr and co-workers [33,178] and later Kou and Le [36,37] observed that Ti-rich particles acting as heterogeneous nucleation sites promoted CET. Lu *et al.* [180,181] observed that carbon inoculation significantly refined the microstructure of Mg–Al alloy castings [180,181]. The most commonly accepted theory of carbon inoculation is that carbon reacts with Al in the melt creating aluminum carbide (Al_4C_3) particles and α-Mg nucleates at the surface of the Al_4C_3 particles which promote grain refinement in the Mg–Al alloy system [180,181]. Furthermore, Kim *et al.* [182] proposed a theory of duplex nucleation, according to which, a polygonal Al_8Mn_5 first nucleates on the surface of Al_4C_3, and then α-Mg nucleates on the surface of Al_8Mn_5 in Mn-containing Mg–Al alloy systems. Nimityongskul *et al.* [183] provided direct experimental evidence of this duplex nucleation model in AM60B castings.

The effect of titanium (Ti) compound addition in the form of Al-3Ti-3B [109,184] and Al-10Ti [185] as a solute on the microstructure of aluminum [65,68,109,184] and Mg alloy castings [136,185] has been studied. It was demonstrated that Ti is the most effective solute element at reducing the grain size of Al alloys in terms of the growth restriction factor (GRF) [109]. Wang *et al.* [185] studied the effects of Ti addition as a solute in the form of the Al-10Ti in a low-frequency electromagnetic casting process on the grain refinement of AZ31 Mg alloy. The grain refinement was related to the potency of the nucleant and the degree and rate of development of constitutional supercooling generated by the Ti solute elemental rejection during growth of previously nucleated grains [185].

To authors' knowledge, little information is available on the effect of pure Ti particles as an inoculant on the microstructure of Mg alloy welds. The pre-existence of the coarse Al_8Mn_5 intermetallic phases as an inoculant was observed to promote the columnar-equiaxed transition (CET) and microstructure refinement of AZ31 Mg alloy welds. Consequently, mechanical properties of welds were enhanced. The objective is to study the effect of extraneous Ti addition as an inoculant on the microstructure refinement and mechanical property improvement of AZ31 alloy welds which did not contain coarse Al_8Mn_5 second phase particles.

5.1. Experimental Procedure

5.1.1. Welding with an Addition of Inoculant

The material was commercial grade hot rolled sheets of AZ31 SB Mg alloys. Ti powder with a purity of 99.98% and a size of ~400mesh were doped inside the fusion zone positioned by a template with a nugget-size of hole at the designed fusion zone on the interior surface of sheets before welding. Ti particles were irregularly shaped and polycrystalline. 8~10 mg of Ti powder was added to each nugget. The volume fraction of Ti inoculant in the fusion zone was further estimated using a polished planar cross-sectional specimen of nugget by the manual point count procedure according to standard ASTM E562-05. It was about 0.5 pct. The welding current was varied from 22kA to 32kA.

5.1.2. Temperature Measurement and TEM Foil Preparation with FIB Technique

The temperature as a function of time in the central area of fusion zones in AZ31 Mg alloy welds at different welding procedures was measured by means of K-type chromel-alumel thermocouples of 10 microns diameter, protected by ceramic tube and pre-placed in the central area of the fusion zone of selected welds through a tiny hole from the side of samples. Data acquisition was carried out with a computer and LabVIEW 8 software. Special magnetic shielding measures was taken to minimize the interference from welding current and the corresponding magnetic field by twining two ferritic rings in the circuit.

In order to analyze the orientation relationship between the added Ti particles and Mg matrix, transmission electron microscopy (TEM) foils containing second-phase particles were prepared using the Focused Ion Beam (FIB) technique with Zeiss NVision 40 Focused Ion Beam / Field Emission Scanning Electron Microscope according to an in-situ lift out method [186]. The milling process steps are shown in Fig. 5-1. A carbon coating was deposited prior to FIB milling to protect the particle surfaces and the interesting area upon exposure to the Ga+ beam, as indicated by an arrow in Fig. 5-1(a). A chunk of the material was removed from the bulk sample by using the FIB after removing material around it (Fig. 5-1(b)). To make the

TEM sample, trenches were milled from the sides of the particles, leaving only a TEM specimen from the center of the matrix. The chunk was then transferred to the grid by attaching the lamella to an Omniprobe TEM grid using FIB induced carbon deposition (Fig. 5-1(c)). Once attached to the grid, final thinning was performed on the lamella, initially at an acceleration voltage of 30 kV, and finally at 1 kV. Details of this procedure can be found in reference [182]. Fig. 5-1(d) shows how the second-phase particles containing TEM sample was excised from the AZ31 Mg alloy welds.

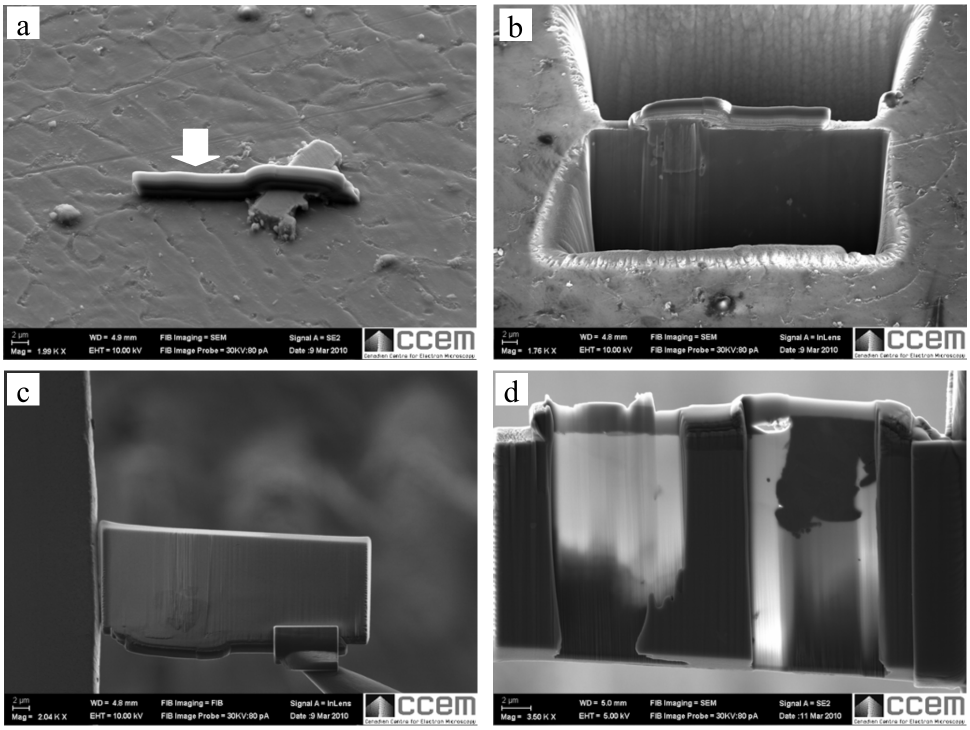

Fig. 5-1. TEM film cutting process with FIB.

5.2. Results

5.2.1. Optical Microstructure

A comparison of optical microstructures on the cross-sections of AZ31 alloy specimens welded without and with an addition of Ti powders is shown in Figs. 5-2(a) and (b) and 5-3(a) and (b). In both conditions, the microstructure could be distinguished with columnar dendritic zone (CDZ) and equiaxed dendritic zone (EDZ) in the fusion zone. The grain structures close to the fusion boundary of the welds were dominated by epitaxial growth. The structure in the weld without Ti addition primarily consisted of well-developed columnar grains, perpendicular to the fusion boundary in a zone with a width of 580 μm.

This region is identified as columnar dendritic zone (CDZ) in Figs. 5-2(a) and 5-3(a). In contrast, the CDZ was significantly suppressed to within an area of 320 μm in width in the welds with the addition of Ti powders, as shown in Fig. 5-2(b). Further examination showed that a fine-grained and more randomly oriented dendritic structure with short primary arms replaced the well-developed primary arms in the vicinity of the fusion boundaries of the welds with the addition of Ti powders, as indicated by arrows in Figs. 5-2(b) and 5-3(b). No obvious long columnar grains were observed in the AZ 31 specimens welded with the addition of Ti.

Towards the central area, the coarse flower-like equiaxed dendrites, defined as the equiaxed dendritic zone (EDZ), were formed in the welds both with and without the addition of Ti, as shown in Figs. 5-2(a), 5-2(b), 5-4(a) and 5-4(b). Further analysis showed that grain refinement was achieved in the central areas of AZ31 welds with the addition of Ti (Figs. 5-2(b) and 5-4(b)). The average diameter of the flower-like grains in the welds without the addition of Ti was approximately 65 μm (Fig. 5-4(a)), whereas it was only about 20 μm with the addition of Ti (Fig. 5-4(b)). Average primary dendrite arm spacings were measured to be approximately 40±10 μm in welds without the addition of Ti, but only 10± 3 μm when Ti was added.

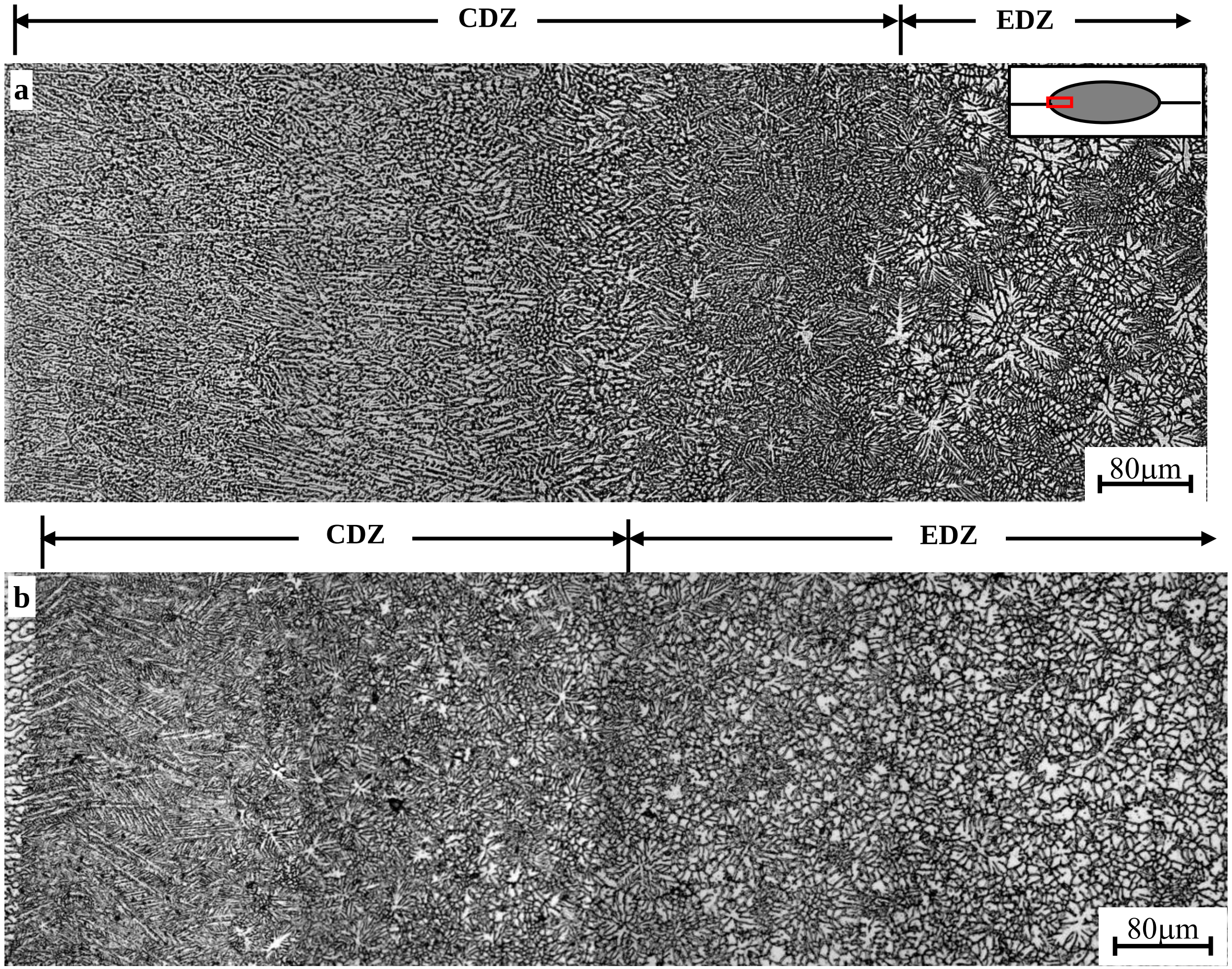

Fig. 5-2. A comparison of fusion zone microstructure in the AZ31 alloy welded: (*a*) without and (*b*) with an addition of Ti. CDZ — Columnar dendritic zone, EDZ — Equiaxed dendritic zone

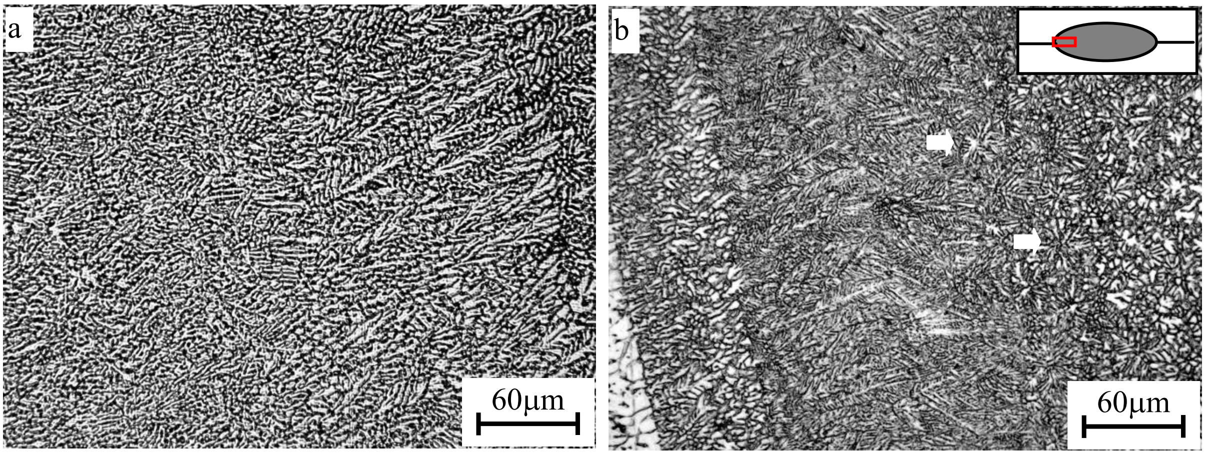

Fig. 5-3. Effect of Ti addition on the microstructure in the vicinity of the fusion boundary of AZ31 alloy welds: (*a*) without Ti addition and (*b*) with an addition of Ti.

5.2.2. Ti Particles in Fusion Zones of Welds

SEM examinations showed that Ti particles were successfully introduced into the fusion zones of these welds. Some second-phase particles were observed at the origin of equiaxed dendrites, as indicated by an arrow in Fig. 5-5. The other tiny particles were eutectic $Mg_{17}(Al, Zn)_{12}$ precipitates in the AZ31 Mg alloy. The energy dispersive spectroscopy (EDS) analysis showed that this large particle was Ti. Analysis of these second-phase particles using EDS line scanning also demonstrated that these particles were essentially pure Ti particles, as shown in Figure 5-6. The change of elemental concentration across the interface between particle and matrix was extremely abrupt. This implies that chemical reaction between the added Ti particles and alloying elements in the matrix did not happen.

Fig. 5-7 displays the X-ray diffraction (XRD) results of AZ31 welds without and with adding Ti powders. For comparison, the XRD curve of Ti powders was included, as well. Some Ti peaks were observed in the welds with added Ti powder, as indicated by down triangles in Fig. 5-7. No XRD peaks of Ti compounds were observed. These results implied that Ti particles were relatively stable in the fusion zone and did not react rapidly with the other alloying elements in the AZ31 Mg alloy during resistance spot welding.

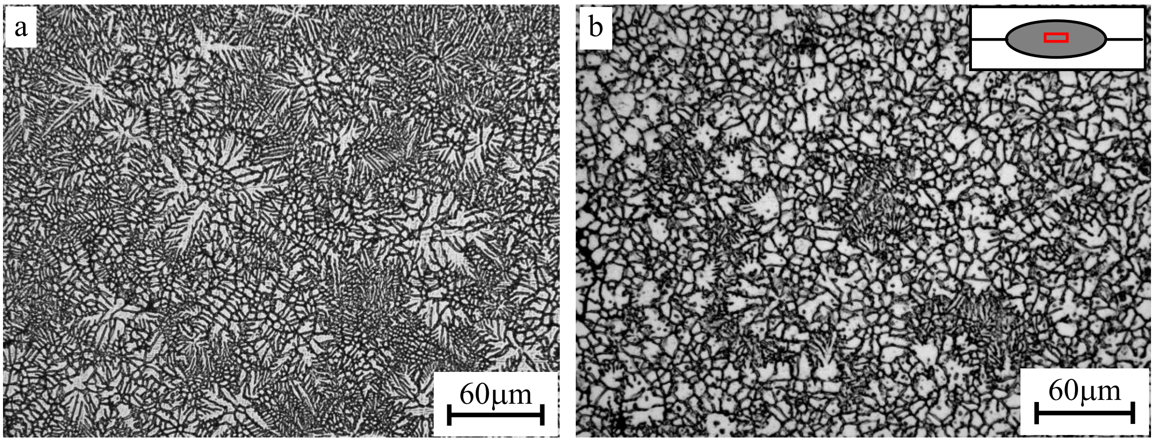

Fig. 5-4. Effect of Ti addition on the microstructure in the center of AZ31 alloy welds: (*a*) without Ti addition and (*b*) with an addition of Ti.

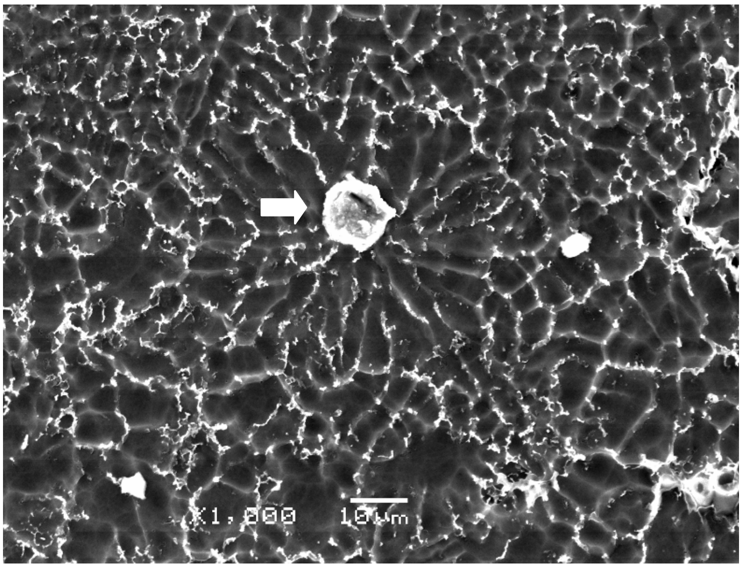

Fig. 5-5. Equiaxed dendritic grain nucleating on Ti particles in AZ31 welds.

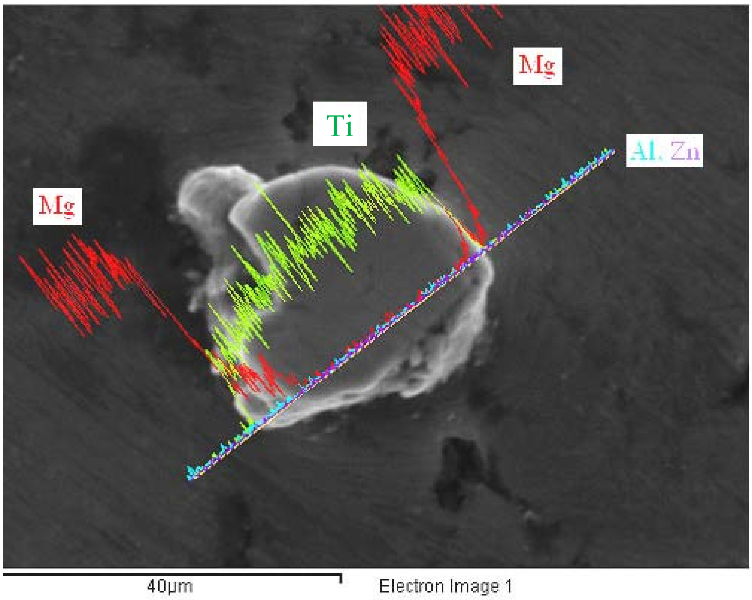

Fig. 5-6. Line-scan profile of chemical element distribution along the cross section of Ti particles in AZ31 welds.

The temperature as a function of time in the centeral area of the fusion zone in Mg alloy welded at 26 kA held for 8 cycles was shown in Fig. 5-8. The results revealed that the peak temperature which the fusion zone could reach, was about 1200°C. The solidification temperature is 600°C during cooling in the present welding condition, as indicated by an arrow in Fig. 5-8. Therefore, spontaneous melting of the added second-phase Ti particles would be unlikely during resistance spot welding because Ti has a melting temperature of 1668°C, which is much higher than what the welding zone could reach. Even though Ti-Mg and Al-Ti system peritectic reactions have low temperatures of 651°C and 665°C, respectively [51], the fraction of Ti which could dissolve into molten pool to become solute is limited according to Ti-Mg and Al-Ti phase diagrams [51]. As a result, Ti particles could exist in the molten pool in the as-received condition without dissolving or reacting with the other elements during welding.

5.2.3. TEM Analysis

The microstructure of the added Ti particles and their interfacial characterization with Mg matrix were analyzed with TEM. Figs. 5-9(a) and (b) demonstrate two typical added Ti particles. The surface and shape of the Ti particles were polyhedral (Fig. 5-9(a)). Multi-grain boundaries were clearly observed inside the added Ti particles, as indicated by arrows in Figs. 5-9(a) and (b). High density of dislocations were presented inside the Ti particles (Fig. 5-9(b)). The interfacial characterization between Ti inoculant and Mg matrix was carefully examined along different Ti grains, as shown in Fig. 5-10. The orientation relationships between the added Ti particles and Mg matrix in these grains were identified by combining information from several pairs of TEM bright-field images with the associated selected area electron diffraction patterns (SADPs) in Fig. 5-10. In this observed area of a TEM foil, Ti particle is polycrystal; in contrast, Mg matrix is single crystal. Therefore, the foil was tilted until the incident beam was parallel to the $[01\bar{1}0]$ zone axis of the Mg matrix, as shown in Fig. 5-10.

The interfacial microstructure and orientation relation between the Mg matrix and the different Ti grains along the Mg/Ti interface were sequentially determined by a series of SADP. The SADPs of Mg matrix, Ti particle, and the combination of Mg matrix and Ti particle were analysed at different sites, as indicated by 1 through 8 in Fig. 5-10(a). The SADP analysis results showed that a good orientation relation was only observed in site 3 indicated by an arrow in Fig. 5-10(a). The results of SADP analysis are shown in Figs. 5-10(b) to (e). Fig. 5-10(c) showed that the grain of Ti particle in site 3 was exactly located on $[1\bar{2}1\bar{3}]$ zone axis, when the Mg matrix was parallel to $[01\bar{1}0]$ zone axis. This result implies that the orientation relationship between the added Ti and the Mg matrix on the Ti/Mg interface is $[01\bar{1}0]_{Mg}$ //

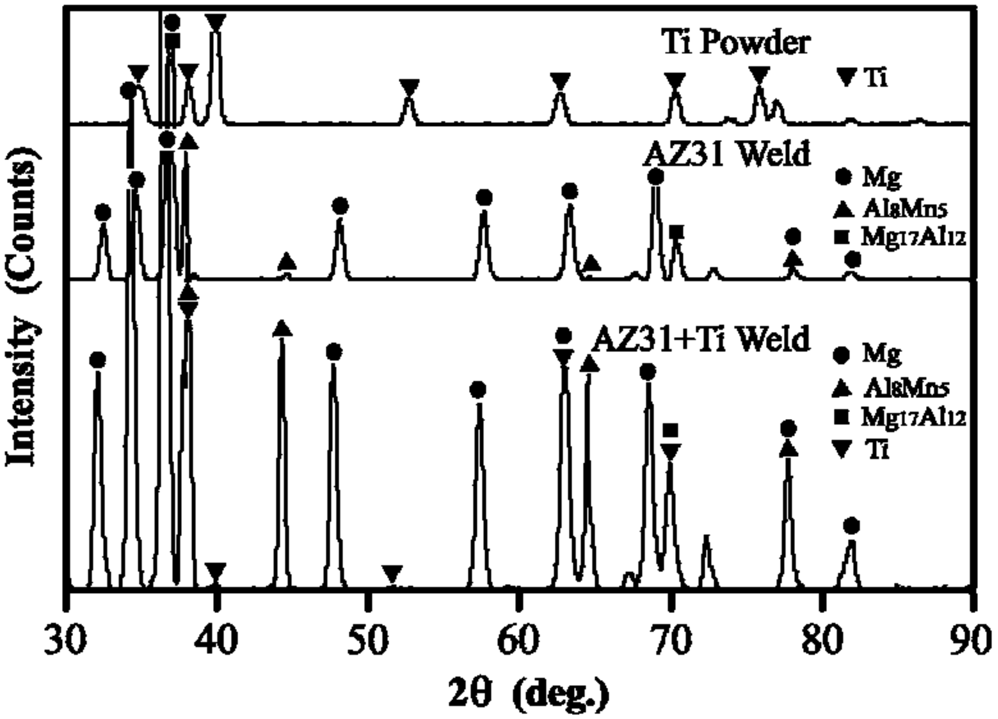

Fig. 5-7. A comparison of XRD curves of AZ31 alloy welds without and with adding Ti.

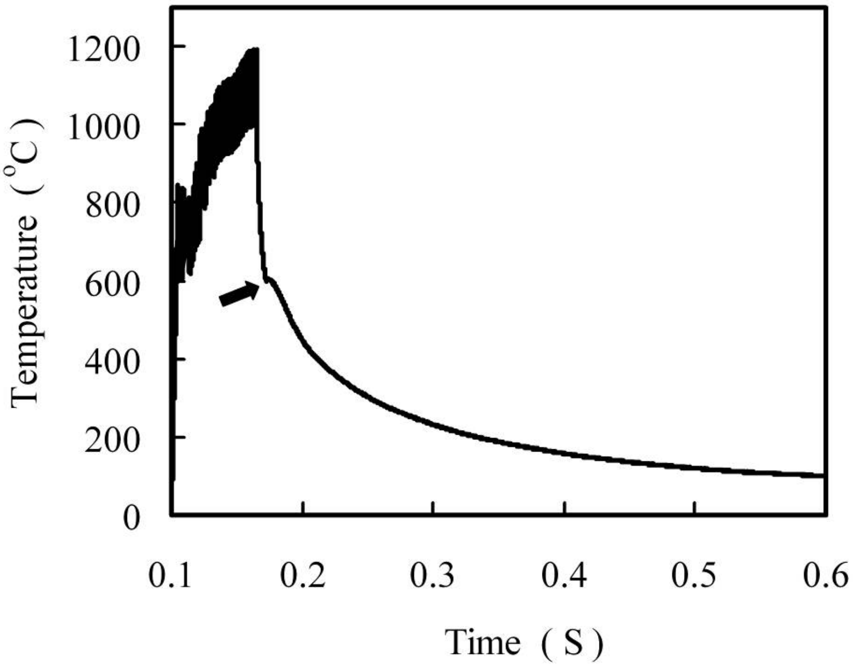

Fig. 5-8. Typical temperature variation curve as a function of time during welding of AZ31 alloy at 26kA in the central area of fusion zone.

$[1\bar{2}1\bar{3}]_{Ti}$. Furthermore, the diffraction spot of (0002) of Mg is superposed with that of $(10\bar{1}0)$ of Ti, as shown in Figs. 5-10(d) and (e). This indicates that the crystallographic plane relationship between the added Ti and Mg matrix in this site was determined to be: $(0002)_{Mg}//(10\bar{1}0)_{Ti}$.

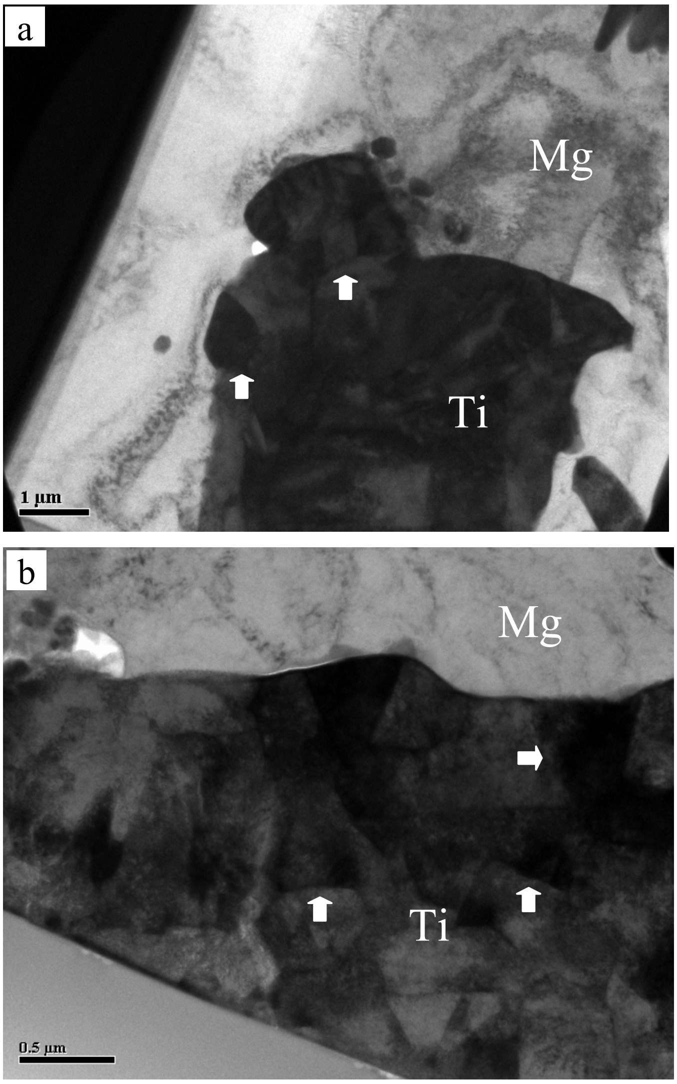

Fig. 5-9. The added Ti particles inside Mg matrix in the welds: (*a*) Polygonal Ti particle and (*b*) Grain boundaries inside Ti particle.

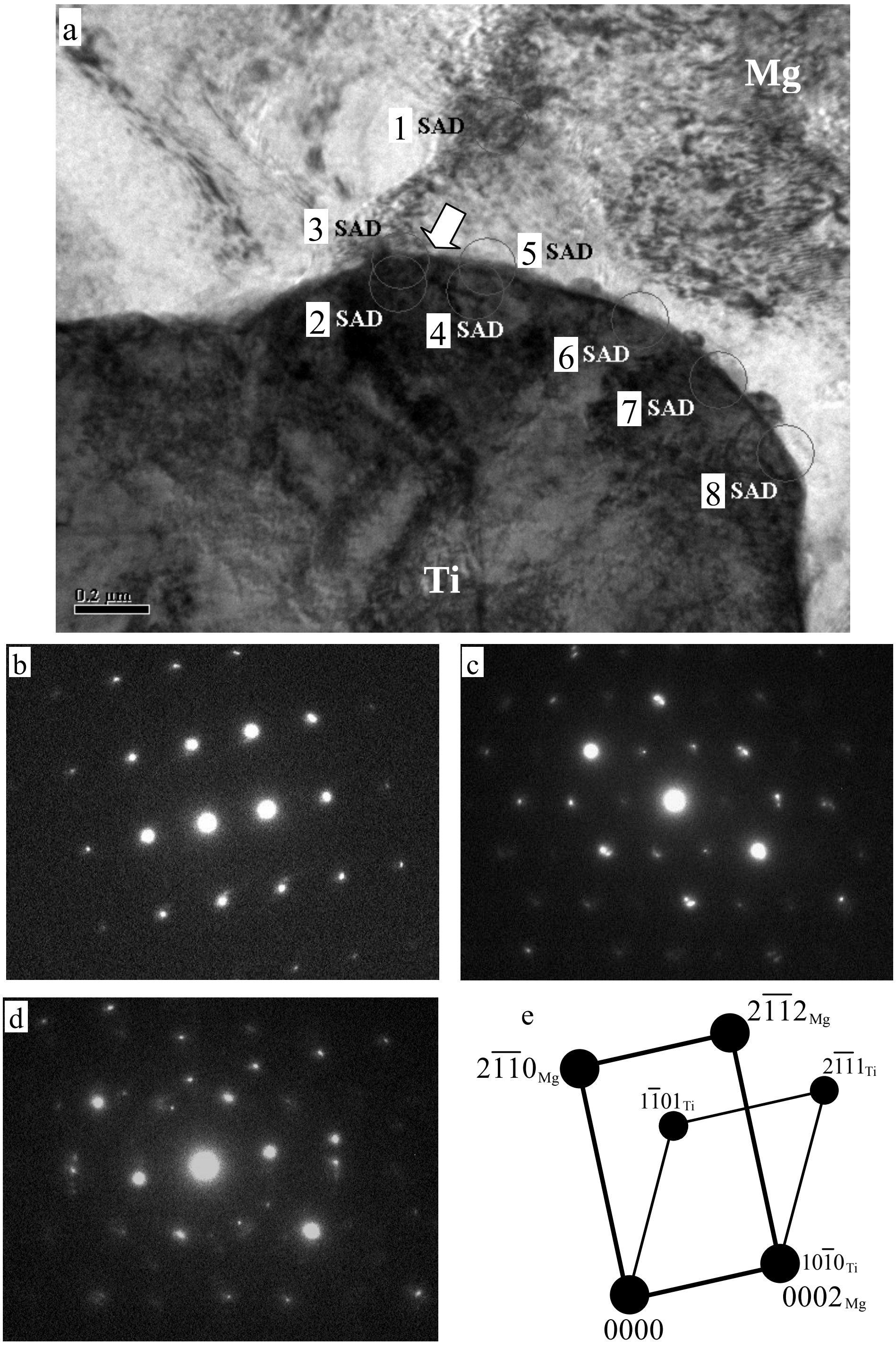

Fig. 5-10. The interface between the added Ti particle and Mg matrix: (*a*) TEM image, (*b*) selected-area diffraction pattern (SADP) of Mg matrix in point 1, incident beam || $[01\bar{1}0]_{Mg}$, (*c*) the corresponding SADP of the added Ti particles, incident beam || $[1\bar{2}1\bar{3}]_{Ti}$ in point 2, (*d*) SADP of the added Ti and Mg matrix in point 3, *i.e.* the interface between Ti and Mg, and (*e*) its schematic representation in $[01\bar{1}0]_{Mg}$ zone axis in point 3.

Distribution of elements across the interface between the added Ti particle and Mg matrix was further analyzed with STEM-EDS line scanning, as shown in Fig. 5-11. The results demonstrate that slight inter-diffusion of elements was limited within a layer of 30 nm. Chemical reaction between the added Ti particles and alloying elements in matrix essentially did not happen, since the element distribution sharply changed across the interface between the added Ti particle and Mg matrix.

5.2.4. Tensile-shear Properties of Welds

The tensile stress-strain data of as-received AZ31 Mg alloy sheets were measured and listed in Table 5-1. The yield strength ($\sigma_{0.2}$) of this alloy is 256 MPa, ultimate tensile strength (UTS) is 292MPa, and the elongation is 20%, which are slightly higher than those with a standard H24 temper designation.

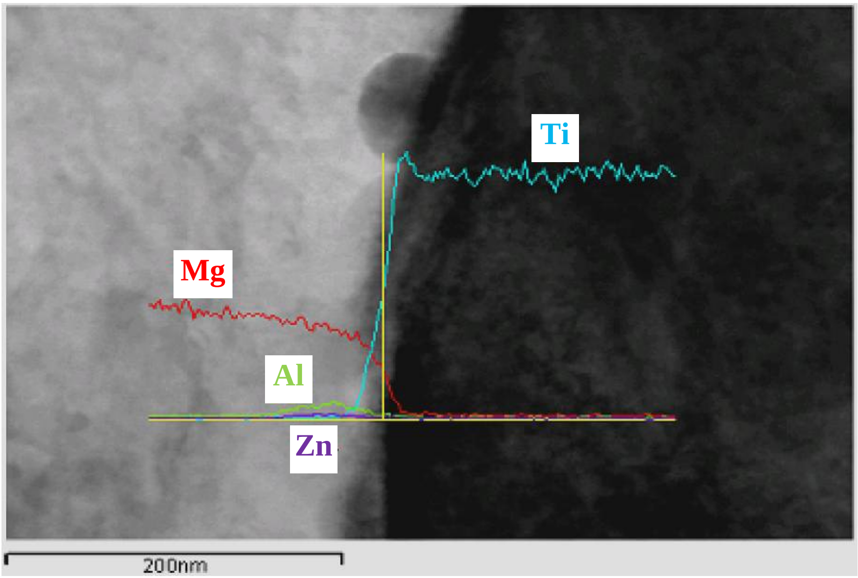

Fig. 5-11. Line-scan profile of chemical element distribution by STEM-EDS across the interface between the added Ti particles and Mg matrix.

Table 5-1. Tension Test Results of AZ31Mg Alloy in As-received Condition

Yield Stress, $\sigma_{0.2}$ (MPa)	Ultimate Tensile Strength, UTS (MPa)	Elongation, δ (%)
256	292	20

The tensile-shear testing of resistance spot welds was performed to examine the effect of Ti addition on the mechanical property aspects of weldability of this Mg alloy. Typical load versus displacement curves of AZ31 welds are illustrated in Fig. 5-12.

The tension-shear mechanical test results presented, each of which is an average of the data of four replicate samples, are summarized in Table 5-2. The ultimate tension-shear load of the alloy welded at 26 kA with an addition of Ti increased by 38 percent from 4076 N to 5619 N in comparison with the welds made without adding Ti. Meanwhile, the displacement rose by 28 percent from 1.09 to 1.40. Thus, both strength and ductility of AZ31 Mg alloy welds were

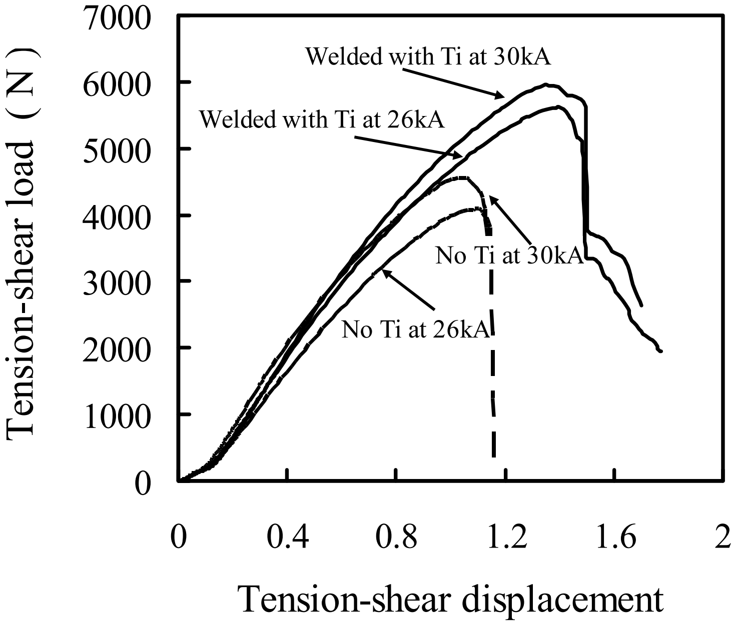

Fig. 5-12. Effect of Ti addition on tension-shear strength of AZ31 welds.

Table 5-2. Effect of Ti Addition on Tensile-shear Load and Displacement of AZ31 Welds

Welding Current (kA)	Welding Mode	Ultimate Load (N)	Ultimate Strength* (MPa)	Displacement (mm)
26	No Ti	4076	75	1.1
	Added Ti	5619	84	1.4
30	No Ti	4796	76	1.1
	Added Ti	5562	81	1.3

* Ultimate strength is the ultimate tension-shear load divided by the area of nugget.

increased by over 25 percent at a welding current of 26 kA. When the welding current increased to 30 kA, the ultimate tension-shear load of welds with adding Ti increased by 16 percent from 4796 N to 5562 N, and the displacement increased by 17 % from 1.12 to 1.31.

The added Ti powder could increase the contact resistance between the AZ31 Mg alloy sheets, and promote the nugget to grow under the same welding current. Our previous experimental results showed that the nugget size of resistance spot welds almost remained a constant in AZ 31 SB alloy, when the welding current was larger than 26kA [151]. Therefore, the tensile-shear properties of samples welded at high welding currents of 26kA and 30kA resulting in a much similar nugget geometry for resistance spot welds with and without adding Ti inoculants, were selected to compare. Furthermore, the ultimate tension-shear load was divided by the nugget size so as to eliminate the possible effect of nugget size. It was revealed from Table 5-2 that the ultimate tension-shear strength of the Mg alloy welds with adding Ti increased by 12% and 7% compared to those of the welds without adding Ti at 26kA and 30kA, respectively. However, the effect of heat-affected zone (HAZ) on tensile-shear properties of welds is significant when the nugget pullout failure occurs. Further work is needed on the HAZ of AZ31 Mg alloy resistance spot welds, which is beyond the scope of this paper.

5.3. Discussion

5.3.1. Grain Refinement due to Ti Addition in AZ31 Welds

Grain refinement was achieved in AZ31 Mg alloy welds by adding Ti powders into the fusion zones during resistance spot welding. The fine equiaxed dendritic structure formed in the AZ31 welds with an addition of Ti could be ascribed to the heterogeneous nucleation of α-Mg on parts of the surface of the Ti particles, since these particles were observed at the origin of equiaxed dendrites of the matrix as an inoculant by scanning electron microscopy (Fig. 5-5(a)). Moreover, EDS analysis revealed that the distribution of elements across the interface between Ti particle and Mg matrix showed no transition region of element distribution suggestive of rapid intermetallic formation (Figs. 5-6 and 5-11). In addition, the experimental measurement of temperature also showed that the peak temperature that the fusion zone could reach was well below the melting point of Ti metal (Fig. 5-8). Therefore, these added Ti particles could be expected to survive and become inoculants to promote nucleation of new grains in the fusion zone of Mg alloy welds, and this heterogeneous nucleation evidently promotes the transition of microstructure from columnar structure to equiaxed structure in AZ31 welds (Figs. 5-2 and 5-3). The columnar-equiaxed transition mechanism due to micron-size second-phase particles has been discussed in reference [153].

Supercooling is another essential factor to control heterogeneous nucleation and microstructure refinement of alloys. Besides being an inoculant, the added Ti particles could slightly dissolve into the molten pool to become solute due to the possible Ti-Mg and Al-Ti peritectic reactions

[51]. However, it was reported that when the cooling rate was as low as 1.2°C/min, the resulting constitutional supercooling produced by solute zirconium in Mg alloy was measured to be less than 2.01°C [167]. The cooling rate could reach 4×10^5°C/min during resistance spot welding of AZ31 Mg alloy based on our numerical simulation results. The degree of thermal supercooling increases with the cooling rate according to the Hunt′s thermal model [70]. As a result, the supercooling produced by constitutional element segregation is much lower than the possible value of thermal supercooling during resistance spot welding. In other words, even though the added Ti particles could partially dissolve into the melt pool of AZ31 Mg alloy welds, the supercooling degree produced by any Ti solute should be much less than thermal supercooling during resistance spot welding. Therefore, the effect of Ti as a solute is much limited compared with that as the inoculant in this work.

Since the values of both G and R are affected by the geometry of the fusion boundary, both the solidification structure and the morphology are affected by the nature of the fusion boundary [29,31,178,187,188]. Differences in the peak temperature experienced by the material, the cooling rate and composition at different locations will lead to the formation of varying microstructures along the weld pool centreline. Further study on the effect of Ti addition on welding variables, temperature distribution, the fusion boundary, and width and shape of the fusion zones of the weldment is needed.

5.3.2. Crystallographic Analysis of Grain Refinement Due to Ti Addition

TEM examination showed that an orientation matching relationship was determined between the added Ti particles and Mg matrix in some grains of Ti. Meanwhile, microstructural examination showed that the added Ti particles were frequently observed at the centre of the

α-Mg grains. It is, therefore, reasonable to assume that the surfaces of the added Ti particles provided suitable nucleation sites for Mg matrix during solidification of welds.

Turnbull and Vonnegut [139] firstly proposed that the efficiency of a substrate in promoting heterogeneous nucleation depended on the crystallographic disregistry between substrate and the nucleated solid. The degree of mismatch of these parameters, *i.e.* the disregistry, is expressed as, $\delta=\Delta a_0/a_0$. In recent years, Zhang, Kelly and their colleagues [46,143-145] developed this crystallographic matching model to predict orientation relationships (OR) and actual atom mismatching across the interface between any two phases based on an assumption that the crystallographic relationships are governed by minimization of the strain energy of interfaces. According to the edge-to-edge matching model, the matching directions and matching planes are normally the close or nearly close packed directions and planes [46,143-145].

As hcp crystal structure, Mg and Ti have three groups of possible close or nearly close packed directions, *i.e.* $<11\bar{2}0>$, $<10\bar{1}0>$, and $<11\bar{2}3>$, and four groups of possible close or nearly close packed planes, *i.e.* base plane, {0002}, prismatic planes, $\{10\bar{1}0\}$, pyramidal planes, $\{10\bar{1}1\}$ and $\{10\bar{1}2\}$. An edge view of atomic positions on different planes in hexagonal lattice is illustrated in Fig. 5-13(a). The interatomic spacing along these potential matching directions is a for straight atom rows $<11\bar{2}0>$, $0.5a\sqrt{3}$ for zigzag rows $<10\bar{1}0>$, and $0.5(a^2+c^2)^{0.5}$ for zigzag rows $<11\bar{2}3>$ [143]. The distances between adjacent $\{10\bar{1}0\}$ planes can be either $\sqrt{3}\,a/6$ or $\sqrt{3}\,a/3$, respectively. If one considers the two planes spaced $\sqrt{3}\,a/6$ apart as being one corrugated plane, then the distance between corrugated planes remains a $\sqrt{3}\,a/2$, while the effective atomic density is doubled [143,189]. Meanwhile, the interplanar spacing is $\frac{ac\sqrt{3}}{\sqrt{4c^2+3a^2}}$ for two corrugated first-order pyramidal planes, $\{10\bar{1}1\}$, and $\frac{ac\sqrt{3}}{2\sqrt{3a^2+c^2}}$ for the corrugated second-order pyramidal planes, $\{10\bar{1}2\}$. The distance between adjacent {0002} base planes is always *c*/2 [189].

The lattice parameters used in the present work are a = 0.3209 nm and c = 0.5211 nm for Mg and a = 0.2951 nm, c = 0.4684 nm for Ti [51]. Tables 5-3 and 5-4 tabulate the relative interatomic spacing misfits along possible matching directions and interplanar spacing mismatches between possible matching planes between Ti phase and Mg matrix, respectively. It demonstrates that the minimum interatomic spacing misfit along $\langle 10\bar{1}0\rangle_{Mg}$ // $\langle 11\bar{2}3\rangle_{Ti}$ and $\langle 11\bar{2}3\rangle_{Mg}$ // $\langle 11\bar{2}0\rangle_{Ti}$ between the added Ti particles and Mg matrix is only 4%, which is much less than the critical value of 10% [143,190-192]. The selection of 10% as the critical interatomic spacing misfit value is based on Van der Merwe′s energy calculation [190-192] to obtain the minimum strain energy along different matching directions. On the other hand, the interplanar spacing mismatch is only 2% for $\{0002\}_{Mg}$ // $\{10\bar{1}0\}_{Ti}$ and 4% for $\{10\bar{1}2\}_{Mg}$ // $\{10\bar{1}0\}_{Ti}$. These interplanar spacing mismatches are much lower than the critical value of 6%, as well [143,193,194]. The 6% is an estimation value through examination of the reported orientation relationship between matching planes to form an interplanar matching relationship without large angle rotation of the matching planes [193,194]. The TEM examination provided evidence for the existence of orientation relationships $(0002)_{Mg}$ // $(10\bar{1}0)_{Ti}$ and $[01\bar{1}0]_{Mg}$ // $[1\bar{2}1\bar{3}]_{Ti}$ between some grains of the added Ti particles and Mg matrix in this work (Fig. 5-10). Therefore, the reason why Ti is an efficient refiner of AZ31 Mg alloy could be explained by this crystallographic matching, which led to a low interfacial energy and promoted the nucleation of Mg matrix on the surface of the Ti inoculants in the period of heterogeneous nucleation. However, it is worth noting that crystallographic matching was observed in partial interfaces between the added Ti particles and Mg matrix. Furthermore, some inoculants, such as Al_8Mn_5 intermetallic compound and pure Mn powder, which have a large theoretical

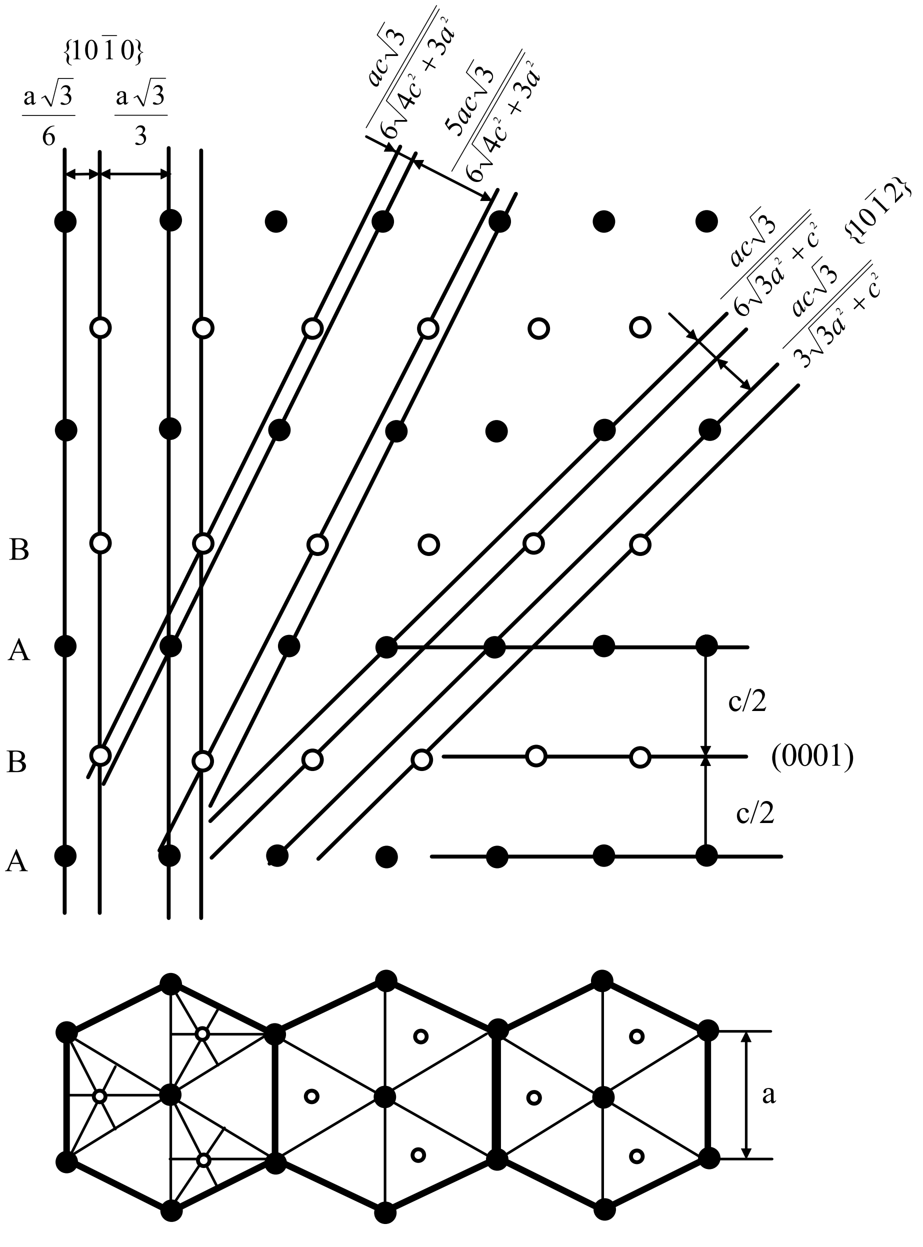

Fig. 5-13. Edge view of $\{10\bar{1}10\}$, $\{10\bar{1}1\}$, $\{10\bar{1}2\}$, and $\{0001\}$ planes in hcp metals.

Table 5-3. Interatomic Spacing Misfits along Possible Matching Directions between Ti Phase and Mg Matrix

Matching Directions		$\langle 11\bar{2}0\rangle_{Mg}$// $\langle 11\bar{2}0\rangle_{Ti}$	$\langle 10\bar{1}0\rangle_{Mg}$// $\langle 10\bar{1}0\rangle_{Ti}$	$\langle 11\bar{2}3\rangle_{Mg}$// $\langle 11\bar{2}3\rangle_{Ti}$	$\langle 10\bar{1}0\rangle_{Mg}$// $\langle 11\bar{2}3\rangle_{Ti}$	$\langle 11\bar{2}3\rangle_{Mg}$// $\langle 11\bar{2}0\rangle_{Ti}$	$\langle 10\bar{1}0\rangle_{Mg}$// $\langle 11\bar{2}0\rangle_{Ti}$
Interatomic Spacing, nm	Mg	0.3209	0.2779	0.3060	0.2779	0.3060	0.2779
	Ti	0.2951	0.2556	0.2768	0.2768	0.2951	0.2951
Interatomic Misfit, %		8	8	10	4	4	6

Table 5-4. Interplanar Spacing Mismatches between Possible Matching Planes of Ti Phase and Mg Matrix

Matching Planes		$\{0002\}_{Mg}$// $\{0002\}_{Ti}$	$\{10\bar{1}0\}_{Mg}$// $\{10\bar{1}0\}_{Ti}$	$\{10\bar{1}1\}_{Mg}$// $\{10\bar{1}1\}_{Ti}$	$\{10\bar{1}2\}_{Mg}$// $\{10\bar{1}2\}_{Ti}$	$\{0002\}_{Mg}$// $\{10\bar{1}0\}_{Ti}$	$\{10\bar{1}1\}_{Mg}$// $\{10\bar{1}0\}_{Ti}$	$\{10\bar{1}1\}_{Mg}$// $\{0002\}_{Ti}$
Interplanar Spacing, nm	Mg	0.2605	0.2779	0.2452	0.1901	0.2605	0.2452	0.2452
	Ti	0.2342	0.2556	0.2243	0.1727	0.2556	0.2556	0.2342
Interplanar Mismatch, %		10	8	9	9	2	4	4

interatomic misfit with Mg matrix according to the edge-to-edge model [143-145], were observed to refine the microstructure of AZ 31 Mg alloy welds in the fusion zone [151,153,195]. Therefore, a good crystallographic matching between the added inoculants and the refined matrix is a sufficient condition rather than necessary one. A further study is needed so as to establish the detailed relationship between the crystallographic matching and the potency of inoculants.

5.3.3. Critical Size of Potent Inoculants

Heterogeneous nucleation would occur ahead of the columnar front once the supercooling suffices to induce nucleation, depending upon the inoculant size. The dependence of nucleation efficiency on the size and surface properties of the foreign nucleating particles can be expressed by Fletcher's spherical substrate model [108,132], which is a basic model for understanding heterogeneous nucleation phenomena.

Based on the Fletcher's model, Qian *et al.* [132,167] gave an inverse relationship between the critical nucleation radius, r^*, and supercooling degree, ΔT, in α-Mg:

$$r^* = 0.354/\Delta T \qquad (5\text{-}1)$$

Based on TEM results, we simplify the added Ti particles as hexagonal platelets which contain a few $[01\bar{1}0]$ faces where α-Mg nucleation occurred. The relationship between the polycrystal Ti particles and Mg embryo can be schematically illustrated in Fig. 5-13. The length of a side of hexagonal platelets is equal to the radius of hexagon, $d/2$.

Based on the Fletcher′s classic nucleation theory [108,132], the substrate radius needs to be at least five times the critical embryo radius to enhance heterogeneous nucleation. Therefore, the size effect of inoculant is most noticeable when $d/2r = 5$, where r is the radius of a spherical embryo. This indicates that the critical size of the added particles as potent inoculants of alloys should be larger than $10r^*$ so that they become the most efficient refiners.

For the added Ti inoculant with a shape of hexagonal polycrystal platelets, the critical condition for free growth of the crystal through hexagonal platelets should be.

$$d = 10r^* \qquad (5\text{-}2)$$

Bramfitt [141] measured the supercooling degree of liquid iron added with different inoculants during solidification, and suggested an empirical equation between supercooling and lattice disregistry:

$$\Delta T_c = \delta^2/8 \qquad (5\text{-}3)$$

TEM examination in this work has showed that there present a set of orientation relationships between the added Ti particle and Mg matrix: *i.e.* $(0002)_{Mg}$ // $(10\bar{1}0)_{Ti}$ and $[01\bar{1}0]_{Mg}$ // $[1\bar{2}1\bar{3}]_{Ti}$. The interplanar and interatomic disregistries between them were calculated to be 2% and 4%, respectively (Tables 5-3 and 5-4). Therefore, substituting the interplanar disregistry and interatomic misfit with 2% and 4%, into equation (5-3), supercooling is 0.5° for interplanar disregistry and 2° for interatomic disregistry.

According to equation (5-1), critical nucleation radius, r^*, is calculated to be 0.708 μm and 0.177 μm when the supercooling is 0.5° and 2°, respectively. Furthermore, based on equation (4-2), the critical size of potent Ti inoculant is estimated to be in the range of 1.8 to 7 μm. This result demonstrates that the critical size of the added Ti particles should be larger than 1.8 μm in order to effectively refine grain size of Mg matrix. Therefore, when Ti particles of ~8 μm in diameter were added into the molten pool, they could become potent inoculants by providing heterogeneous sites for new grain nucleation.

In this work, only a low degree of supercooling is required for nucleation of Mg matrix on the surface of Ti particles since the added Ti particles have a good matching with the refined Mg matrix. The cooling rate of AZ31 Mg alloy welds during resistance spot welding is high enough to satisfy this requirement of supercooling.

5.3.4. Strengthening Mechanisms of AZ31 Welds with the Addition of Ti

The results of tensile-shear measurement revealed that the strength and ductility of AZ31 Mg alloy welds were improved with the addition of Ti particles. This can be attributed to the refinement of grain size and morphology in the fusion zone in these welds [141]. It is well accepted that the finer grain size corresponds to the higher yield strength and ductility [151,153,196]. On the other hand, microstructural characterization of the materials revealed a reasonably uniform distribution of Ti particles with good interfacial integrity between the matrix and the added phases (Figs. 5-6, 5-7, 5-10, 5-11, and 5-12). The Ti particles are harder than the matrix of Mg. The harder Ti particles in the fusion zones are also expected to provide dispersion strengthening as reinforcement *i.e.* Orowan strengthening [197].

Fine grain formation during solidification promotes the flow of molten metal to feed shrinkage, resulting in smaller and more uniformly dispersed shrinkage or gas porosity. Fine grains also provide a complex network of grain boundaries, reducing the tendency for segregation of alloy elements [30,39]. These factors contribute to the improvement of strength and ductility of welds, as well.

5.4. Summary

1. The fusion zone of AZ31 magnesium alloy resistance spot welds could be divided into columnar dendritic zone (CDZ) and equiaxed dendritic zone (EDZ). The CDZ produced in the vicinity of the fusion boundaries of the as-received AZ31 Mg alloy welds was significantly suppressed to within a width of 320 μm due to the addition of Ti powders. A more randomly oriented dendritic structure with short primary arms replaced the well-developed primary arms in the welds with the addition of Ti powders.
2. The equiaxed dendritic zone (EDZ) was formed in the central regions of Mg alloy welds both without and with the addition of Ti. The coarse equiaxed dendrites in the welds without the addition of Ti were efficiently refined by adding titanium powders into the molten pool. The average diameter of the flower-like equiaxed dendrites in the welds with Ti addition was much smaller than that without the addition of Ti. It was approximately 65μm in AZ31 without the addition of Ti, whereas only about 20μm with the addition of Ti.
3. The ultimate tension-shear load of the AZ31 alloy welded at 26 kA with an addition of Ti increased by 38 percent from 4076 N to 5619 N in comparison with the welds without adding Ti. Meanwhile, the displacement rose by 28 percent from 1.09 to 1.40. When the welding current increased to 30 kA, the ultimate tension-shear load increased by 16 percent from 4796 N to 5562 N, and the displacement increased by 17 percent from 1.12 to 1.31.
4. Ti inoculant could provide potent heterogeneous nucleation sites for the Mg matrix due to a good crystallographic matching between some grains of the added Ti particles and

Mg matrix. The orientation relationship between those Ti grains and AZ 31 Mg alloy matrix was determined to be $[01\bar{1}0]_{Mg}$ // $[1\bar{2}1\bar{3}]_{Ti}$ and $(0002)_{Mg}$ // $(10\bar{1}0)_{Ti}$.

5. It is suggested that the diameter of the added Ti inoculant should be larger than 1.8 μm in order to promote efficient nucleation of fine Mg grains. The refined microstructure in the fusion zone could partially contribute to the improvement of tensile-shear properties of AZ 31 resistance spot welds, even though the effect of heat-affected zone (HAZ) on tensile-shear properties of welds is significant when the nugget pullout failure occurs.

6. Heterogeneous Nucleation on Inoculant Particles in the Fusion Zone of Welds during Non-equilibrium Solidification

The heterogeneous nucleation of a condensed phase on the surface of a substrate is a problem of broad scientific interest and technological importance. The ability to control such a process lies at the heart of the development of a novel technology or microstructure, because nucleation controls to a large extent the initial structure type, size scale, and spatial distribution of the product phases [29,30,31,108,110]. In the metal casting and welding industries, for instance, it is a common practice to introduce inoculants into a liquid metal to promote the formation of fine, uniform, and equiaxed grains [29,30,31,42,110,153,198]. However, the mechanism of refinement of grain size through inoculation is not fully understood, especially in welding where the solidification process is extremely non-equilibrium [29,30,31,198,199]. Consequently, industrial processes still rely on empirical approaches to select inoculants for grain refinement.

Columnar and equiaxed dendritic grains are two primary microstructures formed in Mg alloy fusion welds [153,198]. The growth of columnar grains initiating from the fusion boundary often terminates with the appearance of equiaxed grains or, a band of equiaxed grains due to the action of heterogeneous nucleation as the columnar grains propagate to the center of the fusion zone. This process is known as the columnar-to-equiaxed transition (CET) [29,30,31]. Therefore, the heterogeneous nucleation in front of the solid / liquid interface plays a dominant role in promoting the CET and controlling the microstructure′s morphology and size in the fusion zone of Mg alloy welds.

The physical processes and parameters that control the solidification microstructure include: solute diffusion, thermal diffusion, and interfacial energy [29,30,31,64,86]. Mass transport (*i.e.* solute diffusion) and heat transport (*i.e.* thermal diffusion) are two primary thermodynamic processes, which simultaneously take place in the front of a solid/liquid interface and strongly depend on the growth rate of that interface, *R*, during solidification. When *R* is low, microstructural morphology and size are dominantly controlled by the solutal diffusion. The effect of solute microsegregation on heterogeneous nucleation has been systematically studied [70,101,102,134,199,200,201]. The model of constitutional supercooling driven heterogeneous nucleation has successfully predicted the heterogeneous nucleation and growth behaviour of alloys at this condition [70,101,102,134,199,200,201]. On the other hand, at the high *R*, local non-equilibrium effects begin to play an important role with the increasing of the *R* during rapid solidification [114,199,202,203].

Rapid solidification processes produce microstructure with refined grain sizes compared with conventional solidification [114,199,202,203]. The understanding of microstructure formation under rapid solidification has therefore become a major issue in solidification theory. Various models have been proposed to predict the rapid heterogeneous nucleation and growth behavior in supercooled metals and alloys [102,114,199,202,203]. In comparison, some traditional metallurgical processes could also produce rapid solidification microstructure. As an example, the cooling rate of liquid in the fusion zone of resistance spot welds could reach as high as 10^4 to $l0^6$ K/s, which is the cooling rate range of typical rapid solidification processes [198]. There have been few quantitative studies on the dependence of microstructural morphology and size on the solidification condition of liquid and the interfacial properties of inoculants during resistance spot welding.

Heterogeneous nucleation into a specific crystallographic phase is characterized by an activation energy barrier to form a nucleus of critical size in the supercooled liquid, which is determined mainly by the interfacial energy between inoculants and matrix and the local thermodynamic supercooling, ΔT [29,30,31,108,110]. Both reducing the interfacial energy, influenced by the crystallograpic lattice disregistry between inoculants and matrix, and increasing the supercooling, *i.e.* driving force for nucleation, can promote nucleation, and thus grain refinement [29,30,31,109]. It has been generally accepted that dramatically increasing the cooling rate ($\mathrm{d}T/\mathrm{d}t$) could increase the supercooling degree of the liquid [64,86,114,116].

There are two objectives for this work. One is to study heterogeneous nucleation behaviour on inoculant particles, inspired by observations of microstructural refinement in the magnesium alloy welds due to the introduction of different inoculant particles. On the basis of assessment of the inoculant efficiency in refining microstructure of an AZ31 Mg alloy weld according to the crystallographic matching model [143-146,139,204], the present work is concerned with examination of crystallograpic orientation relationships using high resolution transmission electron microscopy (HR-TEM). The second objective is to study the effect of cooling rate on heterogeneous nucleation and the resulting microstructure in the AZ31 Mg alloy welds by designing a variety of welding procedures with different cooling rates.

6.1. Experimental Procedure

The detailed welding process and parameters have been described in previous chapters. The welding current was 26 kA under an applied electrode force of 4 kN on the surface of samples at a weld time of 8 cycles (1 cycle = 0.0167 S). Different post-weld holding times without and with a slope of post-welding heating current were used to change the cooling rate of the liquid phase in the fusion zone. The detailed welding procedure is schematically illustrated in Figs. 6-1(a) and 6-1(b). The welding procedures, named as WP1 and WP2, had 30 and 0 cycles post-weld hold without heating current, respectively (Fig. 6-1(a)). WP3, WP4, and WP5 were welding procedures in which the weld time was followed by different slopes of post-welding heating current so as to decrease the cooling rate of liquid during solidification in the fusion zone (Fig. 6-1(b)).

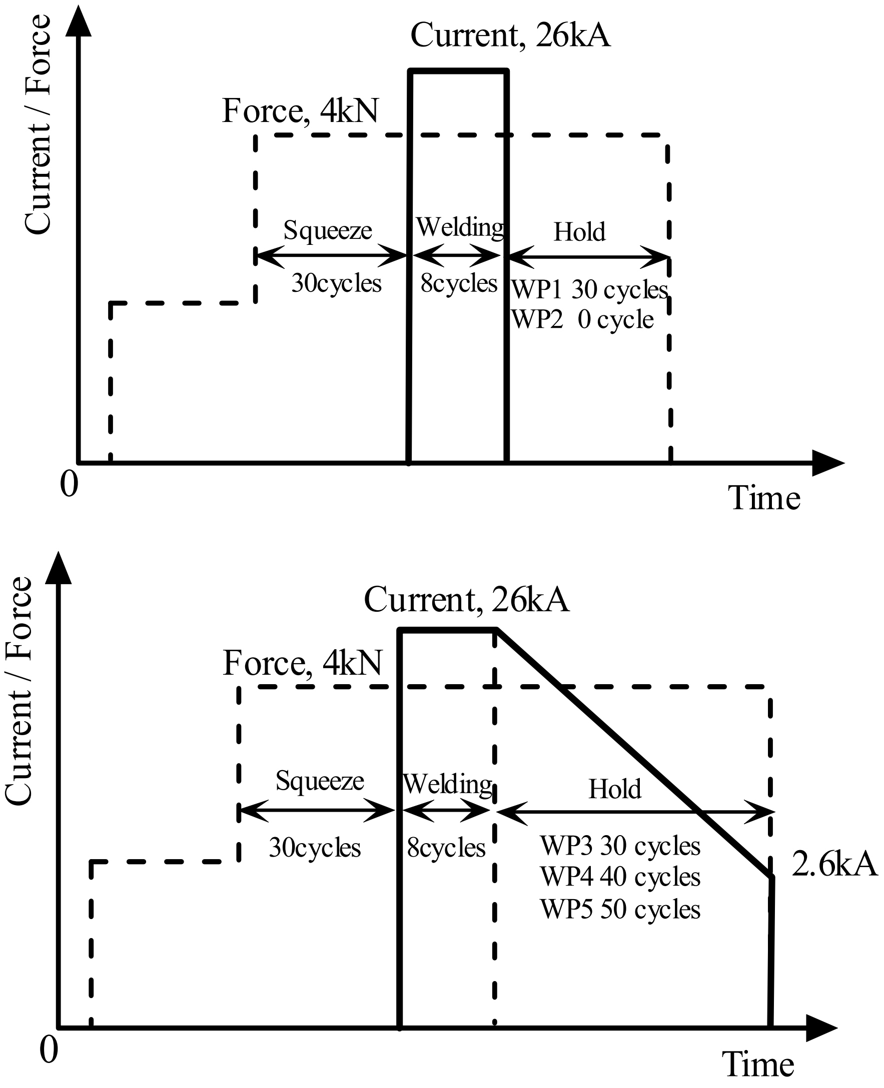

Fig. 6-1. Five welding procedures used in this work, (a) different post-weld holding times without current, (b) different post-weld holding times with a slope post-welding current. (1cycle=0.0167seconds).

Three types of inoculants, Ti, Al_8Mn_5, and Mn with different crystal structures were introduced into the fusion zone of the AZ31 Mg alloy welds during resistance spot welding. The volume fraction of inoculant in the fusion zone was estimated to be about 0.5% using polished planar cross-sectional specimens of the fusion zone by the manual point count procedure according to standard ASTM E562-05.

The microstructures of AZ31 welds without and with an addition of inoculants were examined using an optical microscope. In order to analyze the orientation relationship and lattice matching, TEM foils containing the interface of the inoculant particles and Mg matrix were prepared using the Focused Ion Beam (FIB) (Zeiss IV Vision 40 Focused Ion Beam / Field Emission Scanning Electron Microscope) technique. The interfacial characteristics were observed with a JEOL JEM-2010F field emission transmission electron microscope and high-resolution TEM (HR-TEM) equipped with an Oxford ultra-thin window detector energy-dispersive spectrometer (EDS).

6.2. Results

6.2.1. Microstructural Refinement in AZ31 Welds due to Inoculants

Metallographic examination showed that the columnar dendritic zone (CDZ) and equiaxed dendritic zone (EDZ) could be easily distinguished in the microstructures of the fusion zones of AZ31 alloys welded at 26kA with and without adding inoculants, as shown in Figs. 6-2(a) through 6-2(d). The main differences in solidification microstructures were in the length of the CDZ in the vicinity of the fusion boundary and the diameter of equiaxed dendritic grains in the central areas. Well-developed columnar dendritic grains perpendicular to the fusion boundary within a band of 600μm were produced in the alloy without adding inoculant (Fig. 6-2(a)). In contrast, in weldments with added inoculants, columnar structures were restricted to a narrow strip region and the ratio of length over width of columnar dendritic grains was small (Figs. 6-2(b) to 6-2(d)). The length of CDZ was 380μm, 400μm, and 390μm in the welds with an addition of Ti, Al_8Mn_5, and Mn, respectively. As the solidification progressed towards the centre of the fusion zone, equiaxed dendritic structure occurred in all the welds. The diameter of the flower-like dendritic structures in the alloy with inoculants was smaller than that in the alloy without adding inoculants, as shown in Figs. 6-3(a) to 6-3(d). The average diameter of the flower-like dendrites was about 40μm, 55μm, and 50μm in alloys with the addition of inoculant Ti, Al_8Mn_5, and Mn, respectively. In comparison, it was 85μm in the alloy without inoculant.

6.2.2. Dependence of Inoculant Potency on the Lattice Disregistry

The added inoculants should have a low interfacial energy, σ_{is}, with the solid being nucleated so as to be effective inoculants [139, 204,143-145,205]. Unfortunately, no experimental

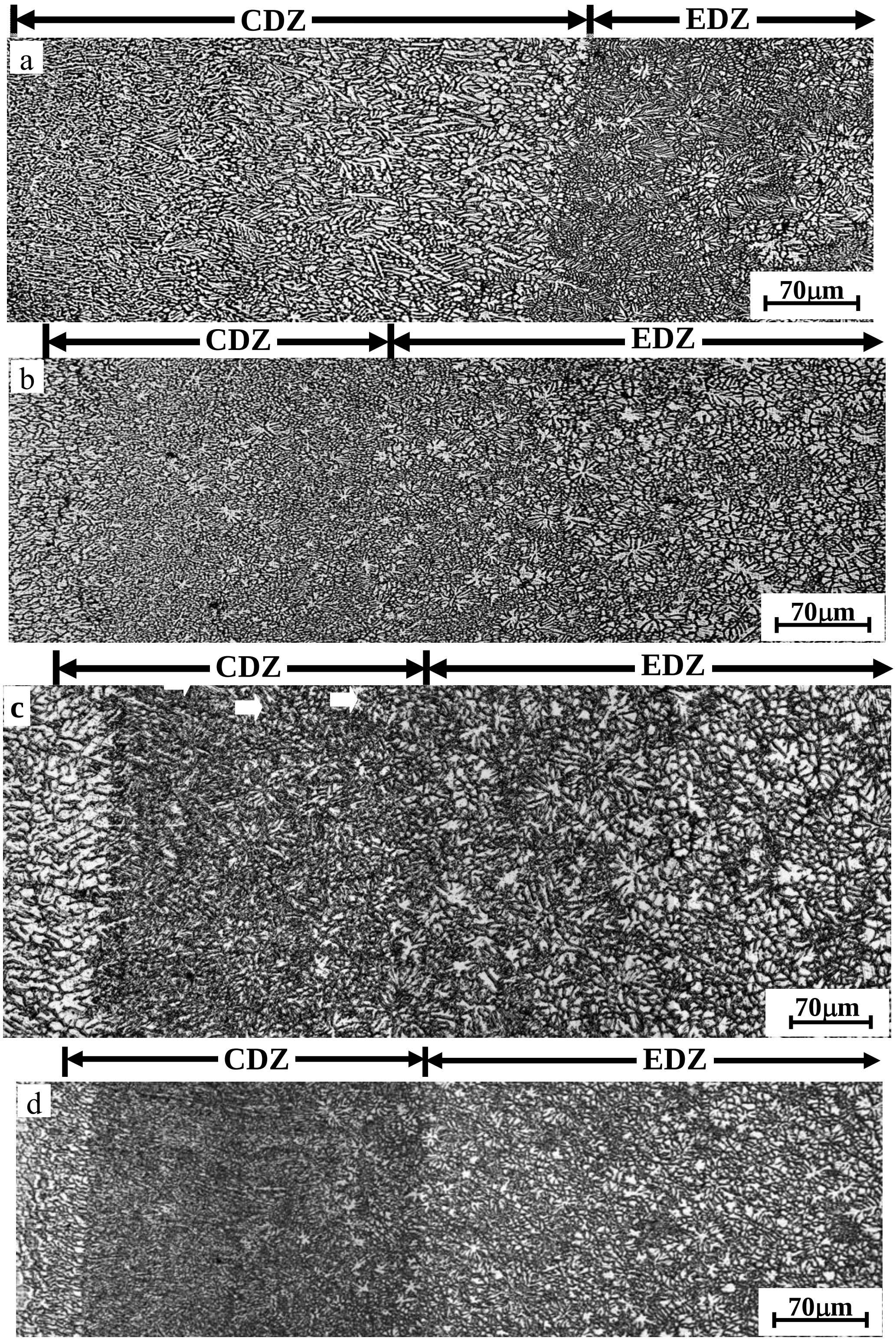

Fig. 6-2. Effect of the added inoculants on microstructure and the length of CDZ in AZ31 Mg alloy resistance spot welds, (*a*) as-received, (*b*) added Ti, (*c*) added Al_8Mn_5, (*d*) added Mn. CDZ — Columnar dendritic zone, EDZ — Equiaxed dendritic zone

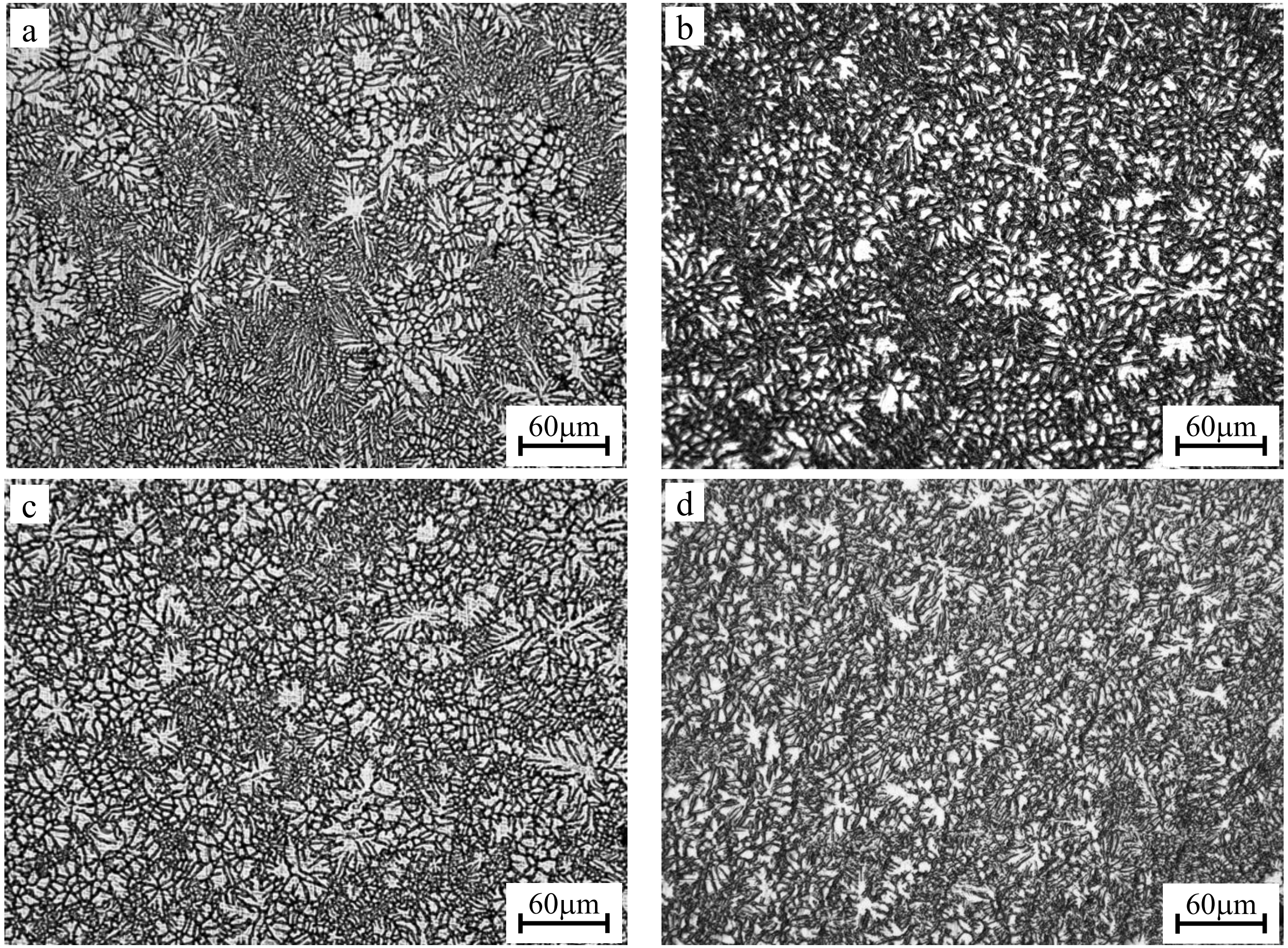

Fig. 6-3. Effect of the added inoculant particles on diameter of equiaxed dendritic grains in AZ31 Mg alloy resistance spot welds, (*a*) as-received, (*b*) added Ti, (*c*) added Al_8Mn_5, (*d*) added Mn.

techniques have been shown to directly measure the interfacial energy of a solid nucleus, so far. Indirectly, interfacial energies have been determined by supercooling experiments on small droplets of pure metals supposing that the maximum supercooling observed corresponds to the limiting case of homogeneous nucleation [206,207]. Theoretically, the crystallographic disregistry along the matching directions and planes between matrix and the inoculants has been used to evaluate the potency of inoculant particles in promoting heterogeneous nucleation according to the crystallographic matching model, which was proposed by Turnbull and Vonnegut [139] and further developed by Zhang *et al.* [143-145,205,204]. Therefore, the crystallographic lattice disregistry could be assumed to be proportional to the interfacial energy, $\sigma_{is,}$ between the added inoculants and the nucleated solid, and could be used to evaluate the efficiency of grain refinement from the perspective of crystallography. The crystallographic lattice disregistry is expressed as [139]

$$\delta=\Delta a_0/a_0, \tag{6-1}$$

where Δa_0 is the difference of lattice parameters, a_0, between inoculant and the nucleated solid for a low-index plane or direction.

The lattice disregistries along the possible matching directions and planes between Mg matrix and the inoculants, Ti, Al_8Mn_5, and Mn have been previously calculated based on the crystallographic matching model [139,143-145,205,204], as listed in Table 6-1. Both Mg and Ti have the hexagonal close-packed (hcp) crystal structure. It has been shown that the minimum interatomic spacing disregistry between the Ti inoculant and Mg matrix along $\langle 10\bar{1}0\rangle_{Mg}$ // $\langle 11\bar{2}3\rangle_{Ti}$ and $\langle 11\bar{2}3\rangle_{Mg}$ // $\langle 11\bar{2}0\rangle_{Ti}$ is only 4%, and the interplanar spacing disregistry is only 2% for $\{0002\}_{Mg}//\{10\bar{1}0\}_{Ti}$ and 4% for $\{10\bar{1}1\}_{Mg}//\{10\bar{1}0\}_{Ti}$. The intermetallic compound, Al_8Mn_5, has a rombohedral crystal structure. The interatomic matching along the close-packed or nearly close-packed directions between Mg and Al_8Mn_5 compound is very poor [145]. There is only one direction pair, *i.e.* $<10\bar{1}0>_{Mg}/<10\bar{1}1>_{Al8Mn5}$, along which the interatomic spacing disregistry is small, *i.e.* 7.4%. However, the two plane pairs, $(0002)_{Mg}//(30\bar{3}3)_{Al8Mn5}$ and $(0002)_{Mg}//(33\bar{6}0)_{Al8Mn5}$, involved in this direction pair have very large interplanar disregistries, *i.e.* 17.8% and 19.5%, respectively [145]. Mn has a body-centered cubic (bcc) structure. The interatomic and interplanar disregistries between Mg and Mn are much larger along the possible orientation relationship $[2\bar{1}\bar{1}0]_{Mg}$ // $[226]_{Mn}$ than the other inoculant particles [144].

In brief, Ti has the best matching with the Mg matrix, and Mn has the worst matching. Therefore, Ti is expected to be the most efficient grain refiner, while Mn is the least efficient grain refiner in comparison with Ti and Al_8Mn_5 inoculant particles for the Mg alloy solidification from the perspective of crystallography.

Table 6-1. Interatomic and Interplanar Spacing Disregistries along Possible Matching Directions and Planes between Ti, Al_8Mn_5, Mn Inoculant Particles and Mg Matrix

Mg/Ti	Matching plane or direction	$\langle 10\bar{1}0\rangle_{Mg}//$ $\langle 11\bar{2}3\rangle_{Ti}$	$\langle 11\bar{2}3\rangle_{Mg}//$ $\langle 11\bar{2}0\rangle_{Ti}$	$\{0002\}_{Mg}//$ $\{10\bar{1}0\}_{Ti}$	$\{10\bar{1}1\}_{Mg}//$ $\{10\bar{1}0\}_{Ti}$
	Disregistry, %	4	4	2	4
Mg/Al_8Mn_5	Matching plane or direction	$\langle 10\bar{1}0\rangle_{Mg}//$ $\langle 10\bar{1}1\rangle_{Al8Mn5}$	$\langle 11\bar{2}0\rangle_{Mg}//$ $\langle 1\bar{1}02\rangle_{Al8Mn5}$	$\{0002\}_{Mg}//$ $\{30\bar{3}3\}_{Al8Mn5}$	$\{0002\}_{Mg}//$ $\{33\bar{6}0\}_{Al8Mn5}$
	Disregistry, %	7.4	10.8	17.8	19.5
Mg/Mn	Matching plane or direction	$\langle 11\bar{2}0\rangle_{Mg}//$ $\langle 111\rangle_{Mn}$	$\langle 11\bar{2}0\rangle_{Mg}//$ $\langle 226\rangle_{Mn}$	$\{10\bar{1}0\}_{Mg}//$ $\{330\}_{Mn}$	$\{10\bar{1}1\}_{Mg}//$ $\{330\}_{Mn}$
	Disregistry, %	20.1	35.4	24.4	14.3

6.2.3. Crystallographic Orientation Relationship and Lattice Matching Analysis

A direct evidence of crystallographic or lattice matching is the existence of orientation relationship between the matrix and the added inoculant particles. In order to analyze the interfacial characteristics, a large number of TEM foils containing these interfaces of the added inoculant particles and α-Mg matrix were extensively examined using HR-TEM by tilting the TEM foils to allow the incident beam to be parallel to various low index crystal directions of either the inoculant particles or the α-Mg matrix.

An orientation matching relationship between the added Ti particles and Mg matrix, *i.e.* $[01\bar{1}0]_{Mg}$ // $[1\bar{2}1\bar{3}]_{Ti}$ and $(0002)_{Mg}$ // $(10\bar{1}0)_{Ti}$ had been determined in some grains of Ti polycrystal particles in our previous paper [174]. Further HR-TEM examination was carried out to explore the possible lattice matching in this work. Fig. 6-4(a) and (b) showed a TEM image and the corresponding HR-TEM lattice image of a typical interface between Ti particle and Mg matrix, respectively. The selected area electron diffraction patterns (SADPs) of Ti inoculant grain and the Mg matrix were inserted in the right-down corner and left-upper corner of Fig.6-4(a), respectively. The SADPs revealed that the Mg matrix was exactly located on the $[01\bar{1}1]$ zone axis, when the thin foil was tilted to align the incident beam parallel to the Ti $[01\bar{1}0]$ orientation. The lattice matching was not observed between this added Ti particle and the Mg matrix, even though an orientation relationship, $[01\bar{1}0]_{Ti}$// $[01\bar{1}1]_{Mg}$, was determined.

Figs. 6-5(a) through 6-5(e) show a typical interface and the SADPs between an Al_8Mn_5 particle and α-Mg matrix, when the TEM foil was tilted to align the incident beam parallel to the Al_8Mn_5 $[01\bar{1}0]$ orientation. The SADP taken from the area including both the Al_8Mn_5 particle and the α-Mg grain is shown in Fig. 6-5(b). The diffraction spots are indexed in Fig. 6-5(c). It was found that the α-Mg matrix was parallel to $[01\bar{1}1]$ orientation, while the Al_8Mn_5 intermetallic compound was in the $[01\bar{1}0]$ zone axis orientation. This indicates that the orientation relationship between the added Al_8Mn_5 and Mg matrix is $[01\bar{1}0]_{Al8Mn5}$ // $[01\bar{1}1]_{Mg}$.

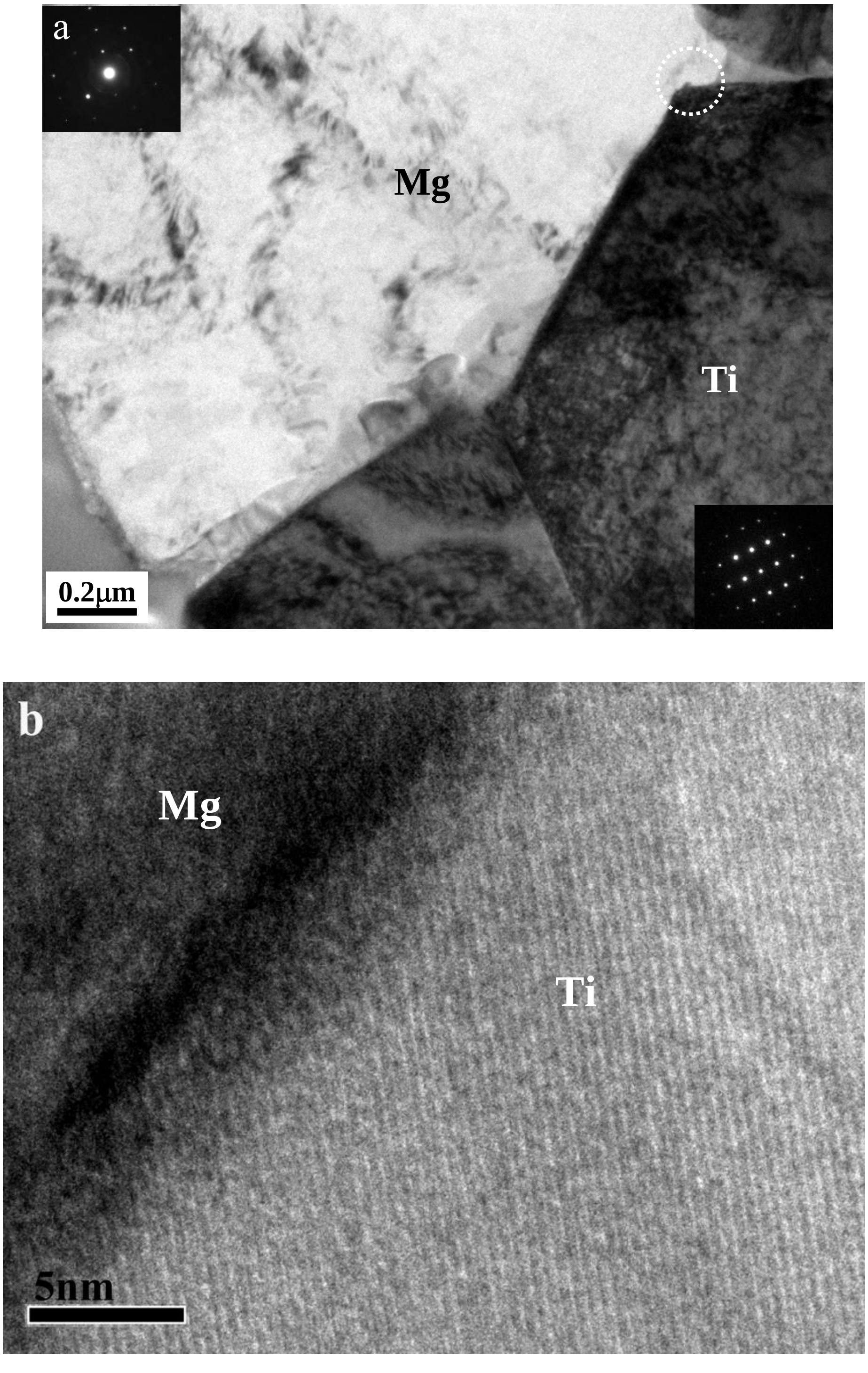

Fig. 6-4. The interface between the added titanium particles and Mg matrix. (*a*) TEM and (*b*) High resolution TEM images. The dashed circle in (a) shows the site of HR-TEM image. The incident beam is parallel to Ti [01$\bar{1}$0], the Mg matrix is right on [01$\bar{1}$1] orientation.

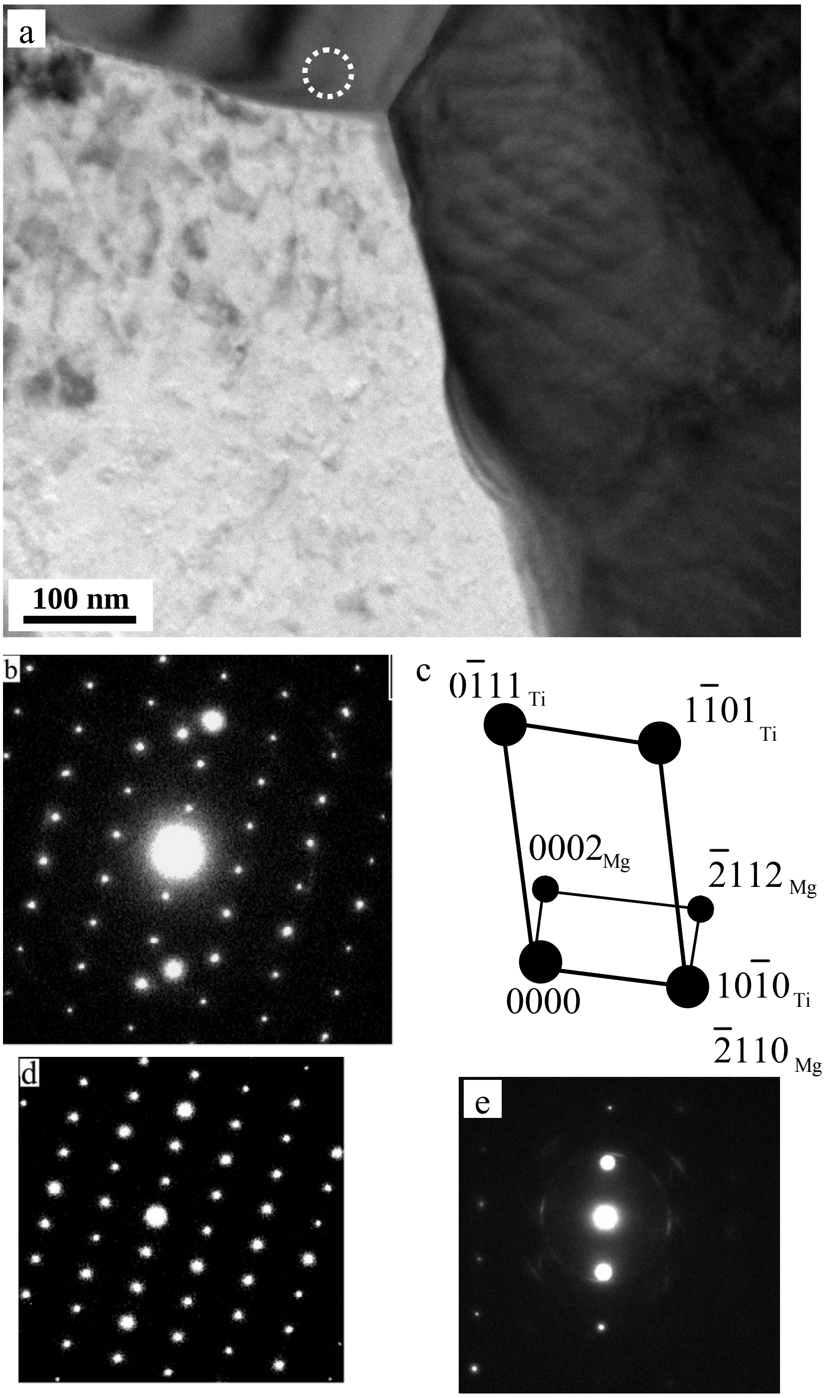

Fig. 6-5. The interface between the Al_8Mn_5 particles and Mg matrix. The incident beam is parallel to Al_8Mn_5 [01$\bar{1}$0], the Mg matrix is right on [01$\bar{1}$1] orientation. (*a*) TEM image, (*b*) selected-area diffraction pattern (SADP) taken from both α-Mg matrix and the added Ti particles, (*c*) schematic diagram of (b) SAD pattern indexed in Al_8Mn_5 [10$\bar{1}$1] zone direction, (*d*) the corresponding SADP of Al_8Mn_5 particle, incident beam ||$[01\bar{1}0]_{Al8Mn5}$, (*e*) SADP of the Mg matrix, incident beam || $[01\bar{1}1]_{Mg}$.

Fig. 6-6(a) and (b) presents HRTEM lattice images of the interface between the Al_8Mn_5 inoculant particle and Mg matrix, when the thin foil was observed along the direction of Al_8Mn_5 $[01\bar{1}0]$ (Fig. 6-6(a)) and $[2\bar{1}\bar{1}0]$ grains (Fig. 6-6(b)), respectively. A crystallographic matching interface was observed between the Al_8Mn_5 inoculant particle and Mg matrix, as indicted by arrows in Fig. 6-6(a). The measured interplanar spacing of the crystal planes in Al_8Mn_5 (0002) was 0.82 nm, as indicated by two parallel dashed lines in Fig. 6-6(a). This value is comparable with the corresponding d-spacing of 0.793 nm calculated according to the reported lattice parameters, $a = 1.265$ nm and $c = 1.586$ nm, for the rhombohedral structured Al_8Mn_5 intermetallic compound at 25°C [51]. With TEM and HRTEM, both the orientation relationship and lattice matching were observed at the interface of the Al_8Mn_5 and α-Mg, when the incident beam was parallel to the $[01\bar{1}0]$ orientation of Al_8Mn_5.

Typical TEM image of the interface between an added Mn particle and Mg matrix is shown in Fig. 6-7, when the incident beam was parallel to $[111]_{Mn}$. The SADP analysis of Mn showed that the added Mn inoculant particles are single crystal through observing three different TEM interface-containing foils. Fig. 6-8(a) shows bright-field and Fig. 6-8(b) to (d) show some dark-field images of Mg matrix, which were observed using different selected spots B, C, D in Fig.6(e), in the vicinity of the Mn/Mg interface, when the TEM foil was tilted to align the incident beam parallel to the Mn [111] orientation (Fig. 6-8(f)). A layer of nano-sized grains was observed in the vicinity of the interface in the Mg matrix. Multi-diffraction rings, which were observed in the Mg matrix, imply that the grains of Mg matrix have been refined to submicron scale, as shown in Fig. 6-8(e). The average grain size, estimated from Figs. 6-8(a) and 6-8(b) to (d), was about 35 ~ 40 nm. Distribution of elements across the interface between

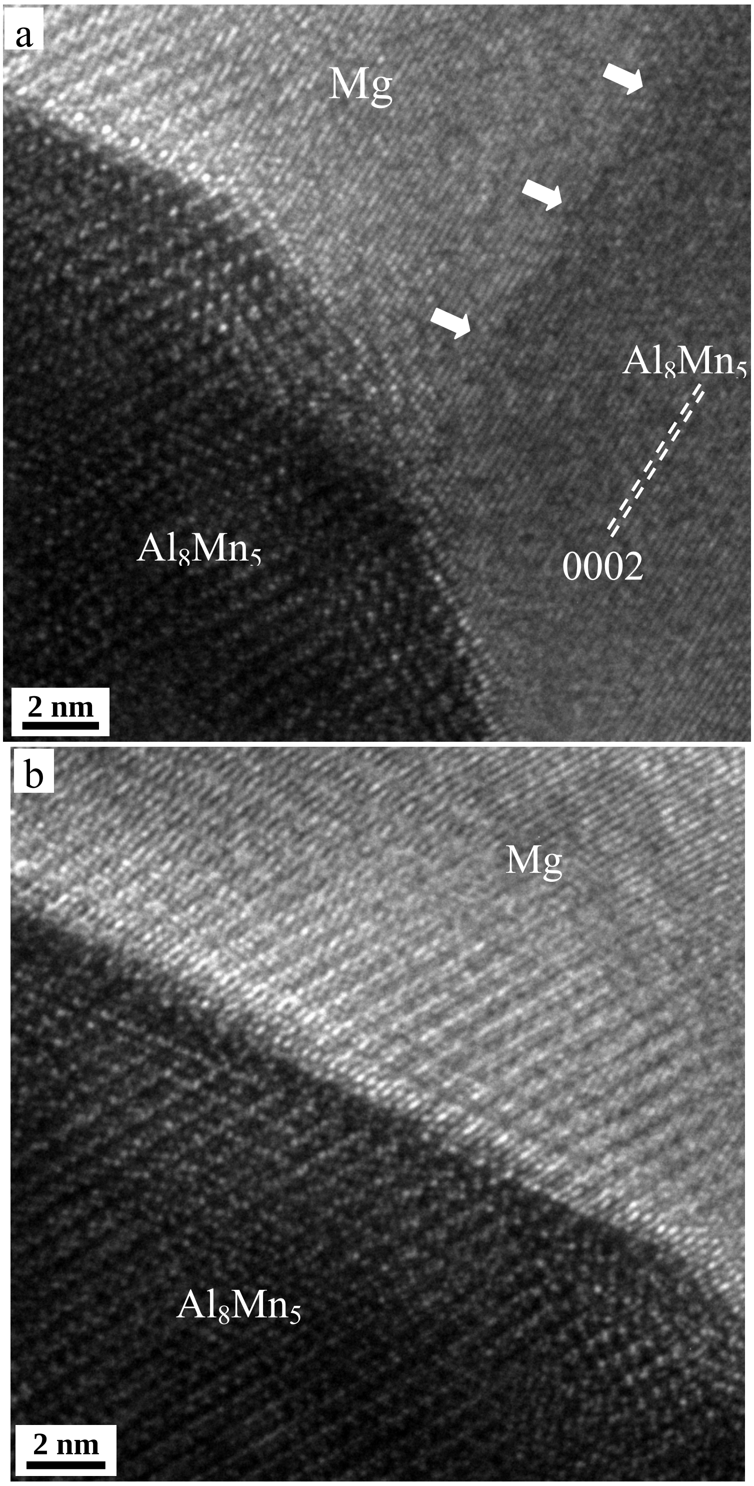

Fig. 6-6. The interface between the Al_8Mn_5 particles and Mg matrix and its HRTEM image. (*a*) incident beam // $[01\bar{1}0]_{Al8Mn5}$, (*b*) incident beam || $[2\bar{1}\bar{1}0]_{Al8Mn5}$.

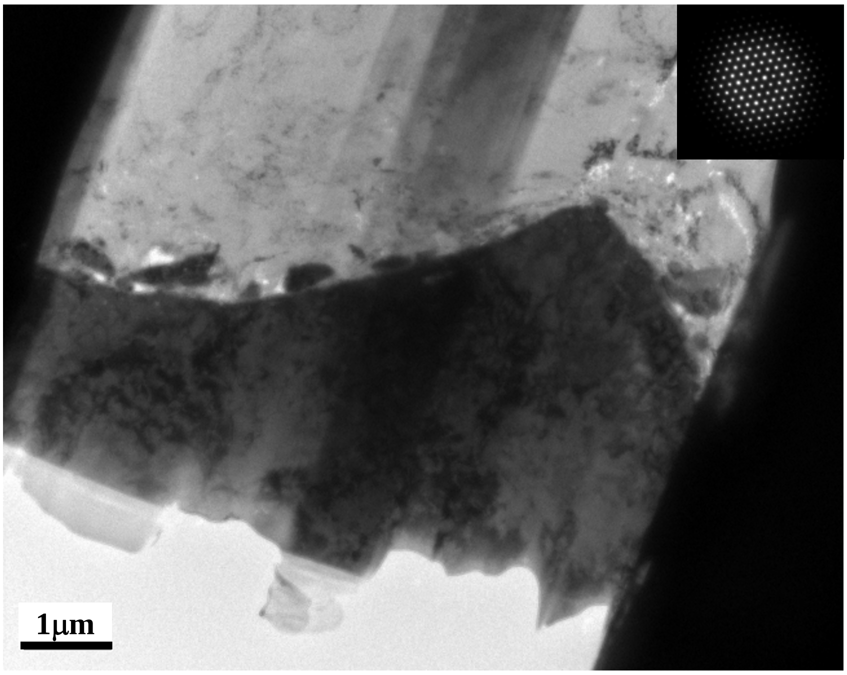

Fig. 6-7. Single crystal Mn inoculant particles added in Mg matrix, incident beam // $[001]_{Mn}$.

the added Mn particle and Mg matrix was further analyzed with STEM-EDS line scanning, as shown in Fig. 6-8(g). The results showed that slight inter-diffusion of elements was limited within a layer of 60 nm between the Mg matrix and the Mn particle (Fig. 6-8(g)). Chemical reaction between the added Mn particles and alloying elements in matrix essentially did not happen, since the element distribution sharply changed and no stable composition was formed across the interface between the added Mn particle and Mg matrix.

The maximum solubility of Mn in Mg at the peritectic temperature of 700°C is 1.0 ~ 1.6 at.% Mn. In comparison, the solid solubility of Mg in Mn is negligible [51]. Therefore, these added inoculant Mn particles could be expected to slightly dissolve into the molten pool to become solute. It was reported that when the cooling rate was as low as 1.2°C/min, the resulting constitutional supercooling produced by solute zirconium in Mg alloy was measured to be less than 2.01°C [167]. The cooling rate could reach 1.4×10^5°C/S during conventional resistance

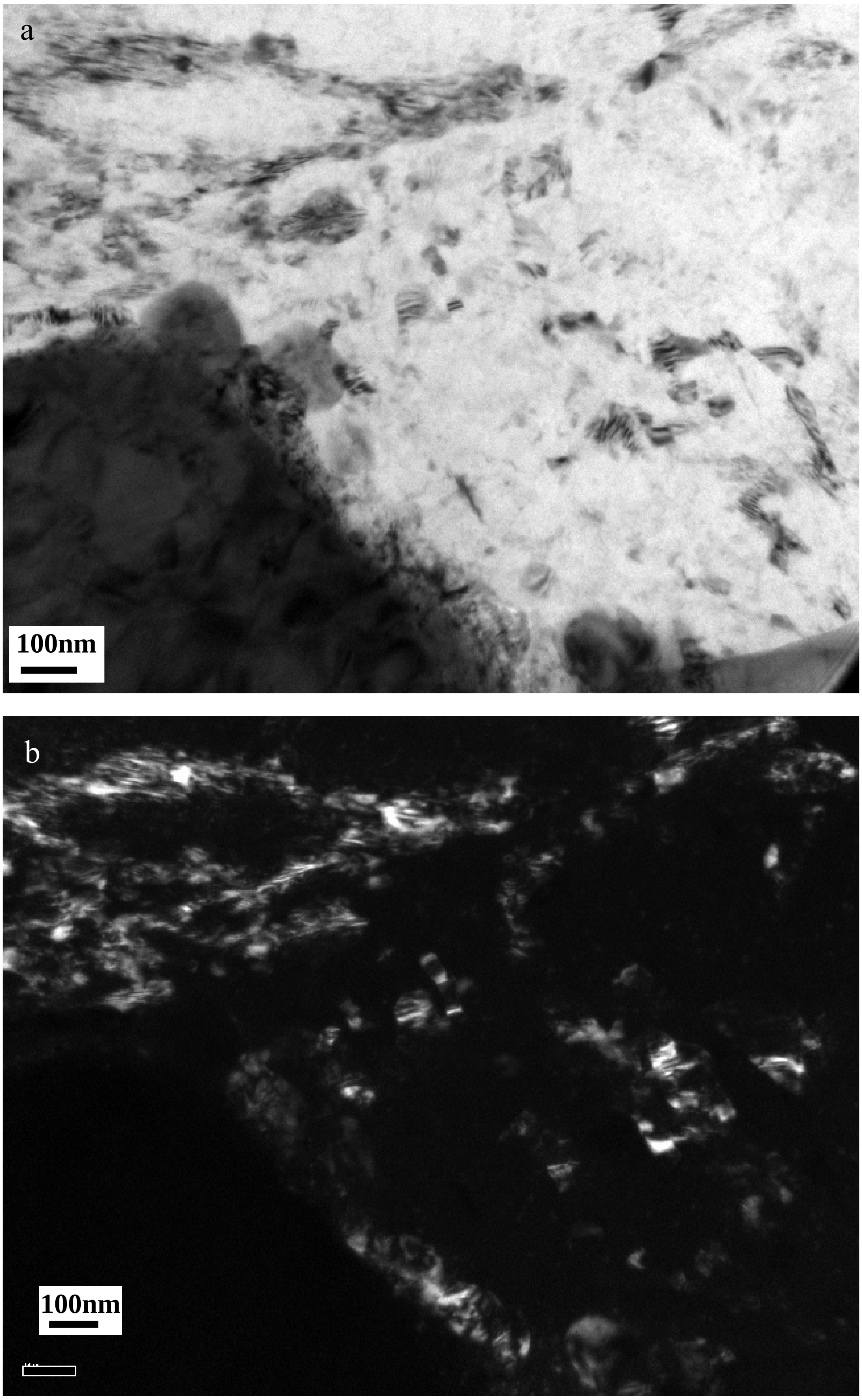
a
100nm
b
100nm

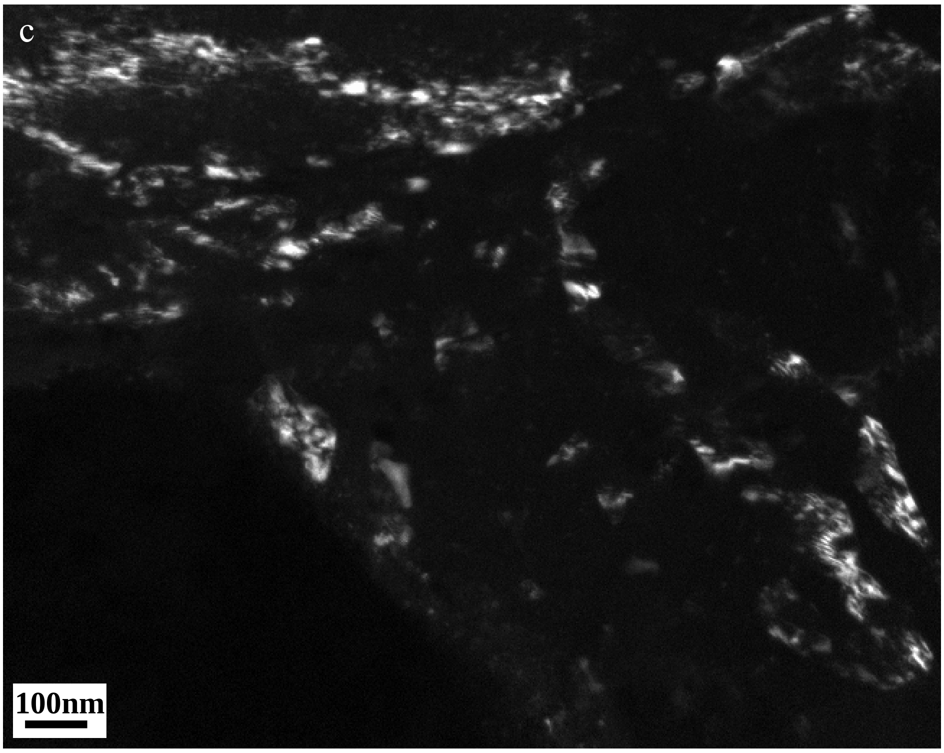
c
100nm

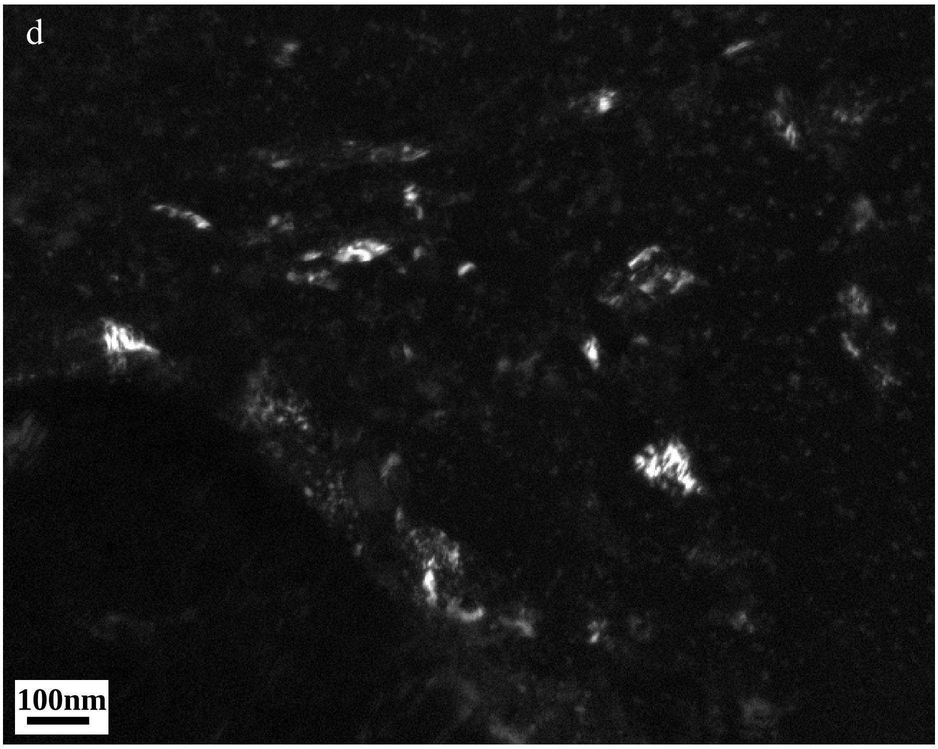
d
100nm

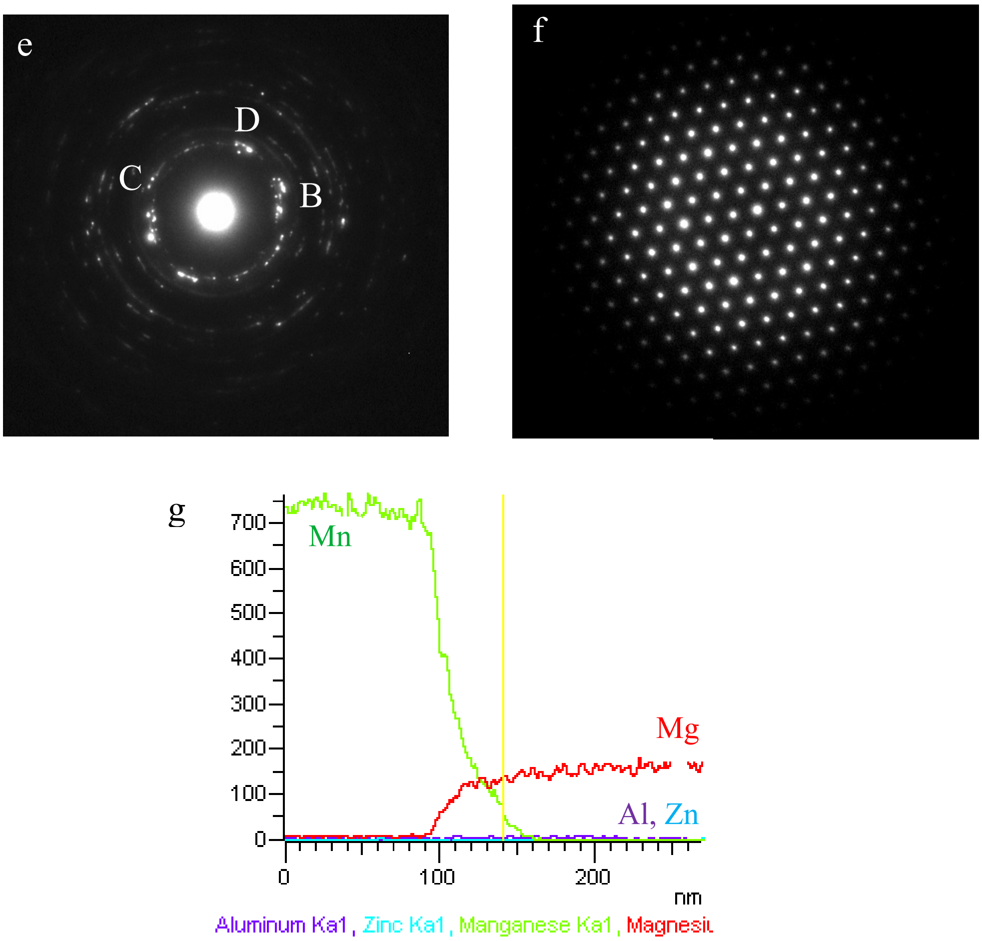

Fig. 6-8. The interface between the added Mn and Mg Matrix, incident beam // $[111]_{Mn}$. (*a*) bright field image, (*b*), (*c*), (*d*) dark field images of nano grains in the vicinity of the interface of Mg matrix corresponding to B, C, D spots in (*e*) selected-area diffraction pattern (SADP) of Mg matrix, (*f*) SADP of Mg matrix, (*g*) STEM line scanning of element distribution across the interface.

spot welding of AZ31 Mg alloy based on our following experimental results. This very high cooling rate leads to a very rapid solidification process during welding. The supercooling produced by constitutional element microsegregation; thus, is much lower than the possible value of thermal supercooling during conventional resistance spot welding in this work.

Figs. 6-9(a) through 6-9(e) show the interfacial character between Mg matrix and the added Mn particle and the corresponding SADPs. The combined SADPs of Mg and Mn and their

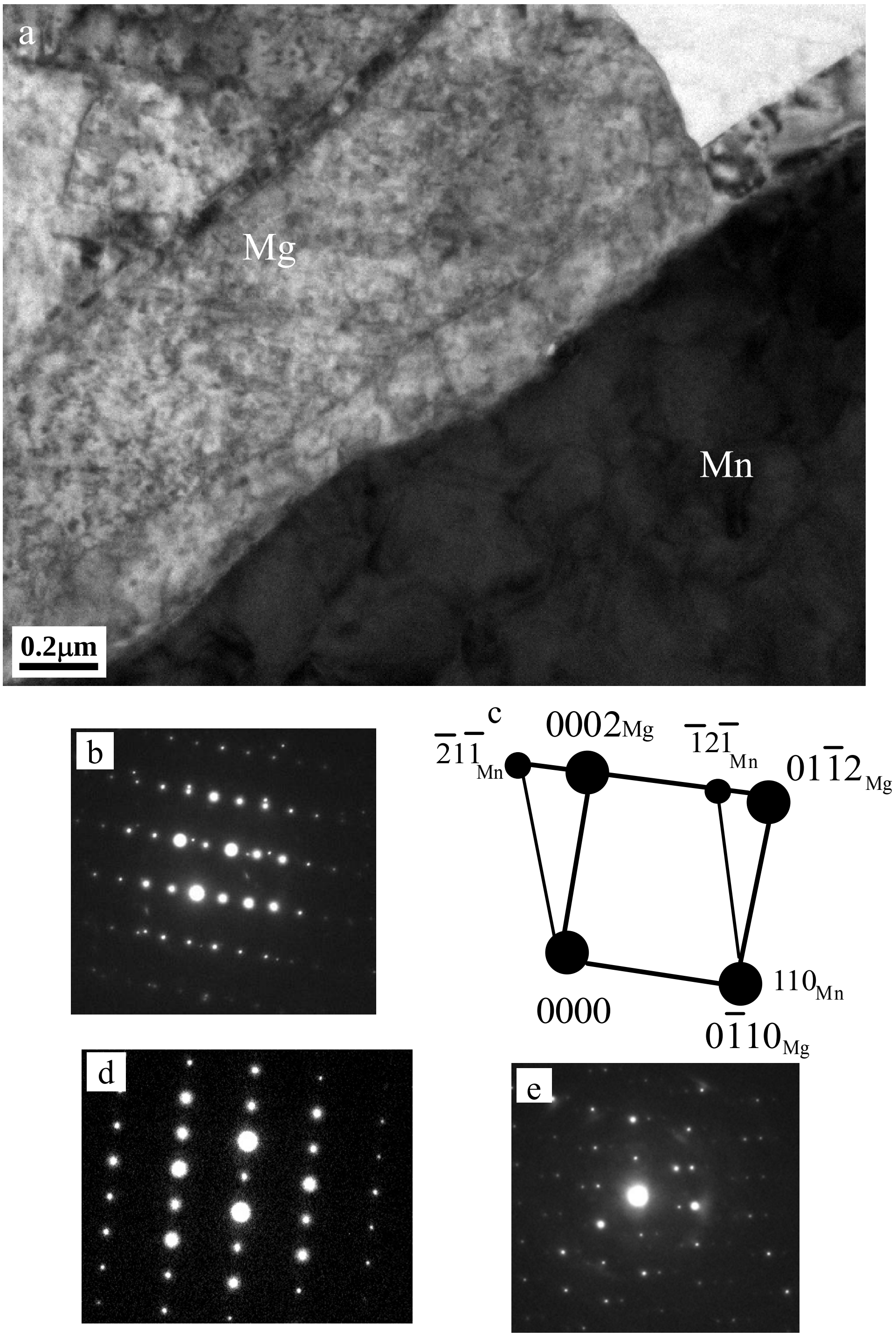

Fig. 6-9. The interface between the added Mn particles and Mg Matrix. (*a*) TEM image, (*b*) selected-area diffraction pattern (SADP) taken from both α-Mg matrix and the added Mn particles, incident beam || $[2\bar{1}\bar{1}0]_{Mg}$, (*c*) schematic diagram of (b) SAD pattern indexed in Mg $[2\bar{1}\bar{1}0]$ zone direction, (*d*) the corresponding SADP of Mg matrix, incident beam ||$[2\bar{1}\bar{1}0]_{Mg}$, (*e*) the corresponding SADP of the added Mn particles, incident beam || $[\bar{1}13]_{Mn}$.

indexing are illustrated in Figs. 6-9(b) and 6-9(c). The SADP of Mg and Mn is shown in Fig. 6-9(d) and (e), separately. When the incident beam was parallel to the $[2\bar{1}\bar{1}0]$ zone axis of the Mg matrix (Fig. 6-9(b) and (d)), the surface of the single crystal Mn particle was perpendicular to $[\bar{1}13]$ (Fig. 6-9(b) and (e)). Therefore, the orientation relationship between the added Mn and the Mg matrix was determined to be $[2\bar{1}\bar{1}0]_{Mg} \parallel [\bar{2}26]_{Mn}$. Fig. 6-10 shows a HR-TEM image of an interface between the added Mn particle and Mg matrix, when the incident beam

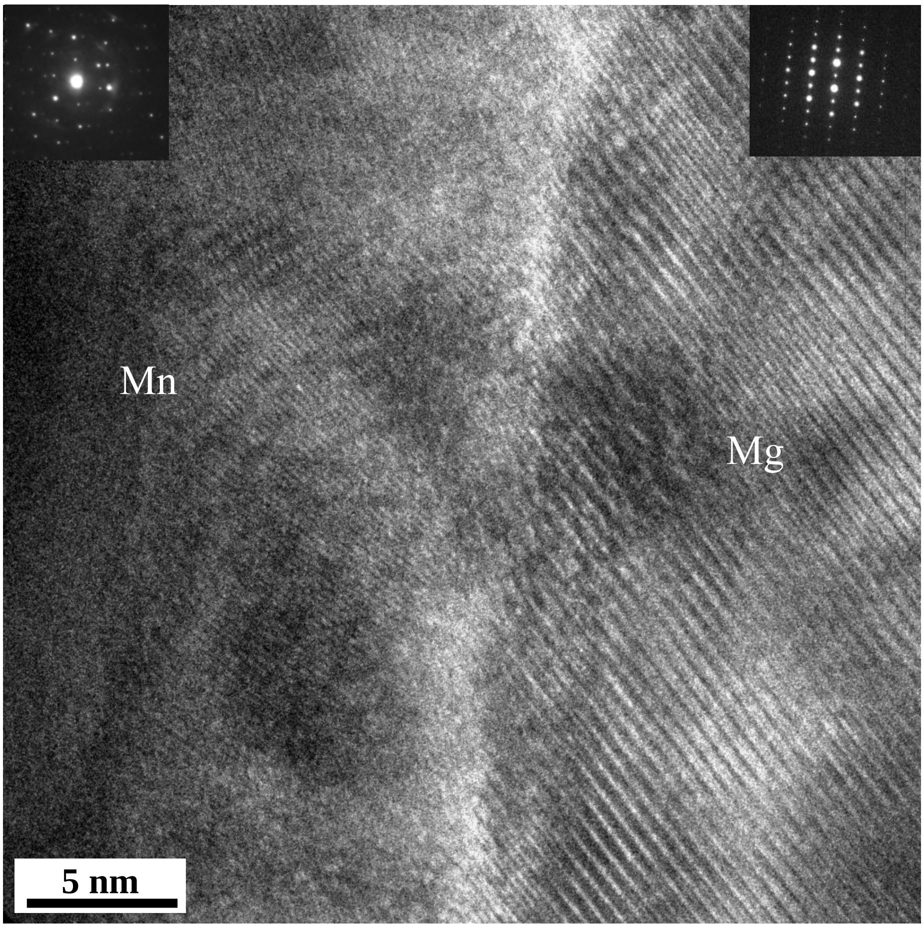

Fig. 6-10. HR-TEM image of the interface between the added Mn and Mg matrix, incident beam || $[2\bar{1}\bar{1}0]_{Mg}$.

was parallel to the $[2\bar{1}\bar{1}0]$ zone axis of the Mg matrix. The lattice matching did not display on the interface, even though there remains a well-defined crystallographic orientation relationship between the added Mn particle and Mg matrix.

Based on the TEM and HRTEM examinations, it can be concluded that there exist well-defined crystallographic orientation relationships between the added three inoculant particles and α-Mg matrix. However, the lattice matching was not always observed on the interface. This could be attributed to the following reasons: (1) the potential coherent or semi-coherent lattice matching between the inoculant and the nucleus could be broken as the nucleus grows to be larger than the critical size, even though this matching could exist in the initial stage of nucleation; (2) a high residual stress could be produced during cutting of the interface by FIB leading to poor quality HR-TEM images to present lattice matching, since the thinning of Mg matrix is much faster than that of Ti, Al_8Mn_5 and Mn particles.

6.2.4. Effect of Cooling Rate on Heterogeneous Nucleation and Resulting Microstructure

The temperature variation as a function of time was measured in the fusion zone of AZ31 Mg alloy welded with the WP1 procedure at different locations, which is shown in the inserted picture on the upper-right corner of the figure, as shown in Fig. 6-11. Double linear cooling curves are displayed. The cooling rate of the liquid phase (left side), which is inferred from the slope of line, was much higher than that of the solid phase (right-down part in Fig. 6-11). Further examination revealed that the liquid phase in the fusion zone could be supercooled to a temperature as low as 483~535°C, which are the apparent nucleation temperatures, T_N, depending on the locations during cooling at the WP1 welding condition. This is 104 to 125°C below the equilibrium melting temperature of the α-Mg phase in AZ31 Mg alloy, T_M, which is about 639°C in the binary Mg-Al phase diagram, when the concentration of Al is 3.0% [51]. The supercooling of liquid phase, ΔT, from 104 to 125°C, which equals the difference of equilibrium melting temperature, T_M, and nucleation temperature, T_N, i.e. $\Delta T = T_M - T_N$, is obtained from the temperature-time profile in the WP1 welding procedure. A tiny peak of temperature curve was produced by recalescence due to the release of latent heat of fusion during solidification, as indicated by an arrow in Fig. 6-11.

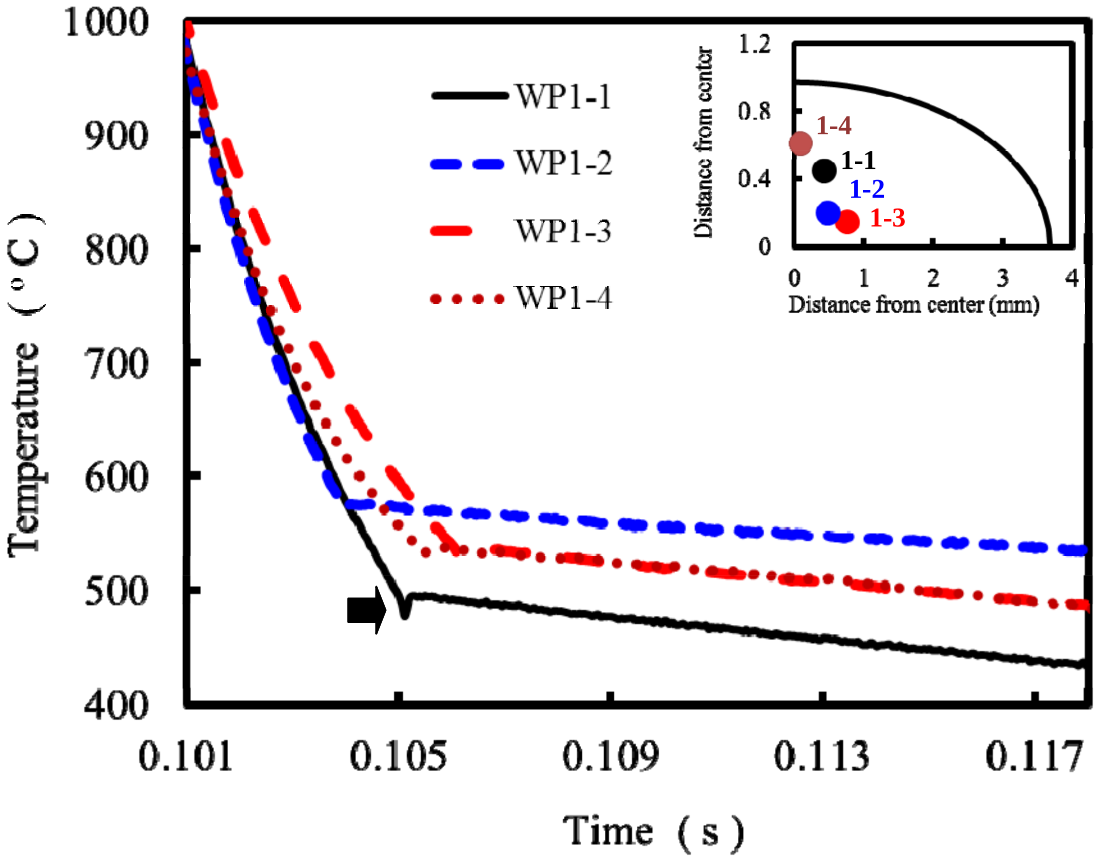

Fig. 6-11. Temperature variation curve as a function of time in AZ 31 resistance spot welds under WP1 at different locations.

The cooling curves of AZ31 welds under different welding procedures from the WP1 to the WP5 at the similar location with WP1-1 in Fig. 6-11 were measured and compared, as shown in Fig. 6-12. The corresponding cooling rate and supercooling level, ΔT, were calculated, as tabulated in Table 6-2. It was found that the cooling rate of the liquid-phase dramatically dropped from 141760°C/S in the WP1 to 1577°C/S in the WP5. The nucleation temperature, T_{N}, changed from 483°C to 639°C depending on the welding procedure and nucleation location. The total supercooling degree, ΔT, dramatically decreased from 120°C in the WP1 to near 0°C in the WP5 with the decrease of the cooling rate (Table 6-2).

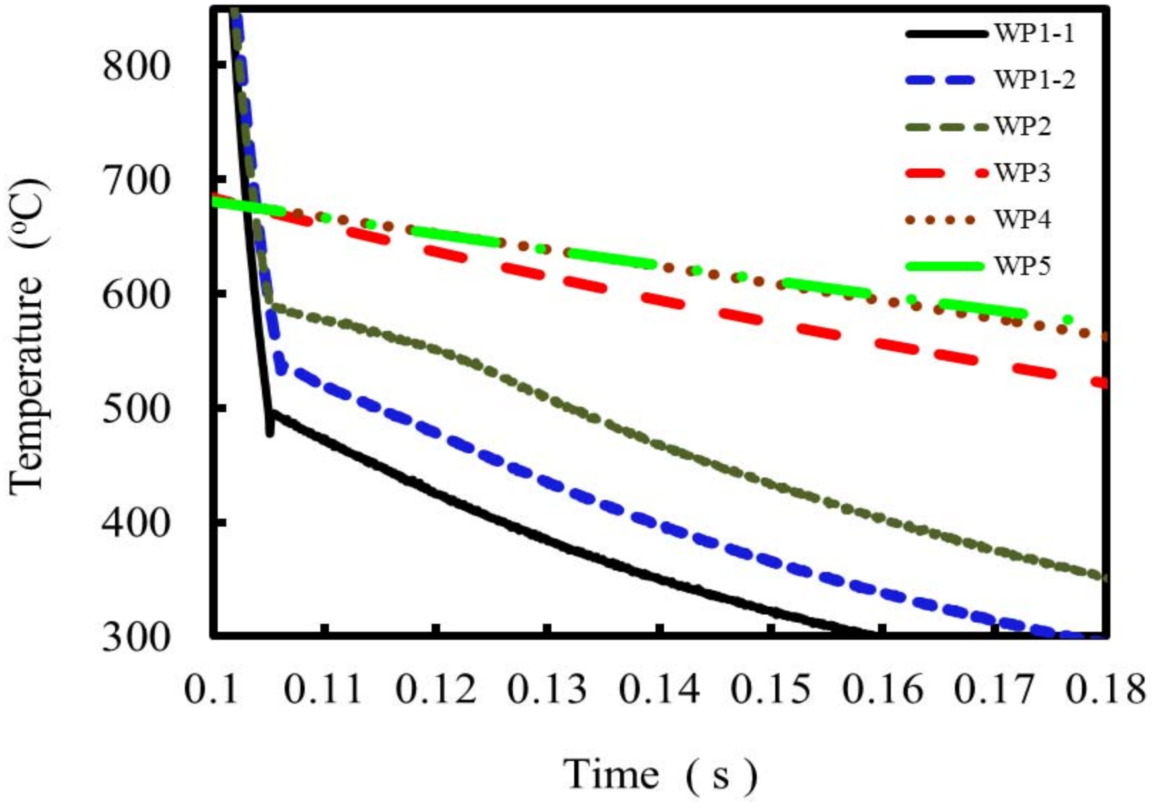

Fig. 6-12. A comparison of cooling rates in AZ 31 resistance spot welds under different welding procedures.

A CET will occur if the equiaxed grains are sufficient in size and number to arrest columnar grain growth in the front of the solid-liquid interface, and the diameter of equiaxed grains in the central areas of the fusion zone will decrease, as the heterogeneous nucleation rate of equiaxed grains increases due to the dramatic increase of cooling rate. Therefore, the relationship between the CDZ and the cooling rate was established, and could be selected as a parameter to evaluate the efficiency of grain refinement in the fusion zone of AZ 31 Mg alloy resistance spot welds due to an addition of inoculant particles under different welding procedures.

Table 6-2. Average Cooling Rate and Supercooling Degree for Each Welding Procedure

Welding Process	Cooling Rate (°C/S)		Supercooling Degree (°C)
	Liquid Phase	Solid Phase	
WP1	141760	4795	120
WP2	89014	4481	52
WP3	2067	1246	0
WP4	1632	1603	0
WP5	1577	1077	0

The microstructures in AZ31 alloy welds with an addition of Al_8Mn_5 and Mn inoculants at WP3 welding procedure are shown in Fig. 6-13(a) and (b), respectively. It was found that the length of CDZ in the weld with an addition of Al_8Mn_5 was shorter than that with Mn addition, where a fully columnar dendritic structure was produced through the fusion zone. This indicates that the inoculant, Al_8Mn_5, with the smaller lattice disregistry with Mg matrix has the higher potency than Mn with the larger disregistry, as the cooling rate declines to 2067°C/S in the WP3.

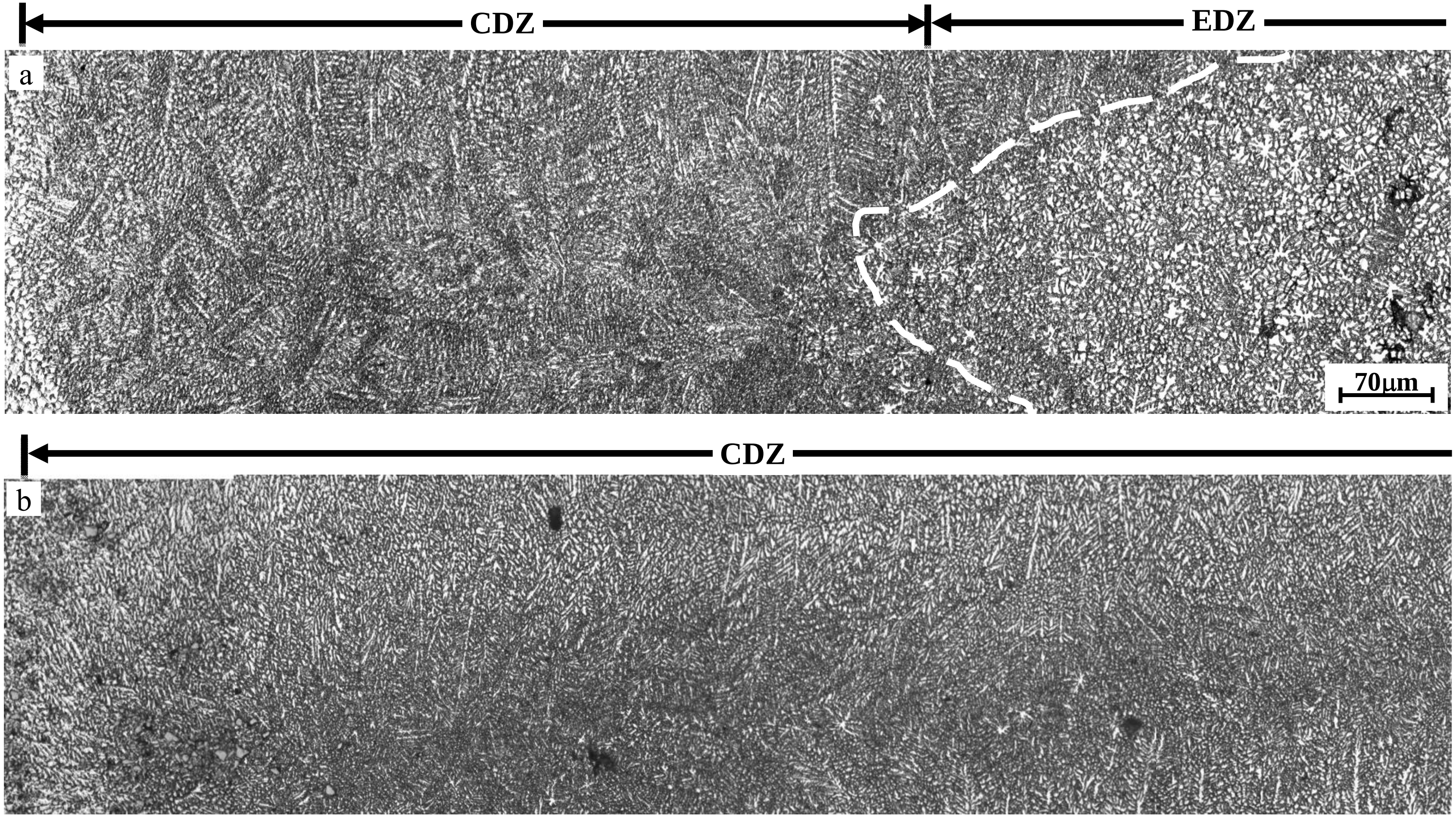

Fig. 6-13. A comparison of grain refinement efficiency between Al_8Mn_5 and Mn inoculants under WP3 welding: (*a*) added Al_8Mn_5 and (*b*) added Mn.

The length of CDZ as a function of cooling rate in AZ31 Mg alloy welded with the addition of different inoculants under different welding procedures is illustrated in Fig. 6-14. The potency of inoculants to refine microstructure under different cooling rates or welding procedures is summarized in Table 6-3. It is demonstrated that the potency of inoculants decreases with increasing values of the lattice disregistry in the WP3, WP4, and WP5, where the cooling rate or the total supercooling degree, ΔT, is low. This implies that the lattice disregistry has an obvious effect on heterogeneous nucleation behaviour at a low ΔT condition. The most potent inoculant is the particle which provides the best lattice matching between the inoculant particle and the Mg matrix. The higher the crystallographic lattice disregistry, the longer the length of CDZ was found, when the total supercooling degree, ΔT, or the cooling rate was low in the WP3, WP4, and WP5 welding processes (Fig. 6-14). However, all inoculants are potent, and the effect of crystallographic lattice disregistry on heterogeneous nucleation could be ignored, when the cooling rate or total supercooling degree, ΔT, was high enough in the WP1 and WP2 which had a high total supercooling level, ΔT, of 104 to 125°C (Fig. 6-14 and Table 6-3).

6.3. Discussion

6.3.1. Effect Factors of Heterogeneous Nucleation

It is generally accepted that an important condition for an inoculant particle to be a potent heterogeneous nucleation site is the formation of a low energy interface between the inoculant particles and the nucleated phase [139,143-145,204,205]. In terms of crystallographic criteria, a coherent or semi-coherent interface with a small lattice disregistry has a small interfacial energy, and thus is an effective site for heterogeneous nucleation. The critical interatomic spacing disregistry along the matching directions and the critical interplanar spacing

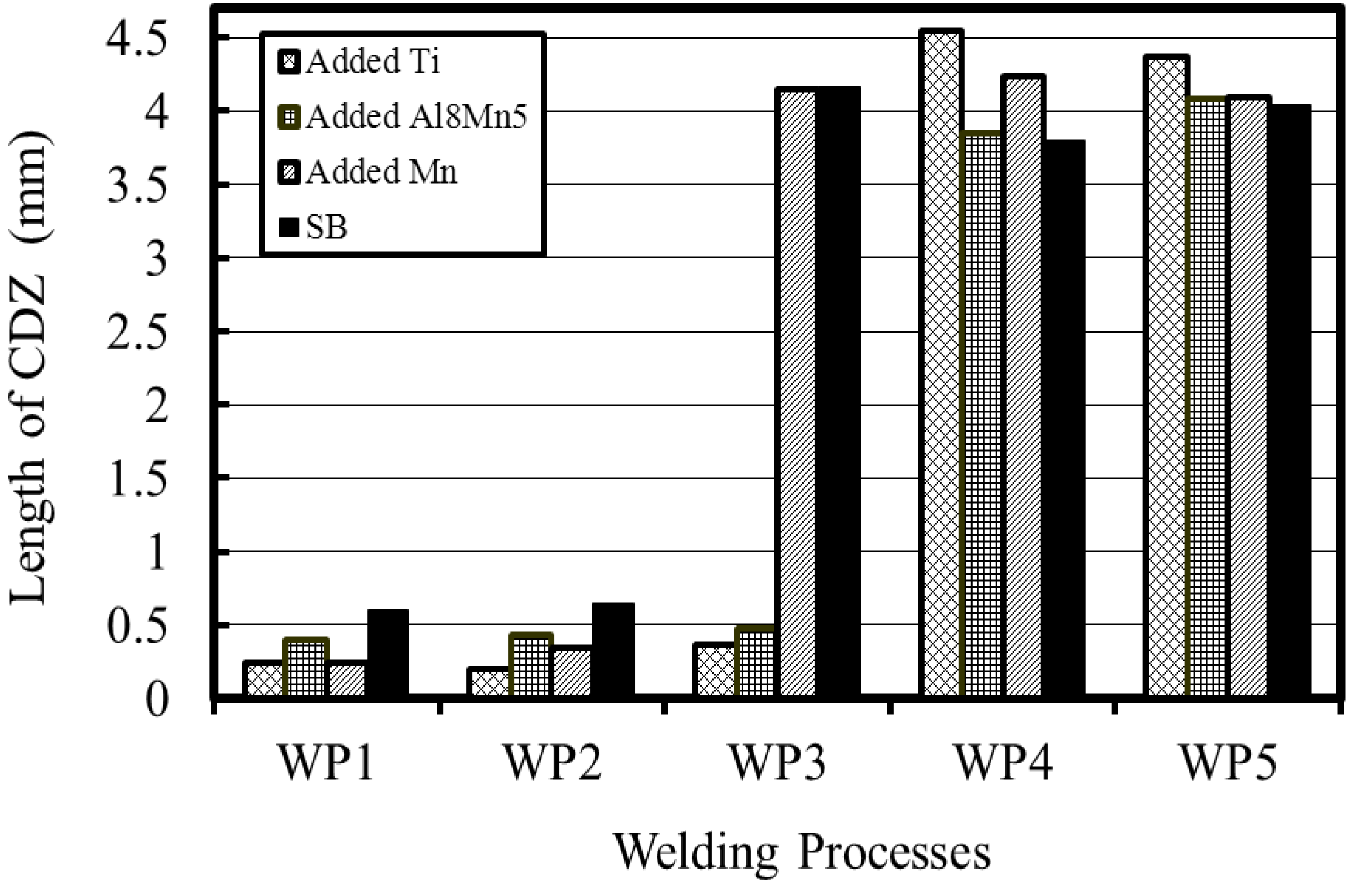

Fig. 6-14. The effect of cooling rate and inoculants on grain refinement during solidification of AZ31 welds.

Table 6-3. A Comparison of Refinement Efficiency for Different Inoculants in AZ31 Mg Alloy Resistance Spot Welds under Different Cooling Rates

Added Inoculants	Minimum Interplanar Disregistry, %	Minimum Interatomic Disregistry, %	Refinement Efficiency				
			WP1	WP2	WP3	WP4	WP5
Ti	2	4	Excellent	Good	Good	Good	No
Al_8Mn_5	7.4	17.8	Excellent	Good	Good	No	No
Mn	10.5	20.1	Excellent	Good	No	No	No

disregistry between matching planes have been used to predict the effectiveness of grain refiners according to the edge-to-edge crystallographic matching model [143-145,190-192,204]. Extensive TEM examinations have showed the existence of good orientation relationship and some lattice matching between the inoculant particles, Ti, Al_8Mn_5, Mn and the Mg matrix in this work. However, some inoculants, which do not have a good theoretical crystallographic matching with Mg, have been experimentally observed by other investigators to refine grain size of Mg alloys [183,208,209]. For example, ceramic inoculants, SiC [208], Al_4C_3 [183], TiB_2 [209], and TiC [209] were reported to be potent refiners during solidification of Mg-alloys castings. This implies that other factors could also promote heterogeneous nucleation when the inoculant particles have a large lattice disregistry or a high interfacial energy with the Mg matrix. Even though the lattice disregistry limits the efficiency of inoculant particles, they can still become the nucleation sites and promote the heterogeneous nucleation and the grain refinement if the cooling rate of liquid phase is high enough to achieve a high total supercooling degree, ΔT, during welding.

6.3.2. Heterogeneous Nucleation Mechanism during Resistance Spot Welding

It has been accepted that solidification morphology in any given alloy depends on the ratio of G/R and solidification size depends on the GR, where G is the thermal gradient and R the solidification growth velocity [29,30,31]. The relationship between the cooling rate, dT/dt, and G and R can be described in equation (6-2) [29]:

$$dT/dt = -GR. \tag{6-2}$$

Some experimental results have shown that a faster cooling rate gave a finer grain size in AZ31 Mg alloy casting [118]. Gunther *et al.* [118] observed that a homogeneous and fine microstructure was achieved in the aluminum-containing Mg alloys during squeeze casting, which had a fast cooling rate. However, coarse grains were formed in the case of slow cooling rates, *e.g.* continuous casting [118]. This is consistent with our results observed in AZ 31 Mg alloy welds. The high cooling rate promoted the heterogeneous nucleation and the grain refinement in the fusion zone of Mg alloys.

Different mechanisms of grain refinement could be activated in different ranges of cooling rates during solidification. The detailed mechanisms have been summarized in several review papers [86,202,210]. For resistance spot welding with the WP3, WP4, and WP5 welding procedures, which have a low cooling rate and a small supercooling, ΔT, solute diffusion occurs under local equilibrium or near-equilibrium conditions, and the solute concentration field is governed by the mass transport equation [70,134,101,102,200,201]. Consequently, the constitutional supercooling driving heterogeneous nucleation becomes the dominant nucleation mechanism [70,134,101,102,200,201]. The columnar grains grow and trap the equiaxed dendritic nuclei in the fusion zone before equiaxed dendrites could nucleate and grow to a critical size. Therefore, the long CDZ is formed.

Under rapid solidification conditions in the WP1 and WP2 procedures, the solute accumulation ahead of the solid/liquid interface decreases due to the increase of solute partition coefficient [114]. Consequently, the effect of constitutional supercooling, ΔT_c, on heterogeneous nucleation and growth gradually decreases. The kinetic supercooling, ΔT_k, and constitutional supercooling, ΔT_c, are minimal and can be ignored in this solidification condition [114,115,202]. On the other hand, the temperature field is far from local equilibrium, and non-equilibrium effect of temperature field at the interface of liquid/solid becomes significant. As a result, solute diffusion in the front of dendrite tip is replaced by thermal diffusion to predominantly control dendrite nucleation and growth, which indicates a transition from the equilibrium solidification controlled by the solutal gradient to a thermally controlled nucleation and growth [86,199,210]. The effect of thermal supercooling, ΔT_t, on heterogeneous nucleation is dominant. As the cooling rate or thermal supercooling increases, equiaxed grains could sufficiently nucleate and grow before the columnar grains can trap them, resulting in the formation of the short CDZ and the refined equiaxed grains in the WP1 and WP2 procedures.

6.3.3. The Potency of Inoculant Particles as Nucleation Inoculants

Al_8Mn_5 intermetallic particles are usually present in most commercial AZ31, AZ61, and AZ91 Mg alloys [50,128,182,211,212]. There has been considerable debate as to whether Al_8Mn_5 particles can act as potent nucleation sites for α-Mg during the solidification of Mg–Al based alloys. Byun *et al.* [128] investigated the effect of different Mn addition levels on the microstructure of the AZ91 alloy, and suggested that $Al_8(Mn,Fe)_5$ particles acted as effective nucleation sites. Laser *et al.* [50] reported grain refinement by Al_8Mn_5 particles in AZ31 alloys even though Al_8Mn_5 has a rather high atomic mismatch energy against α-Mg. Kim *et al.* [182] observed that $Al_8(Mn, Fe)_5$ served as nucleation sites for α-Mg through a duplex nucleation mechanism, in which aluminum carbides enhance the nucleation of $Al_8(Mn, Fe)_5$ particles, and $Al_8(Mn, Fe)_5$ particles in turn promote nucleation of the α-Mg phase.

Zhang *et al.* [143] concluded that Al_8Mn_5 is unlikely to be a potent grain refiner for Mg–Al based alloys due to their high crystallographic disregistry based on edge-to-edge crystallographic matching model. Fan *et al.* [211] experimentally observed that the grain size did not show any notable change in two AZ91D alloys with different Mn concentrations, i.e. 0.02 wt.% and 0.22 wt.%, respectively. After the extensive HR-TEM examination on the Al_8Mn_5/α-Mg interfaces, Wang *et al.* [212] found that there was not any crystallographic orientation relationship between the Al_8Mn_5 and α-Mg crystals, and thus concluded that Al_8Mn_5 particles were unlikely to act as effective nucleation sites for the α-Mg during solidification of Mg-Al based alloys.

It is worth noting that there are two common features of this prior work where the grain refinement did not take place due to Al_8Mn_5 inoculant in the Al-bearing Mg alloys: (1) the peak melting temperature was from 640-675°C, which was too low, in those experiments [211,212], (2) the rate of cooling/solidification was as low as 3.5 K/s during casting [211,212]. In those cases, the supercooling, ΔT, was not high enough to promote heterogeneous nucleation, when the interfacial energy was high due to a large crystallographic disregistry between Al_8Mn_5 inoculant particles and Mg matrix. Therefore, the interfacial energy could be expected to play a critical role in controlling and refining the solidification microstructure. In comparison, in those processes with a relatively high cooling rate [198], the supercooling degree, ΔT, is high enough to overcome the interfacial barrier of inoculant particle to promote the heterogeneous nucleation, even though lattice disregistry could restrict the efficiency of inoculant particles as heterogeneous nucleation sites.

A nano-grain area was observed in the vicinity of the interface of AZ31 Mg matrix when the Mn inoculant particles were added. The formation of nano-grained structure needs a high nucleation rate and a low growth rate [213]. The high interfacial energy between Mn inoculant and Mg matrix facilitates the increase of supercooling of liquid metals and alloys by avoiding heterogeneous nucleation, and thus, increase the heterogeneous nucleation rate. As a result, ultrafine grains were formed during rapid solidification. Meanwhile, the added Mn inoculant particles was observed to be single crystal (Fig. 6-7), which provided the larger crystallographic face with a low interfacial energy to satisfy the critical size of heterogeneous nucleation of Mg matrix in comparison with the polycrystal inoculant particle [198]. As a result, the nucleation rate of Mg matrix is high enough to facilitate the formation of nano-grains at the beginning of solidification.

6.4. Summary

1. Microstructural refinement was achieved in the fusion zone of AZ31 magnesium alloy during resistance spot welding by adding one of three inoculants, Ti, Al_8Mn_5, and Mn. The length of the columnar dendritic zone in the vicinity of the fusion boundary was restricted and the diameter of equiaxed dendritic grains in the central areas of fusion zone was reduced.

2. HR-TEM analysis indicated the existence of crystallographic orientation relationships along close-packed or near close-packed planes and directions between the α-Mg matrix and the added inoculant particles, Ti and Mn.
3. The inoculant potency is high for the Ti inoculant, medium for the Al_8Mn_5, but low for the Mn, when the cooling rate is low. This order in the decrease of grain refinement efficiency is inversely proportional with the order of crystallographic lattice disregistry between inoculants and matrix, which is calculated based on a crystallographic matching model. This implies that the lattice disregistry determines the potency of inoculants at low cooling rates.
4. When the cooling rate is high, the thermal condition in the liquid pool are more severe so that a large supercooling, ΔT, could be achieved, leading to a high driving force for heterogeneous nucleation to promote the grain refinement. As a result, all three inoculants Ti, Al_8Mn_5, and Mn, could efficiently refine the grain size of welds, although they have different degrees of lattice disregistries with the Mg matrix.

7. Summary, Conclusions, and Further Work

7.1. Summary and Conclusions

7.1.1. Dependence of Fusion Zone Microstructure and Fatigue Behaviour of Welds on Second-phase Particles

Four distinct regions could be distinguished in the typical microstructure of AZ31 Mg alloy resistance spot welds, *i.e.* base metal (BM), heat-affected zone (HAZ), columnar dendritic zone (CDZ), and equiaxed dendritic zone (EDZ). Columnar dendritic grains were well-developed in the fusion zone of SB alloy welds, while they were restricted within a narrow region near the fusion boundary by an earlier transition from columnar to equiaxed structure in the SA alloy welds.

Three sizes of second-phase particles, which were formed during manufacturing, were observed in the as-received SA and SB alloys. Coarse Al_8Mn_5 particles of 4-10 μm in length were only formed in the SA alloys. Submicron-sized Al_8Mn_5 particles of 0.09-0.4 μm in length and nano-sized $Mg_{17}Al_{12}$ were observed to be present in both SA and SB alloys. All of these Al_8Mn_5 and $Mg_{17}Al_{12}$ intermetallic particles were pre-existing from the sheet manufacturing process and were not apparently changed significantly by the transient melting during weld nugget formation.

The refined microstructure in the fusion zone of the SA alloy could be attributed to the preexisting coarse second-phase particles of Al_8Mn_5 which played a role of inoculants to promote heterogeneous nucleation on their surface during solidification. The coarser the particles, the more efficient the nucleation of α-Mg was found to be.

Typical fatigued dislocation configurations in the fusion zone of the SA welds consisted of elongated dislocation cells. In comparison, elongated parallel dislocation lines and parallelogram dislocation cells were observed in the fatigued SB welds. Cyclic plastic deformation mode in the AZ31 welds evolved from {0002} single basal slip in the SB alloy welds to $1/3\langle 11\bar{2}3\rangle$ pyramidal combined with {0002} basal slips in the SA alloy welds.

AZ31 SA resistance spot welds with the refined fusion microstructure had a longer fatigue life than that of AZ31 SB welds with the coarse microstructure, when the interfacial failure across fusion zone took place. Pyramidal multiple slips and twinning were simultaneously activated in the finer-grained SA welds probably due to the lower stress concentrations and the high critical shear stress for twinning. This led to an increase of the amount and dispersion of slip systems in the SA welds, thus a longer fatigue life than that of the SB welds.

7.1.2. Grain Refinement and Mechanical Property Improvement due to the Addition of Ti Inoculant

The columnar dendritic zone (CDZ) was significantly suppressed to within a width of 320 μm, and a more randomly oriented dendritic structure with short primary arms replaced the well-developed primary arms in the vicinity of the fusion boundaries of the as-received AZ31 Mg alloy SB welds due to the addition of Ti powders as inoculant particles.

The coarse equiaxed dendrites in the central area of the welds without the addition of Ti were efficiently refined by adding titanium powders into the molten pool. The average diameter of the flower-like equiaxed dendrites in the central area of fusion zone with Ti addition was much smaller than that without the addition of Ti. It was approximately 65μm in AZ31 without the addition of Ti, whereas only about 20μm with the addition of Ti.

The ultimate tension-shear load of the AZ31 alloy welded at 26 kA with an addition of Ti increased by 38 percent from 4076 N to 5619 N in comparison with the welds without adding Ti. Meanwhile, the displacement rose by 28 percent from 1.09 to 1.40. When the welding current increased to 30 kA, the ultimate tension-shear load increased by 16 percent from 4796 N to 5562 N, and the displacement increased by 17 percent from 1.12 to 1.31.

Ti inoculant could provide potent heterogeneous nucleation sites for the Mg matrix due to a good crystallographic orientation matching between some grains of the added Ti particles and Mg matrix. The orientation relationship between those Ti grains and AZ 31 Mg alloy matrix was determined to be $[01\bar{1}0]_{Mg} // [1\bar{2}1\bar{3}]_{Ti}$ and $(0002)_{Mg} // (10\bar{1}0)_{Ti}$.

7.1.3. Grain Refinement Mechanism due to the Addition of Inoculants

HR-TEM analysis indicated the existence of crystallographic orientation relationships along close-packed or near close-packed planes and directions between the α-Mg matrix and the added inoculant particles, Ti and Mn. Both well-defined orientation relationship and well lattice matching were observed on the interface between the Al_8Mn_5 inoculant and α-Mg matrix.

The inoculant potency was high for the Ti inoculant, medium for the Al_8Mn_5, but low for the Mn, when the cooling rate was low. This order in the decrease of grain refinement efficiency was inversely proportional with the order of crystallographic lattice disregistry between inoculants and matrix, which is calculated based on a crystallographic matching model. This implies that the lattice disregistry determines the potency of inoculants at low cooling rates.

When the cooling rate is high, the thermal conditions in the liquid pool are more severe so that a large supercooling, ΔT, could be achieved, leading to a high driving force for heterogeneous nucleation to promote the grain refinement. As a result, all three inoculants Ti, Al_8Mn_5, and Mn, could efficiently refine the grain size of welds, although they have different degrees of lattice disregistries with the Mg matrix.

7.2. Future Work

7.2.1. Microstructure Improvement in the Heat-affected Zone

Both mechanical strength and ductility of AZ 31 alloy welds have been increased by more than 20% through introducing inoculants into the fusion zone to refine microstructure. As a result, cracks begin to initiate and grow in the heat-affected zone (HAZ) in the modified AZ 31 Mg alloy welds when they were subjected to monotonic and cyclic loading. Therefore, it is essential to improve the microstructure and mechanical properties of the HAZ so as to further increase the overall mechanical properties of welds by optimizing the welding process or post-welding treatment based on the microstructural examination of the HAZ.

7.2.2. Synergistic Effect of Temperature Field and Second-Phase Particles on Welding Microstructure of AZ31 Magnesium Alloys under Various Welding Techniques

A variety of welding techniques have been employed to join Mg alloys, such as resistance spot welding, laser welding, electron beam welding, friction stir welding, and tungsten inert gas welding. Among these processes, the prediction of microstructure and mechanical properties of welds is critical for the application of each kind of welding technique. It is essential to establish an evolution map of microstructure as a function of temperature field and inoculant particles in the fusion zones of welds in AZ31 Mg alloys so as to predict the microstructural features and mechanical properties of these welds under a variety of welding techniques.

8. Publications

1. **L. Xiao,** R. Liu, S. Esmaeili, Y. Zhou. (2012): Heterogeneous Nucleation on Inoculant Particles in the Fusion Zone of Welds during Non-equilibrium Solidification, *Metall. Mater. Trans.* A, (submitted *Acta Mater.* on Jan.26, 2012).
2. **L. Xiao,** R. Liu, S. Esmaeili, Y. Zhou. (2012): Microstructure Refinement due to the Addition of Titanium Particles in AZ31 Magnesium Alloy Resistance Spot Welds, *Metall. Mater. Trans.* A, 43, 598-609.
3. **L. Xiao**, L. Liu, D.L. Chen, S. Esmaeili, Y. Zhou. (2011): Resistance Spot Weld Fatigue Behavior and Dislocation Substructure in Two Different Heats of AZ31 Magnesium Alloy, *Mater. Sci. Eng.* A, 529, 81-87.
4. **L. Xiao,** R. Liu, Y. Zhou, S. Esmaeili. (2010): Resistance Spot Welded AZ31 Magnesium Alloys, Part I: Dependence of Fusion Zone Microstructures on Second-phase Particles, *Metall. Mater. Trans.* A, 41(6), 1511-1522.
5. L. Liu, **L. Xiao**, J.C. Feng, Y.H. Tian, S. Esmaeili, Y. Zhou. (2011): Bonding of Immiscible Mg and Fe by Coated Nanoscale Fe_2Al_5 Transition Layer. *Scripta Mater.* 65, 982-985.
6. L. Liu, **L. Xiao**, J.C. Feng, Y.H. Tian, S.Q. Zhou, Y. Zhou. (2010): The Mechanisms of Resistance Spot Welding of Magnesium to Steel, *Metall. Mater. Trans.* A, 41(10), 2651-2661.
7. L. Liu, **L. Xiao**, J.C. Feng, Y.H. Tian, S.Q. Zhou, Y. Zhou. (2010): Resistance Spot Welded AZ31 Magnesium Alloys, Part II: Effects of Welding Current on Microstructure and Mechanical Properties, *Metall. Mater. Trans.* A, 41(10), 2642-2650.

Other Publications, which are not related to my thesis

8. W. Chen, Q.Y. Sun, **L. Xiao**, J. Sun. (2012): Deformation-Induced Grain Refinement and Amorphization in Ti-10V-2Fe-3Al Alloy, *Metall. Mater. Trans.* A, 43(1), 316-326.
9. W. Chen, Q.Y. Sun, **L. Xiao**, J. Sun. (2012): Thermal Stability of Bulk Nanocrystalline Ti-10V-2Fe-3Al Alloy, *Mater. Sci. Eng.* A, 526, 223-230.

10. H. Wang, Q.Y. Sun, **L. Xiao**, J. Sun. (2012): Effect of Grain Size on Twinning Behavior in Ti-2Al-2.5Zr Alloy Fatigued at 77K, *Mater. Sci. Eng.* A, (in press).
11. Z.Y. Song, Q.Y. Sun, **L. Xiao**, J. Sun, L.C. Zhang. (2011): Precipitation Behavior and Tensile Property of the Stress-aged Ti–10Mo–8V–1Fe–3.5Al Alloy, *Mater. Sci. Eng.* A, 528, 4111–4114.
12. Q. Sun, Q. Guo, X. Yao, **L. Xiao**, J.R. Greer, J. Sun. (2011): Size Effects in Strength and Plasticity of Single Crystalline Titanium Micro-Pillars with Prismatic Slip Orientation, *Scripta Mater.* 65, 473-476.
13. Q.W. Jiang, **L. Xiao**, X.W. Li. (2011): A Comparison of Temperature-Dependent Compressive Deformation Features of Ultrafine-Grained Ti and Cu Produced by ECAP. *Mater. Sci. Forum***,** 682**,** 41-45.
14. Qian Yu, Zhi Wei Shan, Ju Li, Xiao Xu Huang, **Lin Xiao**, Jun Sun, Evan Ma. (2010): Strong Crystal Size Effect on Deformation Twinning, *Nature,* 463(7279), 335-338.
15. Z.Y. Song, Q.Y. Sun, **L. Xiao**, L. Liu, J. Sun. (2010): Effect of Prestrain and Aging Treatment on Microstructures and Tensile Properties of Ti–10Mo–8V–1Fe–3.5Al Alloy, *Mater. Sci. Eng.* A, 527, 691–698.
16. H. Wang, Q.Y. Sun, **L. Xiao**, J. Sun, P. Ge. (2010): Low-cycle Fatigue Behavior and Deformation Substructure of Ti-2Al-2.5Zr Alloy at 298 and 673K, *Mater. Sci. Eng.* A, 527, 3493-3500.
17. W. Chen, Q.Y. Sun, **L. Xiao**, J. Sun. (2010): Deformation-Induced Microstructure Refinement in Primary Alpha Phase-Containing Ti-10V-2Fe-3Al Alloy, *Mater Sci Eng.* A, 527, 7225-7234.
18. W. Chen, Z.Y. Song, Q.Y. Sun, **L. Xiao**, W.B. She, J. Sun, P. Ge. (2010): Effect of Solution Treatment Temperature on Trigger Stress Induced Martensitic Transformation in Ti-10V-2Fe-3Al Alloy, *J Solid Mech. & Mater. Eng.* 4(8), 1296-1305.
19. **Lin Xiao,** Qian Yu, Qiaoyan Sun, Jun Sun. (2010): Size Effect of Deformation Mode in Micron-sized Ti-5Al Single Crystal Loaded along $[2\bar{1}\bar{1}0]$ and [0001], *Inter J Modern Physics* B**,** 24(15&16), 2466-2471.
20. H. Wang, Y.L. Xu, Q.Y. Sun, **L. Xiao**, J. Sun, P. Geng. (2009): Effect of Grain Size and Testing Temperature on Low Cycle Fatigue Behavior and Plastic Deformation Mode of Ti-2Al-2.5Zr, *Metall. Mater. Trans.* A, 40(11), 2631-2643.
21. Z.Y. Song, Q.Y. Sun, **L. Xiao**, L. Liu, H. Wang, W. Chen, J. Sun. (2009): The Influence of Prior Cold Deformation on Precipitation of Alpha Phase and Variation of Hardness in Ti-10Mo-8V-1Fe-3.5Al during Aging Treatment, *J Mater. Research*, 24, 452-458.
22. X. Yao, Q.Y. Sun, **L. Xiao**, J. Sun. (2009): Effect of Ti_2Cu Precipitates on Mechanical Behavior of Ti-2.5Cu Alloy Subjected to Different Heat Treatments, *J Alloys and Compounds*, 484, 196-202.
23. W. Chen, Z.Y. Song, **L. Xiao**, Q.Y. Sun, J. Sun. (2009): Effect of Prestrain on Microstructure and Mechanical Behavior of Aged Ti-10V-2Fe-3Al Alloy, *J. Mater. Research*, 24(9), 2899-2908.

References

[1] Avedesian, M.M., Baker, H., “ASM Specialty Handbook: Magnesium and Magnesium Alloys,” ASM International, (1999).

[2] Emley, E.F., “Principles of Magnesium Technology,” Pergamon Press, London, (1966).

[3] Suzuki, A., Saddock, N.D., Riester, L., Lara-Curzio, E., Jones, J.W., Pollock, T.M., *Metallurgical and Materials Transactions A*, 38 (2007) 420.

[4] Wu, L., Jain, A., Brown, D.W., Stoica, G.M., Agnew, S.R., Clausen, B., Fielden, D.E., Liaw P.K., *Acta Materialia*, 56 (2008) 688.

[5] Froats, A., Aune, T.K., Hawke, D., Unsworth, W., Hillis, J.E., “Corrosion of Magnesium and Magnesium Alloys,” ASM Handbook, Vol.13, Corrosion, Materials Park, OH 44073-0002, USA, 1987, pp. 740-754.

[6] Hillis, J.E., Shook, S.O., *Automotive Engineering,* 97 (1989) 57.

[7] Holta, O., Westengen, H., Roen, J., *Proceeding of the Third International Magnesium Conference*, Manchester, UK, 10-12 Apr. 1996. pp. 75–87.

[8] Schmid-Fetzer, R., Grobner, J., *Advanced Engineering Materials*, 3 (2001) 947.

[9] Manuel, M., Hector, L.G., Verma, R., Tong, W., *Materials Science and Engineering A*, 418 (2006) 341.

[10] Duly, D., Zhang, W.Z., Audier, M., *Philosophical Magazine,* 71 (1995) 187.

[11] Nie, J.F., Muddle, B.C., *Acta Materialia*, 48 (2000) 1691.

[12] Kim, W.J., Chung, S.W., Chung, C.S., Kum, D., *Acta Materialia*, 49 (2001) 3337.

[13] Liu, L.M., Zhang, Z.D., Song, G., Wang, L., *Metallurgical and Materials Transactions A*, 38 (2007) 649.

[14] Liu, L. M., Song G., Chi, M. S., *Materials Science and Technology,* 21 (2005) 1078.

[15] Coelho, R.S., Kostka, A., Pinto, H., Riekehr, S., Kocak, M., Pyzalla, A.R., *Materials Science and Engineering A,* 485 (2008) 20.

[16] Chi, C.T., Chao, C.G., *Journal of Materials Processing Technology,* 182 (2007) 369.

[17] Wu, S.H., Huang, J.C., Wang, Y.N., *Metallurgical and Materials Transactions A,* 35 (2004) 2455.

[18] Munitz, A., Cotler, C., Shaham, H., Kohn, G., *Welding Journal*, 70 (2000) 202s.

[19] Sun, D.Q., Lang, B., Sun, D.X., Li, J.B., *Materials Science and Engineering A,* 460-461 (2007) 494.

[20] Wang, Y.R., Mo, Z.H., Feng, J.C., Zhang, Z.D., *Science and Technology of Welding and Joining*, 12 (2007) 671.

[21] Commin, L., Dumont, M., Masse, J.E., Barrallier, L., *Acta Materialia*, 57 (2009) 326.

[22] Pareek, M., Polar, A., Rumiche, F., Indacochea, J.E., *Journal of Materials Engineering and Performance*, 16 (2007) 655.

[23] Hongyan Zhang, Jacek Senkara, "Resistance Welding: Fundamentals and Applications", 1st Edition, Taylor & Francis Group, Boca Raton Fl., (2006).

[24] Liu, R., Feng, J. Zhou, Y., *"Resistance Spot Welding of Magnesium Alloys",* Welding and Joining of Magnesium Alloys, Liu, L. Editor, Woodhead Publishing limited, Cambridge, UK, (2010), pp. 351-365.

[25] Chao, Y.J., *Science and Technology of Welding and Joining*, 8 (2003) 133.

[26] Keneath Stearling, "Introduction to the Physical Metallurgy of Welding", 1st Edition, Butterworths & Co (Publishers) Ltd., p. 1, 110-112 (1983).

[27] Zuberove, Z., Kunz, L., Lamark, T.T., Estrin, Y., Janecek, M., *Metallurgical and Materials Transactions A,* 38 (2007) 1934.

[28] Feng, J.C., Wang, Y.R., Zhang, Z.D., *Science and Technology of Welding and Joining*, 11 (2006) 154.

[29] Kou, S., "Welding Metallurgy," 2nd Editor, Wiley Interscience, A John Wiley & Sons, Inc., Hoboken, New Jersey, (2003).

[30] McCartney, D.G., *International Materials Reviews,* 34 (1989) 247.

[31] David, S.A., Vitek, J.M., *International Materials Reviews,* 34 (1989) 213.

[32] Kurz, W., Fisher, D.J., "Fundamentals of Solidification," Aedermannsdorf, Switzerland, Trans. Tech. SA, (1989).

[33] Ganaha, T., Pearce, B.P., Kerr, H.W., *Metallurgical Transactions A,* 11 (1980) 1351.

[34] Pearce, B.P., Kerr, H.W., *Metallurgical Transactions B,* 12 (1981) 479.

[35] Villafuerte, J.C., Pardo, E., Kerr, H.W., *Metallurgical Transactions A,* 21 (1990) 2009.

[36] Kou, S., Le, Y., *Weld Journal,* 65 (1986) 305s.

[37] Kou, S., Le, Y., *Metallurgical Transactions A,* 19 (1988) 1075.

[38] Gerlich, A., Su, P., North, T.H., *Science and Technology of Welding and Joining*, 10 (2005) 647.

[39] Barnett, M.R., Keshavarz, Z., Beer, A.G., Atwell, D., *Acta Materialia*, 52 (2004) 5093.

[40] Ram, G.D.J., Mitra, T.K., Shankar, V., Sundaresan, S., *Journal of Materials Processing Technology,* 142 (2003) 174.

[41] Nishino, N., Kawahara, H., Shimizu, Y., Iwahori H., "Magnesium Alloys and Their Applications, " K.U. Kainer, ed., Wiley-VCH, New York, NY, (2000), pp. 59-64.

[42] Lee, Y.C., Dahle, A.K., StJohn, D.H., *Metallurgical and Materials Transactions A*, 31 (2000) 2895.

[43] Matsuda, F., Nakagawa, H., Nakata, K., Ayani, R., *Transactions of Joining and Welding Research Institute,* 7 (1978) 111.

[44] Koseki, T., Thewlis, G., *Materials Science and Technology,* 21 (2005) 867.

[45] Cao, P., Qian, M., StJohn, D.H., *Scripta Materialia,* 54 (2006) 1853.

[46] Qiu, D., Zhang, M.X., Taylor, J.A., Fu, H.M., Kelly P.M., *Acta Materialia,* 55 (2007) 1863.

[47] Ohno, M., Schmid-Fetzer, R., *Zeitschrift fur Metallkunde*, 96 (2005) 857.

[48] Gertsman, V.Y., Li, J., Xu, S., Thomson, J.P., Sahoo, M., *Metallurgical and Materials Transactions A,* 36 (2005) 1989.

[49] StJohn, D.H., Qian, M., Easton, M.A., Cao, P., Hildebrand, Z., *Metallurgical and Materials Transactions A,* 36 (2005) 1669.

[50] Laser, T., Nurnberg, M.R., Janz, A., Hartig, Ch., Letzig, D., Schmid-Fetzer, R., Bormann, R., *Acta Materialia*, 54 (2006) 3033.

[51] Massalski, T.B., "Binary Alloy Phase Diagrams," ASM International, Metals Park, OH, (1990).

[52] Laser, T., Hartig, Ch., Nurnberg, M.R., Letzig, D., Bormann, R., *Acta Materialia*, 56 (2008) 2791.

[53] Mirkovic, D., Schmid-Fetzer, R., *Metallurgical and Materials Transactions A,* 40 (2009) 958.

[54] Mirkovic, D., Schmid-Fetzer, R., *Metallurgical and Materials Transactions A,* 40 (2009) 974.

[55] Huang, X.H., Suzuki, K., Watazu, A., Shigematsu, I., Saito, N., *Journal of Materials Research,* 23 (2008) 3029.

[56] Robson, J.D., Henry, D.T., Davis, B., *Acta Materialia*, 57 (2009) 2739.

[57] Wang, S.C., Chou, C.P., *Journal of Materials Processing Technology*, 197 (2008) 116.

[58] Liu, C., Pan, F., Wang, W., *Materials Science Forum,* 546-549 (2007) 395.

[59] Wang, R.M., Eliezer, A., Gutman, E.M., *Materials Science and Engineering A,* 355 (2003) 201.

[60] Messner, H.G., Schubert, K., *Zeitschrift fur Metallkunde,* 56 (1965) 523.

[61] Park, S.S., Bae, G.T., Kang, D.H., Jung, I.H., Shind, K.S., Kim, N.J., *Scripta Materialia*, 57 (2007) 793.

[62] Park, S.S., Oh, Y.S., Kang, D.H., Kim, N.J., *Materials Science and Engineering A,* 449-451 (2007) 352.

[63] Wang, Y. R., Feng, J. C., Zhang, Z. D., *Science and Technology of Welding and Joining*, 11 (2006) 555.

[64] Spittle, J.A., *International Materials Reviews,* 51 (2006) 247.

[65] Heintze, G.N., Pherson, R.M. *Weld Journal*, 65 (1986) 71s.

[66] Kerr, H.W., in 'International trends in welding science and technology', (eds.) S. A. David and J. M. Vitek, 157, Materials Park, OH, ASM International, (1993).

[67] Flood ,S.C., Hunt, J.D., ASM Metal Handbook, 15, (1990).

[68] Davis, G.J., Garland, J.G., *International Metallurgical Reviews,* 20 (1975) 83.

[69] Tiller, W.A., Jackson, K.A., Rutter, J.W., Chalmers, B., *Acta Metallurgica*, 1 (1953) 428.

[70] Hunt, J.D., *Materials Science and Engineering*, 65 (1984) 75.

[71] Quested, T.E., Greer, A.L., *Acta Materialia,* 53 (2005) 4643.

[72] Gaumann, M., Trivedi, R., Kurz, W., *Materials Science and Engineering* A, 226–228 (1997) 763.

[73] Martorano, M.A., Beckermann, C., Gandin, Ch.A., *Metallurgical and Materials Transactions A,* 34 (2003) 1657.

[74] Hallum, D.L., Baeslack, W.A.III, *Welding Journal*, 69 (1990) 326s.

[75] Kato, M., Matsuda, F., Senda, T., *Transaction of the Japan Welding Society,* 3 (1972) 69.

[76] Reinhart, G., Mangelinck-Noel, N., Nguyen-Thi, H., Schenk, T., Gastaldi, J., Billia, B., Pino, P., Hartwig, J., Baruchel, J., *Materials Science and Engineering A*, 413-414 (2005) 384.

[77] Mangelick-Noel, N., Nguyen-Thi, H., Reinhart, G., Schenk, T., Cristiglio, V., Dupouy, M.D., Gastaldi, J., Billia, B., Hartwi, J., Baruchel, J, *Journal. Physics D*, 38 (2005) A28.

[78] Nguyen-Thi, H., Reinhart, G., Mangelinck-Noel, N., Jung, H., Billia, B., Schenk, T., Gastaldi, J., Hartwig, J., Baruchel, J., *Metallurgical and Materials Transactions A*, 38 (2007) 1458.

[79] Sturz, L., Drevermann, A., Pickmann, C., Zimmermann, G., *Materials Science and Engineering A*, 413-414 (2005) 379.

[80] Pollock, T.M., Murphy, W.H., *Metallurgical and Materials Transactions A,* 27 (1996) 1081.

[81] Ganaha, T., Kerr, H.W., *Metals Technology*, 5 (1978) 62.

[82] Ohno, A., Motegi, T., Soda, H., *Transaction ISIJ*, 11 (1971) 18.

[83] Martorano, M.A., Biscuola, V.B., *Acta Materialia,* 57 (2009) 607.

[84] StJohn, D.H., Cao, P., Qian, M., Easton, M.A., *Advanced Engineering Materials*, 9 (2007) 739.

[85] Ruddle, R.W., "Solidification of Castings," Institute Metals, London, (1957).

[86] Trivedi, R Kurz, W., *International Materials Reviews,* 39 (1994) 49.

[87] Norman, A.F., Drazhner, V., Prangnell, P.B., *Materials Science and Engineering*, *A*, 259 (1999) 53.

[88] Spittle, J.A., Brown, S.G.R., *Journal of Materials Science*, 23 (1989) 1777.

[89] Spittle, J.A., Brown, S.G.R., *Acta Metallurgica*, 37 (1989) 1803.

[90] Zhu, P., Smith, R.W., *Acta Metallurgical Materialia*, 40 (1992) 683.

[91] Gandin, Ch.A., Rappaz, M., *Acta Metallurgical Materialia*, 42 (1994) 2233.

[92] Rappaz, M., Gandin, Ch.A., Desbiolles, J.L., Thevoz, Ph., *Metallurgical and Materials Transactions* A, 27 (1996) 695.

[93] Badillo, A., Beckermann, C., *Acta Materialia*, 54 (2006) 2015.

[94] Dong, H.B., Lee, P.D., *Acta Materialia*, 53 (2005) 659.

[95] Wang, C.Y., Beckermann, C., *Metallurgical and Materials Transactions A*, 25 (1994) 1081.

[96] Wu, M., Ludwig, A., *Metallurgical and Materials Transactions A*, 38 (2007) 1465.

[97] Mcfadden, S., Browne, D.J., Gandin, Ch.A., *Metallurgical and Materials Transactions A*, 40 (2009) 662.

[98] Winegard, W.C., Chalmers, B., *Transaction of ASM*, 46 (1954) 1214.

[99] Witzke, S., Riquet, J.P., Durand, F., *Acta Metallurgica,* 29 (1981) 365.

[100] Spaepen, F., *Acta Metallurgica,* 23 (1975) 729.

[101] Lipton, J., Glicksman, M.E., Kurz, W., *Materials Science and Engineering,* 65 (1984) 57.

[102] Trivedi, R., *Journal of Crystal Growth*, 49 (1980) 219.

[103] Kurz, W., Fisher, D.J., *Acta Metallurgica,* 29 (1981) 11.

[104] Trivedi, R., *Metallurgical Transactions A*, l5 (1984) 977–982.

[105] Somboonsuk, K., Mason, J.T., Trivedi, R., *Metallurgical Transactions A*, 15 (1984) 967.

[106] Esaka, H., Kurz, W., *Journal of Crystal Growth,* 72 (1985) 578.

[107] Langer, J.S., Muller-Krumbhaar, M., *Acta Metallurgica,* 26 (1978) 1681.

[108] Fletcher, N.H., *The Journal of Chemical Physics,* 29 (1958) 572.

[109] Greer, A.L., *Philosophical Transactions of the Royal Society of London A,* 361 (2003) 479.

[110] Auer, S., Frenkel, D., *Nature*, 409 (2001) 1020.

[111] Christian, J.W., “The Theory of Transformation in Metals and Alloys,” Pergamon, Oxford, (1975).

[112] Herlach, D.M., Gao, J., Holland-Moritz, D., Volkmann, T., *Materials Science and Engineering A,* 375–377 (2004) 9.

[113] Burden, M.H., Hunt, J.D., *Journal of Crystal Growth*, 22 (1974) 109.

[114] Liu, F., Yang, G., Guo, X., *Journal Materials Science*, 36 (2001) 3607.

[115] Duflos, F., Stohr, J.F., *Journal Materials Science*, 17 (1982) 3641.

[116] Kim, W.T., Cantor, B., *Scripta Metallurgica et Materialia*, 24 (1990) 633.

[117] Cochrane, R.F., Battersby, S.E., Mullis, A.M., *Materials Science and Engineering A,* 304–306 (2001) 262.

[118] Gunther, R., Hartig, Ch., Bormann, R., *Acta Materialia*, 54 (2006) 5591.

[119] Herlach, D.M., Gao, J., Holland-Moritz, D., Volkmann, T., *Materials Science and Engineering A,* 375–377 (2004) 9.

[120] Nyvlt, J., *Journal of Crystal Growth*, 3/4 (1968) 377.

[121] Kashchiev, D., Borissova, A., Hammond, R.B., Roberts, K.J., *Journal of Crystal Growth*, 312 (2010) 698.

[122] EI-Benawy, T.A., EI-Mahallawy, N.A., Taha, M.A., Fredriksson, H., *Materials Science and Technology*, 14 (1998) 721.

[123] Sangwal, K., *Journal of Crystal Growth*, 318 (2011) 103.

[124] Munitz, A., Bamberger, A.M., Wannaparhun, S., Abbaschian, R., *Journal Materials Science*, 41 (2006) 2749.

[125] Cantor, B., Kim, W.T., Bewlay, B.P., Gillen, A.G., *Journal Materials Science*, 26 (1991) 1266.

[126] Kim, W.T., Cantor, B., *Scripta Metallurgica et Materialia*, 24 (1990) 633.

[127] Tiner, N., *AIME Tech. Pub.,* 12 (1945) 1.

[128] Byun, J.Y., Kwon, S., Ha, H.P., Yoon, J. K., "Magnesium Alloys and Their Applications," K.U. Kainer, ed., Weinheim, Wiley–VCH, pp. 713, (2003).

[129] Tamura, Y., Yagi, J., Haitani, T., Motegi, T., Kono, N., Tamehiro, H., Saito, H., *Materials Transactions*, 44 (2003) 552.

[130] Cahn, J.W., In: Cargill, G.S, Spaepen, F., Tu, K.N., (eds.) "Phase transitions in condensed systems – experiments and theory," Pittsburgh (PA): Materials Research Society; pp. 41–55, (1987).

[131] Turnbull, D., *Acta Metallurgica,* 1 (1953) 8.

[132] Qian, M., Ma, J., *The Journal of Chemical Physics,* 130 (2009) 214709–1.

[133] Greer, A.L., Bunn, A.M., Tronche, A., Evans, P.V., Bristow, D.J., *Acta Materialia*, 48 (2000) 2823.

[134] Maxwell, I., Hellawell, A., *Acta Metallurgica*, 23 (1975) 229.

[135] Qian, M., *Acta Materialia*, 55 (2007) 943.

[136] Tarshis, L.A., Walker, J.L., Rutter, J.W., *Metallurgical and Materials Transactions A*, 2 (1971) 2589.

[137] Spittle, J., Sadli, S., *Materials Science Technology*, 11 (1995) 533.

[138] Easton, M.A., StJohn, D.H., *Acta Materialia*, 49 (2001) 1867.

[139] Turnbull, D., Vonnegut, R., *Industrial and Engineering Chemistry,* 44 (1952) 1292.

[140] Reynolds, J.A., Teottle, C.R., *Journal Institute Metals*, 80 (1951) 1328.

[141] Bramfitt, B.L., *Metallurgical Transactions*, 1 (1970) 1987.

[142] Kelly, P.M., Zhang, M.-X., *Metallurgical and Materials Transactions A*, 37 (2006) 833.

[143] Zhang, M.-X., Kelly, P.M., *Acta Materialia*, 53 (2005) 1073.

[144] Zhang, M.-X., Kelly, P.M., *Acta Materialia*, 53 (2005) 1085.

[145] Zhang, M.-X., Kelly, P.M., Qian, M., Taylor, J.A., *Acta Materialia*, 53 (2005) 3261.

[146] Zhang, M.X., Kelly, P.M., Easton, M.A., Taylor, J.A., *Acta Materialia,* 53 (2005) 1427.

[147] Qiu, D., Taylar, J.A., Zhang, M.X., Kelly, P.M., *Acta Materialia,* 55 (2007) 1447.

[148] Zhang, M.X., Kelly, P.M., *Scripta Materialia,* 52 (2005) 963.

[149] Cao, P., StJohn, D., Qian, M., *Materials Science Forum,* 488–489 (2005) 139.

[150] Lei, L., Zhou, S., Tian, Y., Feng, J., Jung, J., Zhou, Y.N., *Science and Technology of Welding and Joining,* 14 (2009) 356.

[151] Lei, L., Xiao, L., Feng, J.C., Tian, Y.H., Zhou**,** S.Q., Zhou, Y.N., *Metallurgical and Materials Transactions A*, 41 (2010) 2642.

[152] Yu, L., Nakata, K., Yamamoto, N., Liao, J., *Materials Letter,* 63 (2009) 870.

[153] Xiao, L., Liu, R., Zhou, Y., Esmaeili, S., *Metallurgical and Materials Transactions A*, 41 (2010) 1511.

[154] Yoo, M.H., *Metallurgical and Materials Transactions A*, 12 (1981) 409.

[155] Wang, Y.N., Huang, J.C., *Acta Materialia*, 55 (2007) 897.

[156] Koike, J., Kobayashi, T., Mukai, T., Watanabe, H., Suzuki, M., Murayama, K., Higashi, K., *Acta Materialia*, 51 (2003) 2055.

[157] Caceres, C.H., Sumitomo, T., Veidt, M., *Acta Materialia*, 51 (2003) 6211.

[158] Barnett, M.R., Keshavarz, Z., Nave, M.D., *Metallurgical and Materials Transactions A*, 35 (2005) 1697.

[159] Patel, H.A., Chen, D.L., Bhole, S.D., Sadayappan, K., *Materials Science and Engineering A,* 528 (2010) 208.

[160] Meyers, M.A., Voringer, O., Lubarda, V.A., *Acta Materialia*, 49 (2002) 4025.

[161] Conrad, H., Narayan, J.J., *Acta Materialia*, 50 (2002) 5067.

[162] Zhang, S., *International Journal of Fracture*, 88 (1997) 167.

[163] Zhang, S., *Weld Journal,* 80 (2001) 201s.

[164] Chen, C.Q., Pei, Y.T., De Hosson, J.T.M., *Acta Materialia*, 58 (2010) 189.

[165] Xiao, L., Umakoshi, Y., *Philosophical Magazine*, 83 (2003) 3407.

[166] Xiao, L., Umakoshi, Y., Sun, J., *Metallurgical and Materials Transactions A*, 32 (2001) 2841.

[167] Qian, M., Das, A., *Scripta Materialia,* 54 (2006) 881.

[168] Buha, J., *Materials Science and Engineering A,* 492 (2008) 11.

[169] Chang, B., Shi, Y., Lu, L., *Journal of Materials Processing Technology*, 108 (2001) 307.

[170] Ma, C., Chen, D.L., Bhole, S.D., Boudreau, G., Lee, A., Biro, E., *Materials Science and Engineering A*, 485 (2008) 334.

[171] Obara, T., Yoshinaga, H., Morozumi, S., *Acta Materialia*, 21 (1973) 845.

[172] Stohr, F.F., Poirier, J.P., *Philosophical Magazine,* 25 (1972) 1313.

[173] Honeycombe, R.W.K., "The Plastic Deformation of Metals," 2nd ed., London, Edward Arnold Publishers Ltd., (1984).

[174] Wang, H., Xu, Y.L., Sun, Q.Y., Xiao, L., Sun, J., Ge, P., *Metallurgical and Materials Transactions A*, 40 (2009) 2631.

[175] Suresh, S., "Fatigue of Materials," Cambridge, New York, Cambridge University Press, (1998).

[176] Gall, K., Biallas, G., Maier, H.J., Gullett, P., Horstemeyer, M.F., Mcdowell, D.L., *Metallurgical and Materials Transactions A*, 35 (2004) 321.

[177] Bernard, J.D., Jordon, J.B., Horstemeyer, M.F., Kadiri, H. El, Baird, J., Lamb, D., Luo, A.A., *Scripta Materialia,* 63 (2010) 751.

[178] DebRoy, T., David, S.A., *Reviews of Modern Physics*, 67 (1995) 85.

[179] Villafuerte, J.C., Kerr, H.W., *Metallurgical and Materials Transactions A*, 21 (1990) 979.

[180] Lu., L., Dahle, A.K., StJohn, D.H., *Scripta Materialia,* 53 (2005) 517.

[181] Lu., L., Dahle, A.K., StJohn, D.H., *Scripta Materialia,* 54 (2006) 2197.

[182] Kim, Y.M., Yim, C.D., You, B.S., *Scripta Materialia*, 57 (2007) 691.

[183] Nimityongskul, S., Jones, M., Choi, H., Lakes, R., Kou, S., Li, X., *Materials Science and Engineering A,* 527 (2010) 2104.

[184] Mohanty, P., Gruzleski, J., *Acta Metallurgical Materialia*, 43 (1995) 2001.

[185] Wang, Y., Zeng, X., Ding, W., Luo, A.A., Sachdev, A.K., *Metallurgical and Materials Transactions A*, 38 (2007) 1358.

[186] Moore, T.M., *Microscopy Today*, 13 (2005) 40.

[187] Ribic, B., Palmer, T.A., DebRoy, T., *International Materials Reviews,* 54 (2009) 223.

[188] Mishra, S., DebRoy, T., *Materials Science and Technology,* 22 (2006) 253.

[189] Xiao, L., Gu, H., *Metallurgical and Materials Transactions A*, 28 (1997) 1021.

[190] Merwe, J.H. van der, *Philosophical Magazine A*, 45 (1982) 127.

[191] Merwe, J.H. van der, *Philosophical Magazine A*, 45 (1982) 145.

[192] Merwe, J.H. van der, *Philosophical Magazine A*, 45 (1982) 159.

[193] Fujii, T., Mori, T., Kato, M., *Acta Metallurgical Materialia,* 40 (1992) 3413.

[194] Duly, D., *Acta Metallurgical Materialia,* 41 (1993) 1559.

[195] Xiao, L., Esmaieli, S., Zhou, Y., *Unpublished Research,* (2011).

[196] Han, B.Q., Dunand, D.C., *Materials Science and Engineering A,* 277 (2000) 297.

[197] Zhong, X.L., Wong, W.L.E., Gupta, M., *Acta Materialia*, 55 (2007) 6338.

[198] Xiao, L., Liu, R., Zhou, Y., Esmaeili, S., *Metallurgical and Materials Transactions A*, 43 (2012) 598.

[199] Turnbull, D., *Metallurgical Transactions A*, 12 (1981) 695.

[200] Turnbull, D., Cech, R.E., *Journal of Applied Physics,* 21 (1950) 804.

[201] Vandyoussefi, M., Creer, A.L., *Acta Materialia*, 50 (2002) 1693.

[202] Kurz, W., Trivedi, R., *Acta Metallurgica*, 38 (1990) 1.

[203] Greer, A.L., *Materials Science and Engineering A*, 133 (1991) 16.

[204] Zhang, M.X., Kelly, P.M., *Acta Materialia,* 46 (1998) 4617.

[205] Karma, A., Langer, J.S., *Physics Reviews A,* 30 (1984) 3147.

[206] Nelson, D.R., Spaepen, F., in "Solid State Physics," Vol. 42, eds. H. Ehrenreich, F. Seitz and D. Turnbull. Academic, New York, p. 1, (1989).

[207] Eustathopoulos, N., *International Materials Reviews,* 28 (1983) 189.

[208] Easton, M.A., Schiffl, A., Yao, J.Y., Kaufmann, H., *Scripta Materialia,* 55 (2006) 379.

[209] Wang, Y.X., Zeng, X.Q., Ding, W.J., *Scripta Materialia,* 54 (2006) 269.

[210] Liu, F., Yang, G.C., *International Materials Review*, 51 (2006) 146.

[211] Fan, Z., Wang, Y., Xia, M., Arumuganathar, S., *Acta Materialia,* 57 (2009) 4891.

[212] Wang, Y., Xia, M., Fan, Z., Zhou, X., Thompson, G.E., *Intermetallics,* 18 (2010) 1683.

[213] Inoue, A., Ohtera, K., Kita, K., Masumoto, T., *Japan Journal Applied Physics* 27 (1988) L2248.